A reciprocity method for multiple source simulations

Thesis by

Leo Eisner

In Partial Fulfillment of the Requirements
for the Degree of
Doctor of Philosophy

Caltech
Pasadena, California

2001
(Submitted St. Valentine, February 14, 2001)

Bez konců šiRé moře je, jde vlna za vlnou,
hrob jedné vlny druhé je zelenou kolébkou.
Kdo první vlnu vytvořil, ten stvořil také poslední...

A borderless vast ocean, wave by wave,
the death of one is a green cradle for the next.
He, who created the first wave, also created the last one...

Balada o Namořníkovi, Jíří Wolker (1900-1924).

To my mother.

Acknowledgements

A short time after I arrived at Caltech, back in the hot summer of 1995, my friend wrote me in a letter: "A duck which flew over the ocean still remains a duck!". Today I know the right answer: "But it is a duck which flew over the ocean!!!" I am grateful for the gift of wings from my kind Prague advisors Professor Vlatislav Červený and Dr. Ivan Pšenčík. I feel very fortunate to have had the opportunity to learn from them and their high moral and scientific values will be carried on, I promise.

I would like to thank the faculty, staff and students of the Seismolab, the Division and the entire Caltech community for some wonderful years in which I enjoyed their support, understanding and the beauty of science. My appreciation goes to my thesis advisor, Rob Clayton, whom I thank for his valuable input. Thanks to Hiroo Kanamori, for a great opportunity to get his kind advice by consulting with him. His great insight and overview reminded me in many ways of my Prague years, yet his drive to understand nature beside mathematics gave me a new point of view on my own work. Joann Stock is admired for standing by, rain or shine; always ready to help, she has been a wonderful academic adviser for me! I wish I could get all of Don Helmberger's good jokes, and I am glad I could always get the advise I needed! It was a mind stimulating adventure to take a class with Don Anderson, and I feel honored I had a chance to work with him, yet I feel guilty for leaving an unfinished job. I admire Tom Heaton for having so much patience and explaining to me the basics of engineering. Talking about the basics, I thank Jeroen Tromp for extra teaching his T.A. (me) and his kind advise during my adventure of the finite frequency equivalent medium parameters. I also thank Luis Rivera and Rob Graves. I will never forget the evening conversations by an open fire with Dr. Bob Sharp on trips through southern California. Jason Saleeby upgraded the stay on the Big Island to a great trip.

I thank Tim Kunz (former Amoco employee) and his family for being so nice to me during my internship at Tulsa and taking me to and from the hospitals after my accident. That summer at Tulsa was a wonderful time, thanks to Joe Etgen and Joe Dellinger (both still with BP-Amoco). That oily internship actually motivated my earthquake research and I am grateful to Leon Thompsen (BP-Amoco).

I would like to thank Caltech and SCEC for my financial support, their service, and secretaries, who ran everything so smoothly. Special thanks to Ann and Michele for their great help! I have enjoyed the company of my dear officemates who first introduced me to the community (Jascha, Craig, Xi), then came my drinking buddies (Javier, Brian, Martin) and the brave ones who were there when I was writing my thesis (Sidao, Kaiwen, Charlotte and Vala). Igor, despite not being an office-mate, became a soul-mate; I am glad we met and he, Natasha, Sasha and Dimka will always be in my heart. Olivier and Marco became the safe harbors to whom I would always run for fun or when needed. I had a wonderful time with Jamie; thank you very much for your support and friendship. Mair, Frank and Alison Carpenters, my English-Walsh family, have been supportive during my entire life, and I thank them for a beautiful friendship. Special thanks go to Jascha and Hong Kie whose priceless friendship was always rewarding (no, you can't buy it with your Master-card!). Dear Javier, I wish I could name those earthquakes after the wonderful data we found together. Thanks, Jane, for making my first Christmas without my family interesting, and thanks to Elisa for a taste of the real American Thanksgiving. I would like to thank also to friends and colleagues Anu, Cangli and Ling, Chen, Debbie, Ernie (and his delicious food), Garret (who told me that the berries growing around Catalinas are not edible, unfortunately too late), Jeroen (Ritsema), Louis (Moresi), Liz (Moyer), Liz (Eboer), Lupei, Tim and Anna.

Last but definitely not least, a deep gratitude belongs to my mother, Marie Glückaufová, who is the best mother-father I could wish. Words are not enough to express how much you mean to me!

Abstract

This thesis develops and applies the reciprocity method to assess the seismic site and path effects at a chosen location of interest. To do this, we show that the reciprocity theorem is valid for this application, and develop a technique to represent velocity models of sedimentary basins. Using these tools we test the accuracy of synthetic seismograms computed for southern California. Finally, we apply the reciprocity technique to evaluate the site and path effects for three selected sites in southern California.

The first chapter describes the reciprocity method for simulating seismograms due to multiple earthquake sources at a site of interest. It shows a theoretical proof of the method and discusses the practical implementation and accuracy for the finite difference technique. The numerical tests show that the reciprocal simulations can be performed with the same level of accuracy as the forward calculations.

The second chapter develops a new methodology to represent models of sedimentary basins with extremely low near surface velocities by replacing these velocities with equivalent medium parameters for a finite frequency signal. The new model has a higher minimum velocity, which makes the numerical simulations feasible, and minimizes the difference between the seismograms from the original and new model.

The third chapter validates the velocity model by comparing synthetics and data. It applies the reciprocity method and compares the full waveform synthetic seismograms with a large number of weak motion data. The discrepancies between the predicted waveforms and the data are interpreted by analyzing the attributes of seismograms to find regions of the model that are in error.

Finally the reciprocity technique is applied to calculate site and path effects in the Los Angeles area for three selected sites by simulating 75 source scenarios on 5 major southern California faults. The largest amplitudes at the selected sites are obtained from earthquakes on local faults rather than an earthquake on the San Andreas fault.

Contents

List of Figures

List of Tables

Chapter 1 Introduction

Earthquakes can not be predicted, but we can reduce their negative effects on society by better understanding the way they cause damage. It is clear that most earthquake damage consists of the collapse of man-made structures. Therefore, by designing structures that can better withstand earthquake shaking, we can significantly reduce the negative effects of earthquakes on society. The design of structures can be adjusted if we know what kind of ground motions the structures should withstand. Therefore, we have developed a practical method to assess the ground motion due to a large number of earthquakes at a particular site.

Ever since Galileo Galilei endeavored to determine the resistance of a beam, one end of which is built into a wall, when the tendency to break it arises from its own or an applied weight (Love's historical introduction [*Love*, 1892]), naturalists became interested in formulation of a theory to explain the displacement of a solid body which is subject to the action of a system of forces. It was the discovery of the proportionality of stress and strain by Robert Hooke in 1660 [*Hooke*, 1678] that enabled the formulation of the mathematical foundations of elastic theory which became immensely successful, not only in the analysis of Galileo's problem, but many other natural phenomena, including earthquakes. Further advances of Bernoulli, Euler, and Young, to name a few, in elastic theory finally led Navier [*Navier*, 1827] to formulate the general equations of equilibrium and vibration of elastic solids. Part of his equations became the core of the numerical code used in this thesis.

This thesis exploits the Betti's reciprocal theorem simultaneously discovered by *Betti* [1871-73] and *Rayleigh* [1873]. The theorem is widely used in various parts of mathematical physics and, as shown in Chapter 2, it is also suitable for numerical evaluation of multiple earthquake responses. Since the discovery of Hooke's law, naturalists seek the best fitting constants of proportionality between stress and strain (parameters of the medium) in order to understand the observations. The Earth's interior can be studied only from its surface (and above the surface) making the Earth sciences even more sensitive to the parameterization of the shallow regions of the Earth. Lord Rayleigh's discovery [*Rayleigh*, 1885] of surface waves made it evident that the influence of the free surface dominates the character of the observed motions due to an earthquake, the most powerful tool to study the Earth's interiors. Professor Horace Lamb [*Lamb*, 1904] in his first ever analysis of the complete propagation of the vibrations over the surface of an isotropic elastic halfspace notes: "It is a more difficult matter [curvature of the Earth vs. halfspace] to estimate the nature and extent of the modifications produced by heterogeneity... even considerable discontinuities would have little influence if their scale were small compared with the wavelength of the primitive impulse. A covering of loose material over the solid rock probably causes only local, though highly irregular modifications, with some dissipation of energy." Chapter 3 of this thesis analyzes conditions under which covering loose material (e.g. sediments) over a rock causes either local or propagation modification to the observed seismograms. Furthermore, the chapter shows how to find the parameters of the medium representing the near surface low velocity (loose rock) for modeling of the seismic waves of a limited frequency range. To do meaningful seismic modeling, we must show that the synthetic seismograms reproduce the previously observed data. Therefore a large number of weak motion observed seismograms is compared with the synthetics in Chapter 4. Chapter 5 applies the reciprocity to evaluate site and path effects using synthetic seismograms.

The present day knowledge of the subsurface structure does not allow us to successfully reproduce the observed ground motion data in our numerical simulations for short and intermediate periods (periods shorter than 3-5 seconds). This is especially true for regions with strong heterogeneities such as the sedimentary basins of southern California. Therefore, we focus our study on the long period seismic hazard which is mostly important for large structures, such as tall buildings, bridges, etc.

It was Chris Chapman (*Chapman and Coates* [1991]) who noted that full waveform synthetic seismograms can be as difficult to interpret as real data (hopefully not more). Therefore, now that we have better numerical techniques to evaluate waveform synthetic seismograms at our disposal; can we use them in a clever way? Chapters 4 and 5 of this thesis offer two applications for realistic numerical modeling.

Chapter 2 A reciprocity method for multiple source simulations

”In a space occupied by air, let A and B be two sources of disturbance. The vibration excited at A will have at B the same relative amplitude and phase as if the places were exchanged. ... ; but we are now in a position to assert that the reciprocity will not be interfered with, whatever number of strings, membranes, forks, &c. may be present, even though they are subject to damping.”

Rayleigh [1873]

2.1 Abstract

Reciprocity is applied to the situation where numerical simulations are needed for a number of source locations, but relatively a few receiver positions. By invoking source-receiver reciprocity, the number of simulations can be generally reduced to three times the number of receiver positions. The procedure is illustrated for a heterogeneous medium with both single force and double-couple sources. The numerical tests using a finite-difference implementation show that the reciprocal simulations can be performed with the same level of accuracy as the forward calculations.

2.2 Introduction

Simulations of waves in complex 3D media have shown that wave propagation in basin-like structures can cause significant variations in amplitudes, traveltimes, and coda of the strong ground motion [*Graves*, 1995; *Olsen et al.*, 1997; *Wald and Graves*, 1998]. The usual procedure is to evolve the wavefield outward from the source location to a suite of observation points, which means that one complete simulation needs to be done for each source location. For many problems such as comparing seismograms recorded for many earthquakes at a particular site, this straightforward approach can be computationally expensive. The same situation is true for iteratively calculating the source response for inverse problems.

However, with the use of three orthogonal point forces at the receiver locations and the reciprocity theorem, the number of numerical calculations can be reduced to 3 times the number of the receivers. Here we show a technique for calculating the Green's functions and their derivatives for the full elasto-dynamic equation that exploits reciprocity to reduce the number of simulations.

The property of source-receiver reciprocity has been known for a long time for the elasto-dynamic equations of motion and has been widely used in exploration seismology. *Claerbout* [1976] for example shows that reciprocity is a fundamental property of the elasto-dynamic equation. Reciprocity of the ray theoretical reflection/transmission in anisotropic medium was finally resolved by *Chapman* [1994] and a general proof for arbitrary media is given by *Červený* [2001]. *de Hoop and de Hoop* [2000] gave an extensive overview of the application of reciprocity in remote sensing including a generalized theory for source inversion. There are several applications of the reciprocity theorem to the full waveform modeling in seismology. *Bouchon* [1976] used reciprocity to develop a technique for computation of synthetic seismograms due to sources in a strongly heterogeneous media. Our paper extends the work of *Graves and Clayton* [1992] who used reciprocity for acoustic modeling of path effects in 3-D basin structures. Recently *Graves and Wald* [2001] applied elastic reciprocity to the finite fault inversion.

In this paper we shall first give a detailed proof of the reciprocity theorem with sources on the boundary of domain of interest (section 2.3). Then we shall discus a numerical implementation of the reciprocity for a finite-difference method (section 2.4). The finite-difference method is particularly suitable for application of the reciprocity method since the whole 3-D volume is calculated for each run; thus an arbitrary number of sources can be simulated in the 3-D volume. Finally we shall numerically test the accuracy of the reciprocity method on several simple models (section 2.5).

2.3 The reciprocity theorem

The reciprocity theorem is proven in *Aki and Richards* [1980] (page 28) for an elastic anisotropic continuous medium. *Dahlen and Tromp* [1998] (page 230) generalized their proof for an anelastic, piece-wise continuous body. Here we discuss in detail the boundary conditions of the reciprocity theorem as needed for the reciprocity method. We extend the proof of *Dahlen and Tromp* [1998] for source and receiver positions on the boundary of an area of interest. The basic statement of reciprocity is contained in Betti's theorem. *Dahlen and Tromp* [1998] (page 160) show Betti's reciprocal relation for a piece-wise continuous anelastic body with total volume V bounded by a surface Σ (equation 5.64 of *Dahlen and Tromp* [1998]):

$$\begin{aligned}
&\int_{-\infty}^{\infty}\int_{V} s_i(\vec{x},\vec{x}';t-t')\bar{f}_i(\vec{x},\vec{x'};-t,t')\partial V\,dt \\
&\quad+\int_{-\infty}^{\infty}\int_{\partial V} s_i(\vec{x},\vec{x}';t-t')\bar{t}_i(\vec{x},\vec{x'};-t,t')d\Sigma dt \\
&\qquad=\int_{-\infty}^{\infty}\int_{V} \bar{s}_i(\vec{x},\vec{x}';-t+t')f_i(\vec{x},\vec{x'};t,t')\partial V\,dt \\
&\qquad\quad+\int_{-\infty}^{\infty}\int_{\partial V} \bar{s}_i(\vec{x},\vec{x}';-t+t')t_i(\vec{x},\vec{x'};t,t')d\Sigma dt.
\end{aligned} \tag{2.1}$$

Here $s_i(\vec{x},\vec{x}';t-t')$ is the *i-th* component of the displacement vector which is a solution of the elasto-dynamic equations

$$\begin{aligned}\rho(\vec{x})\frac{\partial^2}{\partial t^2}s_i(\vec{x},\vec{x}';t-t') =& f_i(\vec{x},\vec{x'};t-t',0)\\ &+\frac{\partial}{\partial x_k}\left(\int_{-\infty}^{t'} c_{iklm}(\vec{x},t'-\tau)\frac{\partial}{\partial x_m}s_l(\vec{x},\vec{x}';t-\tau,0)d\tau\right),\end{aligned} \tag{2.2}$$

with a traction condition on the surface of volume V (∂V)

$$t_i(\vec{x},\vec{x'};t-t',0) = g_i(\vec{x},\vec{x'};t-t',0) + n_j\int_{-\infty}^{t'} c_{ijkl}(\vec{x},t'-\tau)\frac{\partial}{\partial x_l}s_k(\vec{x},\vec{x}';t-\tau,0)d\tau, \tag{2.3}$$

where $\vec{n}$ is a normal to the boundary of the volume V, $c_{ijkl}(\vec{x})$ is a tensor of elastic parameters and $\rho(\vec{x})$ is density characterizing a medium. The vector $\vec{f}$ represents the body forces inside the volume V, and the $\vec{g}$ represents the traction on the surface of the volume V. The barred variables satisfy the analogous condition

$$\begin{aligned}\rho(\vec{x})\frac{\partial^2}{\partial t^2}\bar{s}_i(\vec{x},\vec{x}';-t+t') =& \bar{f}_i(\vec{x},\vec{x'};-t+t',0)\\ &+\frac{\partial}{\partial x_k}\left(\int_{-\infty}^{t'} c_{iklm}(\vec{x},t'-\tau)\frac{\partial}{\partial x_m}\bar{s}_l(\vec{x},\vec{x}';-t+\tau)d\tau\right),\end{aligned} \tag{2.4}$$

with the analogous traction condition on ∂V

$$t_i(\vec{x},\vec{x'};-t+t',0) = \bar{g}_i(\vec{x},\vec{x'};-t+t',0) + n_j\int_{-\infty}^{t'} c_{ijkl}(\vec{x},t'-\tau)\frac{\partial}{\partial x_l}\bar{s}_k(\vec{x},\vec{x}';-t+\tau)d\tau. \tag{2.5}$$

To derive Betti's theorem (2.1) both barred and unbarred equations must satisfy continuity of the normal stresses at the discontinuities of $c_{ijkl}(x)$ and $\rho(x)$ and the forces $\vec{f}$ and $\vec{\bar{f}}$ have to be such that their contributions from time $t=\infty$ and $t=-\infty$ vanish. For an unbounded medium or a partially unbounded medium (such as a layered halfspace), the boundary conditions (2.3) and (2.5) are satisfied over the unbounded part of the medium as the left-hand side of both conditions (2.3) and

(2.5) vanish (either the source at infinity does not exist or, if it does, it takes an infinite time to receive any information about its existence), and so does the right-hand side of (2.3) and (2.5) as the vector of displacement must be zero at infinity. Therefore, the traction conditions (2.3) and (2.5) act only on the boundaries at finite distance.

Now we shall make a special choice of the source and receiver for the barred and unbarred variables and derive the reciprocity of the source and receiver position. By taking $\vec{\bar{t}}$ to be zero at the ∂V, and $\vec{\bar{f}}$ impulsive

$$\vec{\bar{f}}(\vec{x},\vec{x}';t,t') = \vec{e}_j\delta(\vec{x}'-\vec{x})\delta(t'+t), \qquad \vec{\bar{t}}(\vec{x},\vec{x}';t,t') = 0,$$

or $\vec{\bar{t}}$ impulsive at the ∂V, and $\vec{\bar{f}}$ zero everywhere in V

$$\vec{\bar{f}}(\vec{x},\vec{x}';t,t') = 0, \qquad \vec{\bar{t}}(\vec{x},\vec{x}',t,t') = \vec{e}_j\delta(\vec{x}'-\vec{x})\delta(t'+t),$$

where $\vec{e}_j$ is a unit vector in a direction of j-th axis, and body force $\vec{f}$ and traction $\vec{t}$ are oriented along the vector $\vec{e}_j$. The *i-th* component of the displacement vector $\vec{s}$ becomes by definition the *i-th* component of the Green's function due to the force acting along the $\vec{e}_j$ vector:

$$\bar{G}_{ji}(\vec{x},\vec{x}';-t+t') \equiv \bar{s}_i(\vec{x},\vec{x}';-t+t').$$

Hence, equation (2.1) reduces to

$$\begin{aligned} s_j(\vec{x},\vec{x}';t-t') = &\int_{-\infty}^{\infty}\int_V \bar{G}_{ji}(\vec{x},\vec{x}';-t+t')f_i(\vec{x},\vec{x}';t+t',0)\partial V dt \\ &+ \int_{-\infty}^{\infty}\int_{\partial V} \bar{G}_{ji}(\vec{x},\vec{x}';-t+t')t_i(\vec{x},\vec{x}';t-t',0)d\Sigma dt. \end{aligned} \tag{2.6}$$

And further by setting $\vec{t}$ to be zero at the ∂V, and $\vec{f}$ impulsive

$$\vec{f}(\vec{x},\vec{x}',t,t') = \vec{e}_i\delta(\vec{x}-\vec{x}')\delta(t-t'), \qquad \vec{t}(\vec{x},\vec{x}',t,t') = 0,$$

or $\vec{t}$ impulsive at the ∂V, and $\vec{f}$ zero everywhere in V

$$\vec{f}(\vec{x}, \vec{x'}, t, t') = 0, \qquad \vec{t}(\vec{x}, \vec{x'}, t, t') = \vec{e}_i \delta(\vec{x} - \vec{x'})\delta(t - t'),$$

and analogously the *j-th* component of the displacement vector $\vec{s_j}$ becomes by definition the *j-th* component of the Green's function due to the force acting along the $\vec{e}_i$ vector:

$$G_{ij}(\vec{x}, \vec{x'}; t - t') \equiv s_j(\vec{x}, \vec{x'}; t - t').$$

We obtain from (2.6) the reciprocal relation:

$$G_{ij}(\vec{x}, \vec{x'}, t - t') = \bar{G}_{ji}(\vec{x'}, \vec{x}, t - t'). \tag{2.7}$$

This proof of reciprocity is valid anywhere in the volume V or on its boundaries ∂V. Equation (2.7) allows the source and receiver points to be interchanged and identical seismograms will be recorded if the sources or receivers are situated inside the volume V or on its boundary δV. The proof is valid for a solution of elastodynamic equation (2.2, 2.4) with linearized attenuation represented by a stress-strain relationship $\sigma_{ij}(\vec{x}, t) = \int_{-\infty}^{t} c_{ijkl}(\vec{x}, t - \tau)\epsilon_{kl}(\vec{x}, \tau) d\tau$.

Equation (2.7) can be directly applied for evaluating the elastic fields from a single force point source by placing three single force sources at the receiver site ($\vec{x}$) and calculating response at the source area ($\vec{x'}$). However, elastic fields due to a double-couple (or a single-couple, or an explosive) point source require evaluation of the derivatives of the Green's functions:

$$u_i(\vec{x}, \vec{x'}, t - t') = \frac{dG_{ij}(\vec{x}, \vec{x'}, t - t')}{dx'_k} * M_{jk}(x', t')$$

where $*$ represents convolution over time. This equation can be evaluated by taking a numerical derivative of the reciprocal Green's functions of equation (2.7):

$$u_i(\vec{x}, \vec{x'}, t - t') = \frac{d\bar{G}_{ji}(\vec{x'}, \vec{x}, t - t')}{dx'_k} * M_{jk}(x', t') \tag{2.8}$$

Equations (2.7) and (2.8) allow us to evaluate a response due an arbitrary point source (double-couple, single-couple, explosive, or single force) without using body force equivalent forces (*Burridge and Knopoff* [1964], *Graves* [1996]).

2.4 Numerical implementation for the finite-difference method

For the problem of wave simulation in a complex three-dimensionally heterogeneous medium, we propose to calculate reciprocal Green's functions by interchanging the source and receiver positions. This is done by a standard finite-difference algorithm with a source placed at the receiver position. The results are then post-processed to generate the seismograms that would have been obtained if the source and receiver had not been interchanged. The efficiency of the reciprocal method comes with the fact that for each reciprocal simulation, a number of pseudo-receivers can be recorded. When the post-processing reverses the source-receiver relationship, this translates to synthetic seismograms due to many sources recorded at the same receiver.

The finite-difference technique we used is a velocity-stress equation solved by a staggered grid scheme [*Virieux*, 1984; *Graves*, 1996]. For the receivers not situated on the free surface, no special treatment is necessary for the reciprocal calculations. However, if the receiver is situated directly on the free surface, a more careful implementation of the three orthogonal point forces is necessary. We empirically found that the reciprocity is best satisfied by horizontal body forces implemented right at the free surface boundary and a vertical force half a grid point below the free surface. This fits better than averaging over the two staggered vertical components above and below the surface. Equation (2.8) can be evaluated as a recorded response to the three orthogonal point forces sources at the receiver site. This is a simple implementation in the finite-difference calculation since the response for the whole model for each time step is evaluated. To get $\bar{G}_{ij,k}$ we can use the first-order numerical spatial derivatives of the displacement centered at the source locations. Either the numerical derivatives or the corresponding $\bar{G}_{ij}$ itself can be saved at each pseudo-source point. One advantage of saving the $\bar{G}_{ij}$ comes if the source position is not known precisely and we would like to perturb its location. To save storage space we may store only certain combinations of the $\bar{G}_{ij,k}$. For example, if we are interested in the explosive sources, we only need to store $\bar{G}_{i1,1}$, $\bar{G}_{i2,2}$, $\bar{G}_{i3,3}$, or if we are interested in pure double-couple sources, we only need $\bar{G}_{i1,1}$, $\bar{G}_{i2,2}$, $\bar{G}_{i1,2} + \bar{G}_{i2,1}$, $\bar{G}_{i1,3} + \bar{G}_{i3,1}$, $\bar{G}_{i2,3} + \bar{G}_{i3,2}$.

One issue that arises in the practical application of the reciprocity method is that the boundary conditions are not completely reciprocal for finite-difference modeling. The most common boundary conditions used in finite-difference modeling are the free surface and absorbing boundaries. The free surface boundary condition satisfies in theory the condition of the reciprocity relation (2.7); however, different finite-difference formulations of the free surface boundary suffer various degrees of inaccuracy (*Zahradník et al.* [1993] or *Graves* [1996]). Discrepancies between direct and reciprocal seismograms can be used as a criterion for the accuracy of the free surface boundary condition as has been suggested by *Dellinger* [1997]. An absorbing boundary satisfies reciprocity, to the extent that it mimics perfectly the unbounded homogeneous space. Imperfections in the numerical implementation of the different versions of absorbing boundaries do not in general satisfy the reciprocity. In the examples we show, we generally try to avoid any contamination of our seismograms with reflections from absorbing boundaries.

2.5 The numerical test

The reciprocal method can be tested by showing that identical seismograms can be obtained comparing standard forward calculations with reciprocal ones. We apply this test to synthetic seismograms computed for the three cases: an unbounded homogeneous medium, a case with a 1-D variation of the medium parameters and a free surface, and a case with a 3-D variation of the medium parameters. In each case, the results are computed with a spatially fourth-order staggered-grid finite-difference scheme and second-order time derivatives. The finite-difference parameters are chosen to provide a reasonable level of modeling accuracy without prohibitive cost. The absorbing boundary conditions are the A1 of *Clayton and Engquist* [1977] and an additional attenuating zone to minimize the artificial reflections.

Homogeneous Unbounded Medium.

Figure 2.1 shows all nine components of the direct and reciprocal Green's functions $G_{ij}(x, x', t - t', 0)$ for a homogeneous unbounded medium computed with the staggered-grid finite-difference technique. The finite-difference results are accurate only for periods longer than 3 seconds however, we present unfiltered seismograms to demonstrate the reciprocity of not only the direct signal but also of the numerical noise generated by the FD method. We can see the reciprocal pairs match within the thickness of the line. The solutions start to diverge slightly for time around 13-18 seconds which corresponds to the artificially reflected waves from boundaries. The non-reciprocal mismatch increases with proximity to the absorbing boundary (as the waves hit boundary under more non-normal incidence) and are caused by both P- and S-wave reflected from the boundary.

Free Surface and 1-D Heterogeneous Medium.

Figure 2.2 shows three components of the direct and reciprocal seismograms recorded in the vicinity of the free surface from a source at the free surface. The 1-D model and the source mechanism are described in the figure caption. The 1-D structure traps energy in the upper layer of the model. Small discrepancies between the direct and reciprocal solution appear with the first arriving energy when the synthetic seismograms are computed with coarse sampling (5 points per wavelength). These discrepancies are caused by inaccuracies in the implementation of the free surface boundary conditions which cause it not exactly satisfy the continuity of the normal traction. The discrepancy diminishes as more accurate results are compared (right column with 10 points per S-wave wavelength in the top layer). Also note the slightly smaller amplitude computed with the finer grid - the more accurate computation evaluates more precisely the surface wave (which has a shorter wavelength than the

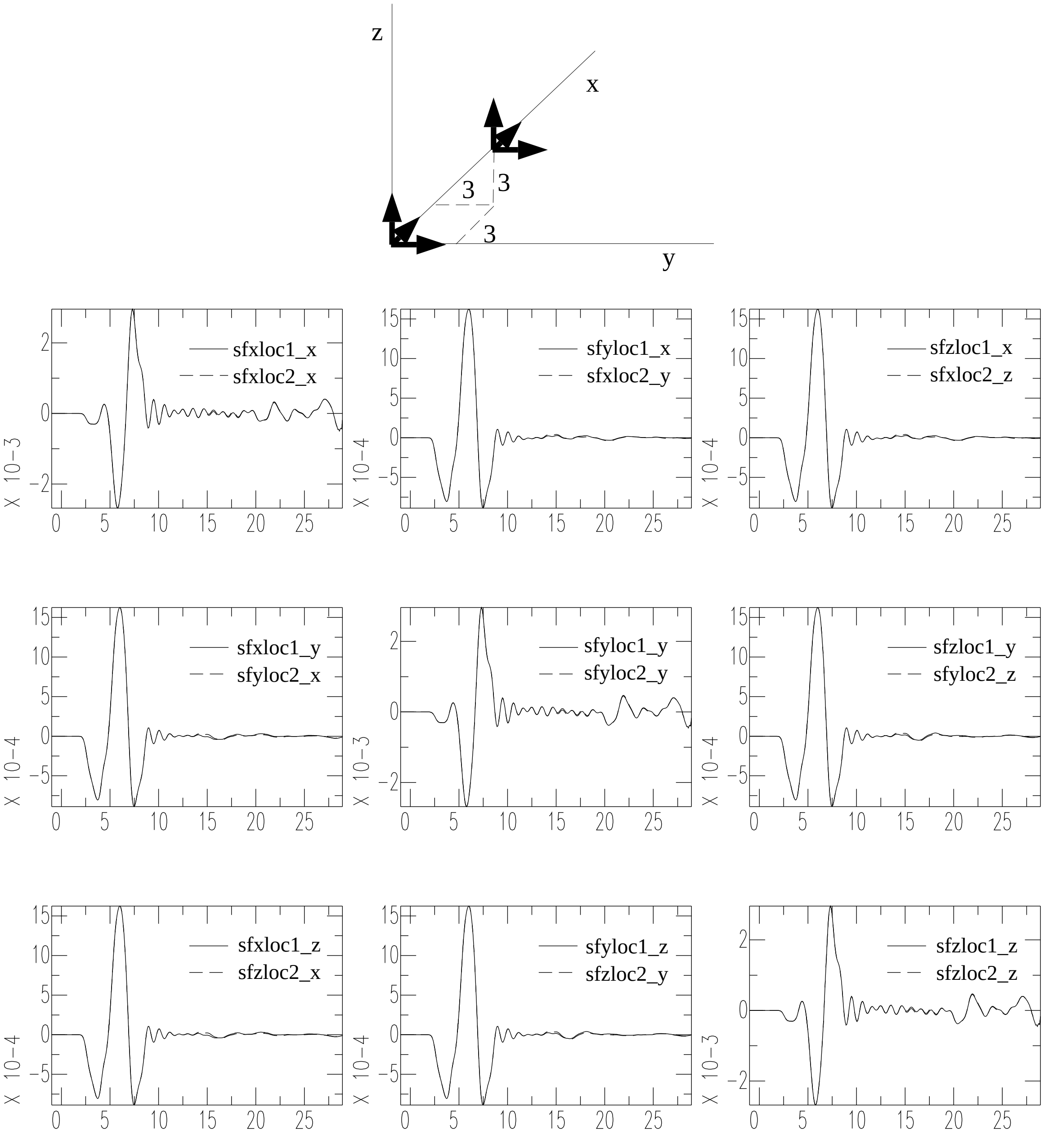

Figure 2.1: Nine pairs of Green's functions $G_{ij}(x, x', t, t')$: loc1 (solid line) represents source at (0.0 km,0.0 km,0.0 km) and receiver at (3.0 km,3.0 km,3.0 km), loc2 (dashed line) represents source at (3.0 km,3.0 km,3.0 km) and receiver at (0.0 km,0.0 km,0.0 km). The first three letters denote the source type: sfx is single force into x direction, sfy is single force into y direction, and sfz is single force into z direction. The last letter denotes the component at the receiver. The unbounded homogeneous medium was chosen with $\alpha = 2.0$ km/sec, $\beta = 1.0$ km/sec, and $\rho = 2.6$ g/ccm. Absorbing boundaries were placed at 12.0 km from the origin (0.0 km,0.0 km,0.0 km).

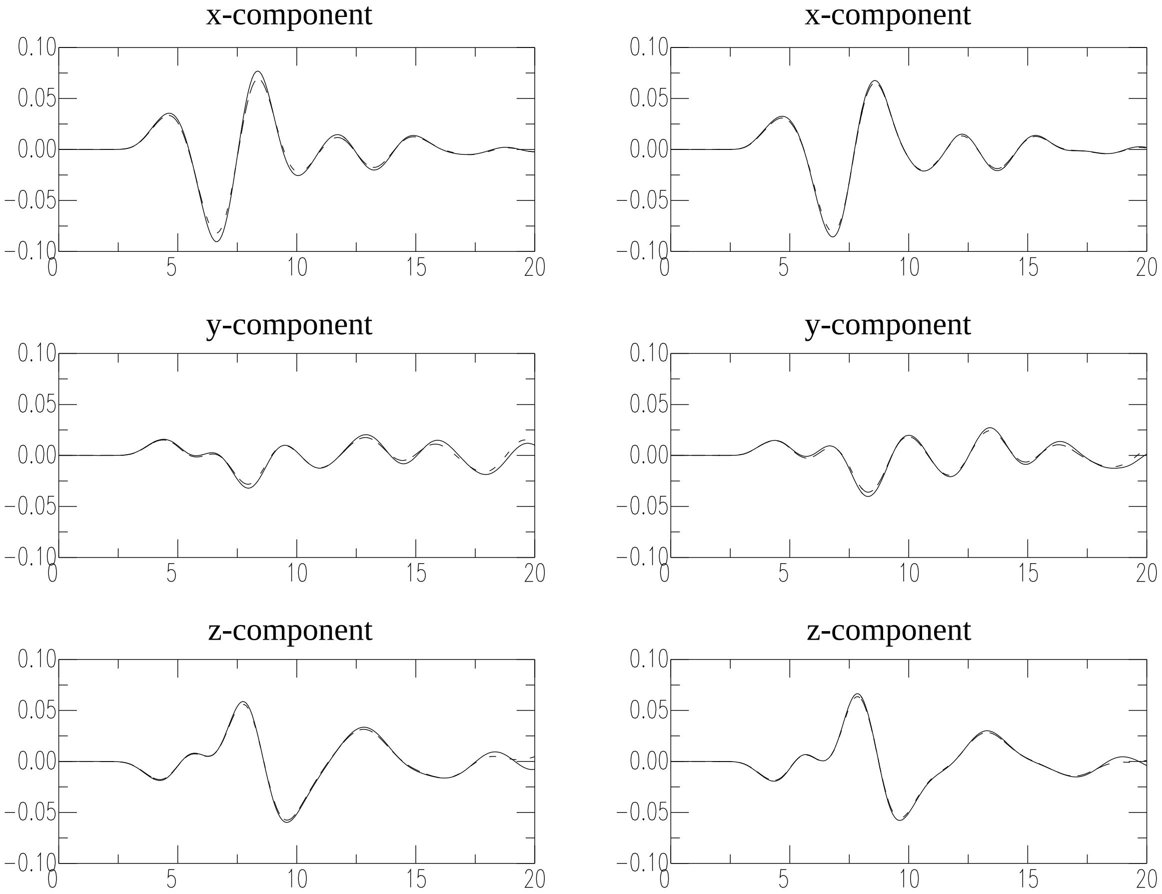

Figure 2.2: Three pairs of components of the acceleration (in mm/sec^2) due to a double-couple source at (0.0 km,0.0 km,3.6 km) recorded at a receiver (3.0 km,3.0 km,0.0 km). The seismograms correspond to an earthquake of magnitude 1.0 with dip slip (strike 0^o, rake 90^o and dip 90^o), x-axis is positive to the North, y-axis is positive to the East and z-axis is positive down. Solid line represents direct computation, and dashed line represents reciprocal computation. Left column was computed with 5 grid points per wavelength, and the right column of seismograms was computed with 7.5 points per wavelength. Seismograms computed for 1-D heterogeneous medium with parameters: $\alpha = 2.0$ km/sec, $\beta = 1.0$ km/sec $\rho = 2.0$ g/ccm from surface to 3.0 km depth, $\alpha = 4.0$ km/sec, $\beta = 2.0$ km/sec $\rho = 2.3$ g/ccm from 3.0 km to 6.6 km depth, $\alpha = 6.0$ km/sec, $\beta = 4.0$ km/sec $\rho = 2.7$ g/ccm for depths bellow 6.6 km.

direct shear wave and therefore was computed with even fewer points per wavelength). This phenomenon illustrates that the error due to the numerical implementation of the reciprocity (single force source at the free surface and numerical derivatives of the Green's functions) is smaller than the error due to the finite-difference computation (i.e., accuracy of the scheme, free surface boundary condition accuracy, and absorbing boundaries).

Laterally Heterogeneous Medium.

Figure 2.3 shows three pairs of components of a reciprocal and direct computation in a strongly heterogeneous medium. The 3-D model and the source mechanism are described in the figure caption. We have simulated the response due to a small earthquake in a strongly heterogeneous medium. There are many arrivals caused by diffracted energy trapped in the sedimentary basin. Overall, we can see the fit is very good and the direct calculation may be replaced with the reciprocal simulation. The discrepancy on the East component around 10s is caused by an artificial reflection from a model boundary which was close to the deep source used in the model. Note the largest discrepancies are on the smallest component.

Sampling of the Green's functions in Heterogeneous Medium.

Finally we would like to test the most efficient way of storing the derivatives of the Green's functions $\bar{G}_{ij}$ used for more complex sources suitable for iterative implementation of equation (2.8). We wanted to test if Green's functions $\bar{G}_{ij}$ can be stored instead of derivatives of the Green's function $\bar{G}_{ij,k}$. This way we hoped to be able to store Green's functions $\bar{G}_{ij}$ on a coarse grid and reevaluate the derivatives of Green's functions $\bar{G}_{ij,k}$ in the post-processing where needed. However, we show that the accuracy of such an approach is not satisfactory.

Figure 2.4 shows three components of the two approximations of the seismograms due to single-couple source. The two approximations differ in the accuracy of evaluation of the $\bar{G}_{ij,k}(x, t; \xi, \tau)$ of equation 2.8. The solid line represents the numerical derivative of the second order over the smallest possible grid step (1/5 of the shortest

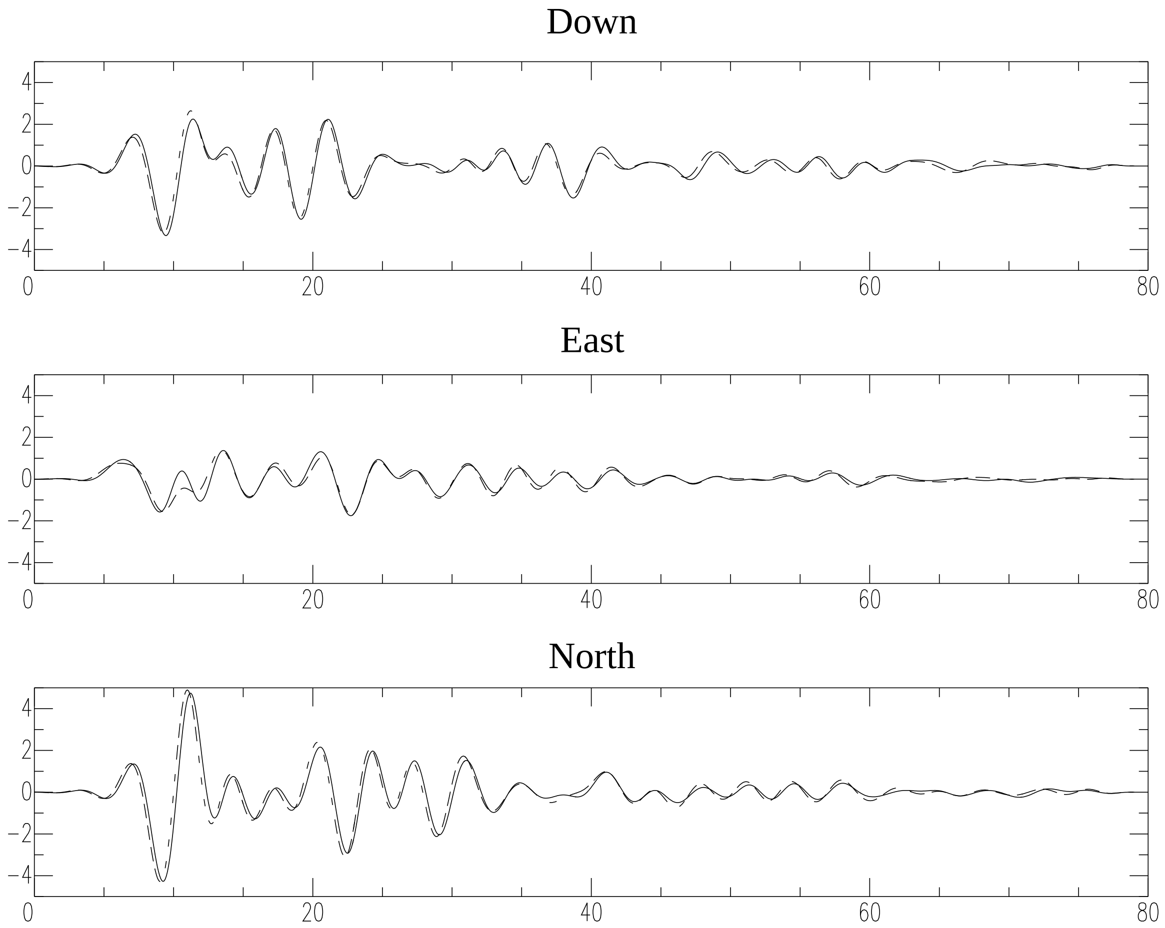

Figure 2.3: Three pairs of components of acceleration (in microns per second squared) due to a double-couple source in laterally heterogeneous velocity model of southern California SCEC version 1 (*Magistrale et al.* [1996]). The event simulates an aftershock of the Northridge earthquake (34.24^{o}N, 118.47^{o}W and depth z=15.1 km) as recorded at the Pasadena station (34.14^{o}N, 118.17^{o}W). The mechanism for a point source double-couple of the aftershock is strike 109^o, dip 63^o, and rake 82^o with magnitude 4.0 (coordinate system as in of Figure 2.2). The velocity model includes strong lateral variations of both P and S-wave velocities as well as densities due to the presence of the deep basins (Los Angeles and San Fernando in this case). The solid line represents the direct solution; and the dashed line is a reciprocal seismogram recorded at the free surface.

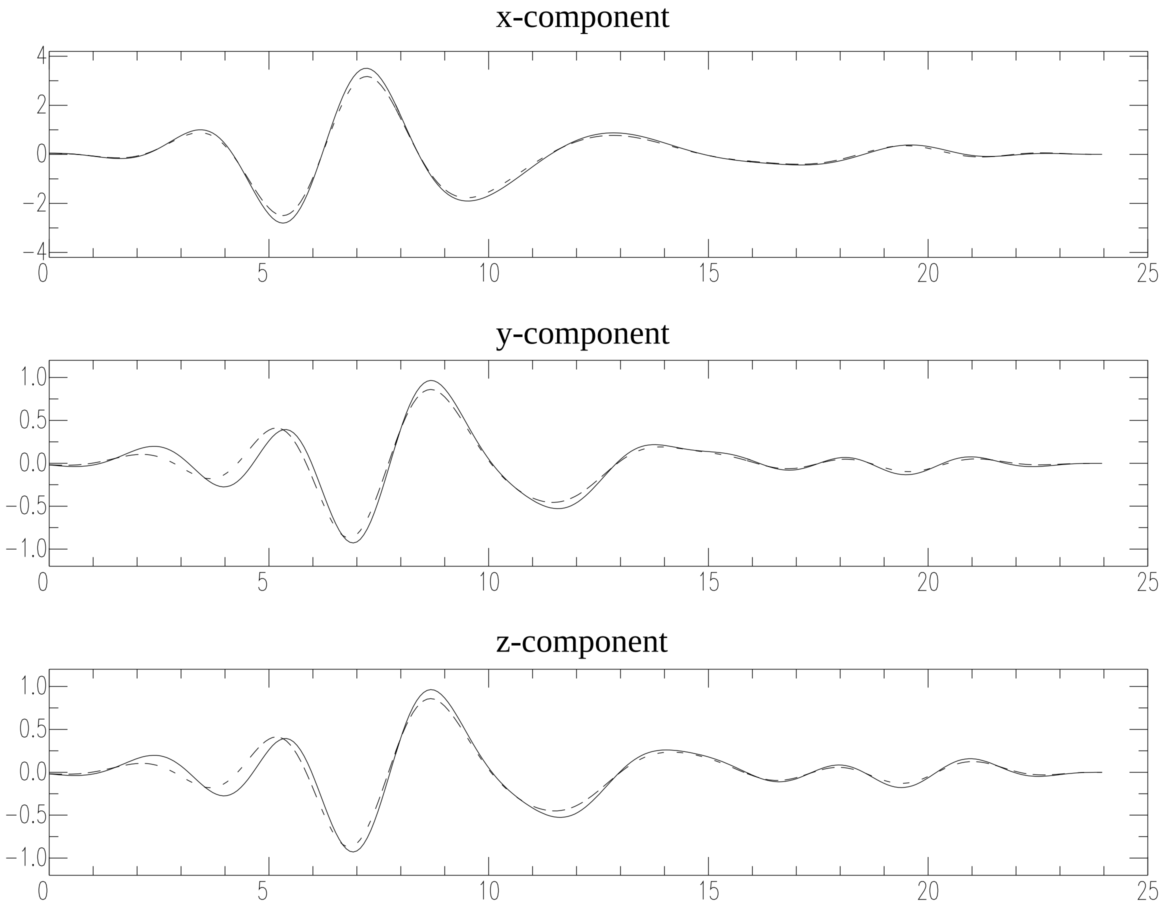

Figure 2.4: Three pairs of components of the acceleration due to a single-couple source at (0.0 km,0.0 km,2.6 km) recorded at receiver (3.0 km,3.0 km,0.0 km). Only component M_{zz} of the single-couple was excited. Solid line - reciprocal computation from numerical derivatives of the Green's functions with spacing 0.6 km, dashed line - reciprocal computation from numerical derivatives of the Green's functions with spacing 1.8 km. Seismograms recorded in 1-D heterogeneous medium parameters as that of Figure 2.2.

wavelength of S-wave), the same as used in the finite-difference run. The dashed line was calculated from the second-order numerical derivative over the three grid steps (1.8 km). We can see that the dashed line does not match the more accurate calculation both in amplitude (all components) and in phase. We have tested only the second-order derivative of the Green's function as we compare with a direct solution evaluated with the second order approximation of the moment tensor (*Graves* [1996]). Therefore, we need to directly store the derivatives of the Green functions $\bar{G}_{ij,k}$ evaluated on a fine grid.

2.6 Conclusions

The reciprocal method can be used to reduce the number of calculations where seismograms from many sources at a few receivers are desired. The numerical tests show that the errors due to the numerical implementation of reciprocity method itself are less than the errors of the finite-difference method. The accuracy of the procedure is dependent upon calculating the derivatives of the Green's functions to the same level of accuracy as the finite-difference itself. The method is suitable for source inversion and source relocation, where a large number of sources at different locations and with arbitrary mechanisms can be quickly simulated. Another application is in determining the anticipated size of strong ground motions at particular site due to an earthquake at many locations.

Chapter 3 Equivalent medium parameters for full waveform numerical modeling in isotropic media with low velocities near the free surface

3.1 Abstract

We have developed a methodology to discretize an isotropic velocity model with low velocities near the free surface for full waveform numerical modeling. The method modifies the near surface minimum velocity in the original model by replacing parts of the model with equivalent medium parameters (EMP) for a frequency range of interest. The discretized model (with EMP) has a higher minimum velocity, and minimizes the difference between the seismograms evaluated for the original model and the model with EMP. The method is suitable for studies requiring full waveform numerical modeling with a limited frequency range (such as a finite-difference full waveform modeling in a sedimentary basin). The discretized model with EMP is set to match locally surface-wave velocities evaluated in the original model over the frequency range of interest. The difference in group velocity calculated for the original vertical profile and the vertical profile with EMP provides an estimate of the error due to the modification of the original model.

3.2 Introduction

Numerical solution of the wave equation has become practical for large heterogeneous models. The accuracy of the numerical simulations (i.e. the mesh size) is determined by the slowest velocities in the model, which may span only a small portion of the model (usually the shallow sediments at or near the surface). The size of the required numerical simulations increases with a smaller mesh size (the required size of a model for a three-dimensional finite-difference simulation (*Graves* [1996]) increases proportional to the 4^{th} power of one over the mesh size). A simple clamping of the minimum velocities (known as a velocity cut-off, e.g. [*Olsen et al.*, 1995], [*Olsen and Archuleta*, 1996], [*Olsen et al.*, 1997], [*Graves*, 1998], [*Wald and Graves*, 1998]) can cause some significant errors, which appear to contaminate the surface waves. The velocity clamping often eliminates the near surface structure where many multiply reflected waves interfere constructively to create a significant effect on dispersion of long period surface waves. While attenuation will generally reduce the effect of the near surface low velocity structure, it does not eliminate it.

One solution to this problem is to use a variable mesh-size to reduce the number of calculations while preserving the accuracy (*Opršal and Zahradník* [1999], **?**, *Komatitsch and Tromp* [1999]). However, accurate variable mesh-size algorithms may substantially increase the algorithm complexity (*Opršal and Zahradník* [1999], **?**) or mesh generating algorithms (*Komatitsch and Tromp* [1999]). In this study, we propose a method in which the low velocity regions are modified in a manner that is consistent with the surface wave dispersion, but allows coarser sampling of the medium. We do not include into our method attenuation or any other anelastic effects of the low velocity regions; it is beyond the scope of this paper. We address how to sample models for elastic wave propagation in isotropic media.

The problem of correct discretization and velocity clamping is more significant than is commonly realized, particularly in the calculation of the multiply reflected waves inside sedimentary basins. *Graves* [1997] made a simple attempt to see the effect of the velocity clamping by comparing synthetic seismograms computed for models with different values of the velocity clamping. Our analyses started with analogous numerical experiments in which we compared seismograms computed for models with different values of the velocity clamping. In these tests a velocity clamping to a certain threshold is a replacement of all velocities lower than that threshold with that threshold. Figure 3.1 shows the effect of velocity clamping on long period seismic wave propagation. The direct body waves are not significantly affected, but later arrivals are very sensitive to the value of the velocity clamping. Both the source and the receiver are situated outside the sedimentary basins. Stations situated inside the sedimentary basin show even more sensitivity to the value of the velocity clamping. The horizontal components are most severely affected, especially the transverse component, dominated by the Love waves.

Therefore we propose to discretize the original model in a way that does not alter the surface wave velocities. Section 3.3 describes the algorithm for a 1-D medium and Section 3.4 shows a generalization of this method for a 3-D medium. Section 3.5 shows examples of the method applied to the numerical modeling of seismic waves in isotropic media. In the following we shall refer to the input model as the original model and the output modified model will be called the EMP model.

3.3 Equivalent medium parameters for a 1-D vertical profile

In this section we shall show how, for a given frequency range and a 1-D vertical profile, we can find an EMP vertical profile such that the entire synthetic seismogram (including surface waves) computed for both vertical profiles will agree as closely as possible. We shall require two conditions to reduce the cost of numerical modeling: the minimum velocity in the modified vertical profile must be higher than a certain *a priori* selected threshold (v_{min}) and the original and modified profiles are isotropic.

An analogous problem was solved by *Backus* [1962], who shows how to replace thin isotropic elastic layers with a homogeneous anisotropic layer. This method was gen-

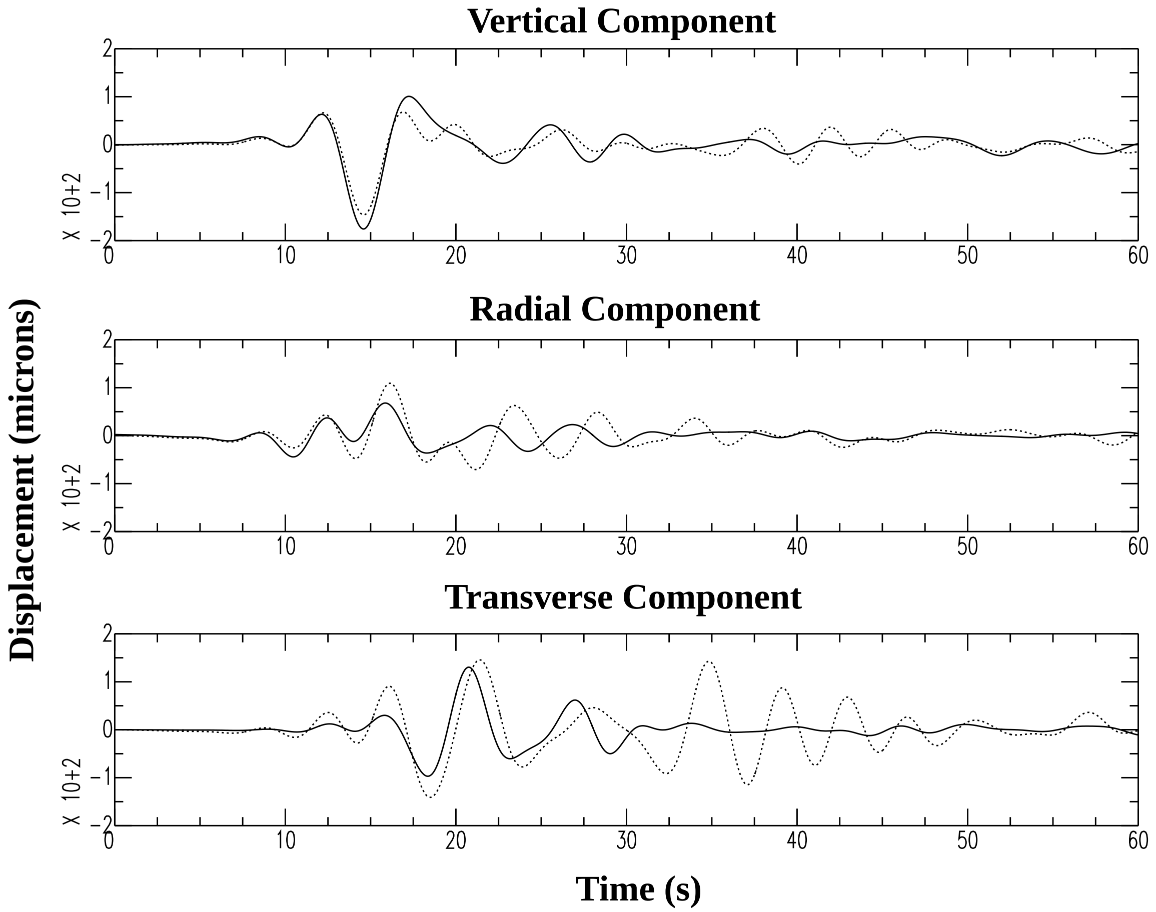

Figure 3.1: A comparison of synthetic seismograms computed for different values of the velocity clamping. Three components of displacement (in micrometers) due to a source in the model of SC3DVM (Version 1, *Magistrale et al.* [1996]). The event simulates an aftershock of the Landers earthquake (34.38^{o}N, 118.49^{o}W and depth at 6.7 km) as recorded at station Pasadena (34.14^{o}N, 118.17^{o}W). The point source double-couple mechanism of the aftershock is strike 278^o, dip 56^o, and rake 63^o with magnitude 4.2. The solid line represents the displacement computed for a model with a minimum velocity clamped to 1.0 km/sec, and the dashed line represents the displacement computed for a model with a minimum velocity clamped to 0.5 km/sec. The velocity model includes strong lateral variations of both P and S-wave velocity as well as density due to the presence of deep basins (Los Angeles and San Fernando in this case); however, neither source nor receiver are situated in the sedimentary basin.

eralized by *Schoenberg and Muir* [1989] for an arbitrary anisotropic elastic medium. This method is not dependent on the period range of interest (it is derived for infinitely long period); the modified vertical profile is always anisotropic and its minimum velocity may be lower than the *a priori* selected threshold.

3.3.1 Algorithm for a 1-D vertical profile

The original 1-D vertical profile is described by depth dependent P-wave and S-wave velocities and density. Let us assume there is a maximum depth h for which the S-wave velocity is lower than the *a priori* selected threshold. To modify the vertical profile we evaluate the Love wave group velocities $v_{gL}^{or}(T)$ over a range of periods of interest (T_1, T_2) using the original vertical profile. Then we find the new EMP S-wave velocity and density profile such that the S-wave velocity of the EMP profile is greater than or equal to the *a priori* selected threshold, by minimizing the relative error of the Love wave group velocities between the EMP and the original vertical profiles. We set the EMP vertical profile equal to the original vertical profile everywhere except the top layer of thickness H, where $H > h$. The EMP vertical profile is then found by a gradient search for the three parameters of the top homogeneous layer of the EMP profile: the thickness H, the S-wave velocity v_s^{EMP} and the density ρ^{EMP}. To find the new parameters of the homogeneous layer (h, v_s^{EMP}, and ρ^{EMP}), we minimize

$$E = \underset{(T_1,T_2)}{L_1} \left[\frac{v_{gL}^{EMP}(T, H, v_s^{EMP}, \rho^{EMP}) - v_{gL}^{or}(T)}{v_{gL}^{or}(T)} \right]. \tag{3.1}$$

Where the $\underset{(T_1,T_2)}{L_1}$ norm is applied over the period range of interest, and $v_{gL}^{EMP}(T, H, v_s^{EMP}, \rho^{EMP})$ is the group velocity evaluated for the EMP model.

The P-wave velocity is determined after we set the other parameters of the homogeneous layer: H, v_s^{EMP}, and ρ^{EMP}. We do not modify the P-wave velocity of the original model for depths greater than H. Ideally the P-wave velocity of the homogeneous layer should be determined by minimizing:

$$E = \underset{(T_1,T_2)}{L} \left[\frac{v_{gR}^{EMP}(T, v_p^{EMP}) - v_{gR}^{or}(T)}{v_{gR}^{or}(T)} \right], \tag{3.2}$$

where v_{gR} is the group velocity of Rayleigh waves, and v_p^{EMP} is the P-wave velocity of the homogeneous layer in the EMP profile. However for large 3-D velocity models evaluation of this equation is expensive (as it requires a gradient search). We found it to be sufficiently accurate to determine the P-wave velocity by using the ratio

$$\Re = \frac{1}{H} \int_0^H \frac{\lambda(z)}{\mu(z)} dz,$$

where z is the depth, $\lambda(z)$ and $\mu(z)$ are uniquely determined from the medium parameters of the original vertical profile. The P-wave velocity for a homogeneous layer is evaluated by

$$v_p^{EMP}(z_m) = v_s^{EMP}(z_m) \sqrt{\frac{\lambda + 2\mu}{\mu}} = v_s^{EMP}(z_m) \sqrt{\Re + 2}.$$

Figure 3.2 illustrates the result of fitting the Love wave dispersion with the equivalent medium parameters. The EMP and the original vertical profile's Love wave dispersion curves match only over the frequency range of interest. Note, that the group and phase velocities of the shorter periods are significantly different.

3.3.2 Discussion of the algorithm for a 1-D vertical profile

The lowest velocities in the velocity models of our interest occur near the surface. In our numerical experiments, we have found that Love waves are generally the most sensitive to the low-velocity structure near the surface. For this reason and for the reasons discussed in the introduction we have based our algorithm on matching the Love waves rather than Rayleigh waves or body waves. Love waves in a 1-D medium exists only on the transverse component. The frequency spectrum of the transverse component due to a source with a small frequency range in a vertically varying medium

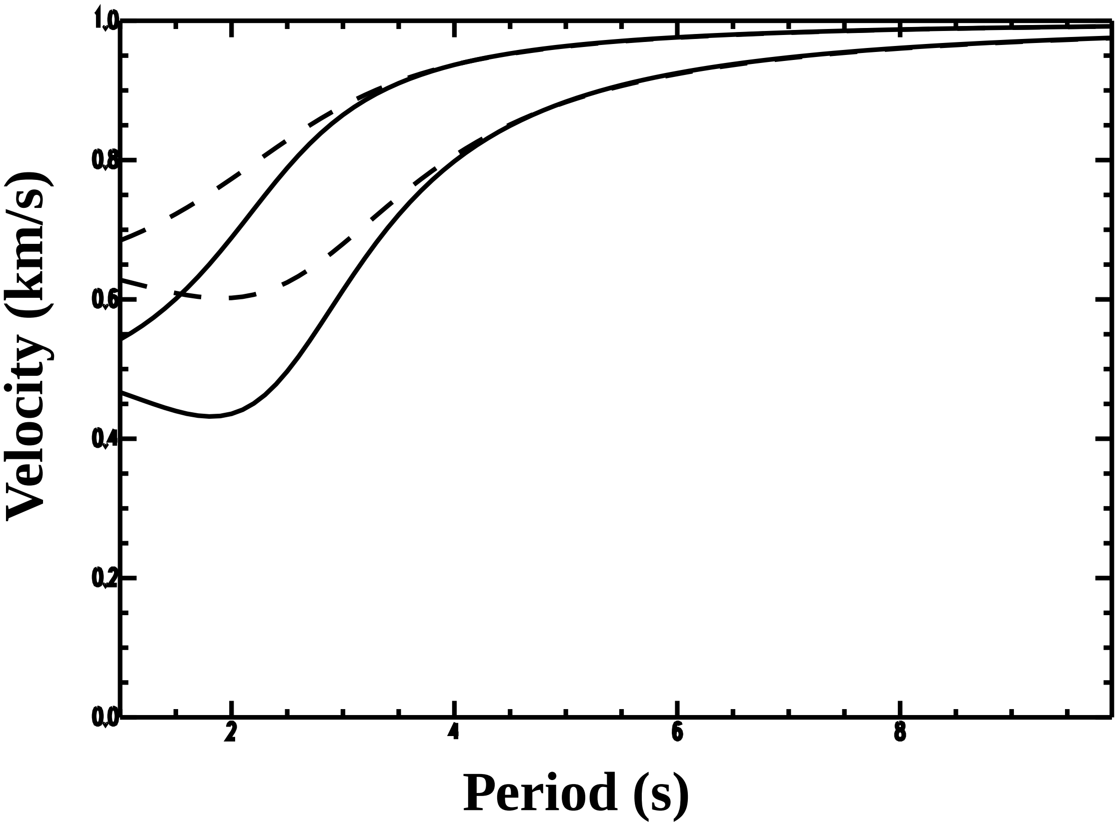

Figure 3.2: A comparison of the group and phase velocity of the original and the EMP models. The Love wave group and phase dispersion is matched only in the frequency range of interest (T>3 sec.). The solid line represents group and phase velocity of the original model; and the dashed line represents the group and phase velocity of the EMP model (phase velocity is greater than or equal to group velocity in each model).

can be evaluated from the formula (7.147) of *Aki and Richards* [1980]. This formula describes the elastic wave propagation effects on the synthetic seismograms due to the depth of the source and the receiver. The elastic wave propagation effects on the synthetic seismograms due to the horizontal (epicentral) distance of the source and receiver of a finite frequency signal centered about a given frequency ω_0 can be approximated by the formula (7.11) of *Aki and Richards* [1980]:

$$f_0(x,t) \sim \frac{\Delta\omega}{\pi}\frac{sinY}{Y}cos\left[\omega_0(t-\frac{x}{c})\right],$$

where $Y = \frac{\Delta\omega}{2}\left[t - \frac{x}{v_g}\right]$. Here $f_0(x,t)$ is a signal due to a normalized harmonic source (evaluated from (7.147) of *Aki and Richards* [1980]) of an angular frequency ω_0 at time t and distance x. The phase and group velocities of Love waves are c and v_g, respectively, both of which are functions of ω_0.

Because we modify the original model, we cannot obtain exactly the same seismograms computed for the original and the EMP models. An exact match between the seismograms computed for the two models would mean we match exactly the eigen-functions as well as the group and phase velocities evaluated at the original and the EMP models for the frequency range of interest, which is not possible. We have the choice of matching the phase velocities, or the group velocities, or the eigen-functions evaluated for the original and the EMP model. Of these possibilities, the group velocity seems to be a good compromise, because it guarantees that the energy in the seismograms evaluated for the original and the EMP model arrives at the same time. Matching only the phase velocities of the original and the EMP model does not give as good a match of the seismograms. Matching only the eigen-functions causes significant traveltime errors and it is much more expensive.

The discrepancy due to the propagation effect can be estimated from the difference in the two corresponding maximum energy arrivals in the seismograms evaluated for the original and the EMP vertical profiles:

$$\Delta t = \frac{x}{v_{gL}^{EMP}(T)} - \frac{x}{v_{gL}^{or}(T)} = t_{prop} \frac{v_{gL}^{EMP}(T) - v_{gL}^{or}(T)}{v_{gL}^{or}(T)}.$$

Here $t_{prop} = \frac{x}{v_{gL}^{EMP}(T)}$. The time discrepancy between arrivals of the corresponding groups of energy for a given distance x will increase with larger relative error of the group velocity and longer time of wave propagation in the modified model t_{prop}. For a given period we may estimate the time for which the seismograms should match by

$$t_{prop} < T \frac{v_g^{or}(T)}{v_g^{new}(T) - v_g^{or}(T)}. \tag{3.3}$$

The effects due to source depth, receiver depth, and source radiation pattern are important if the original and the EMP models' Love or Rayleigh wave eigen-functions differ significantly at the source or receiver positions. The perturbation of eigen-functions due to a velocity change at shallow depths rapidly decays with depth. We have numerically found that the differences in the original and the EMP models' eigen-functions due to the receiver or source position at the free surface are also negligible. However, if a receiver or a source is situated in the modified layer of the EMP model, the eigen-functions of the EMP and the original models may differ, thus causing some discrepancies.

A low velocity layer in the model should not be eliminated if it can trap seismic waves within the frequency range of interest. We have numerically found that the lowest group velocity (the minimum of the Airy phases) is very sensitive to a minimum velocity near the surface. Therefore, the near surface low velocity can be increased only if the frequency range of interest does not contain the frequency of the group velocity minimum. Furthermore, we have found that the higher mode cut-off frequency is usually higher or near the frequency of the minimum of the group velocities. Consequently, we do not include group and phase velocities of higher modes in the inversion.

It is also important to include a search over the density. The best fitting homogeneous layer of the EMP model tends to be of lower density compared to the original model. If we do not include a search over density, the EMP vertical profile's eigen-functions would not match the original model's eigen-functions. The lower densities may compensate for the increased velocity by maintaining the impedance contrast at the depth h of the replacement layer.

3.4 Equivalent medium parameters for a 3-D isotropic model

To modify a 3-D model we horizontally discretize it to be a set of 1-D vertical profiles. We evaluate the group velocity of the Love and Rayleigh waves in all 1-D vertical profiles and find the minimum group velocity in the frequency range of interest. This minimum determines the mesh size of our numerical simulation. Vertical profiles with velocities lower than the minimum are modified with the algorithm describe in the previous section 3.3.1.

3.4.1 Algorithm for a 3-D isotropic model

The input parameters of the algorithm are a 3-D model of P and S-wave velocities [$v_p^{or}(x, y, z)$ and $v_s^{or}(x, y, z)$ respectively] and density [$\rho^{or}(x, y, z)$], and the period range of interest (T_1, T_2).

In the first step, we discretize the original model to a finite set of vertical profiles at points $\{x_i, y_j\}$. The horizontal discretization should be fine enough to capture the slowest regions of the original model. Then we compute the group velocities of the Love $v_{gL}^{or}(T, x_i, y_j)$ and Rayleigh $v_{gR}^{or}(T, x_i, y_j)$ waves within the frequency range of interest at every point $\{x_i, y_j\}$. The values of the group velocities must be independent of the discretization of the original model. We find the minimum

$$v_{min} = \min_{T \in (T_1, T_2), x_i, y_j} (v_{gL}^{or}(T, x_i, y_j), v_{gR}^{or}(T, x_i, y_j)).$$

This determines the minimum velocity that must be used for the numerical simulation, which then sets the mesh size.

Now we shall again search through the entire original discretized model by examining vertical profiles for every point $\{x_i, y_j\}$. If for a horizontal point $\{x_i, y_j\}$, the velocity in its vertical profile does not drop below the minimum velocity v_{min}, we do not modify that vertical profile and parameters in the EMP model are equal to the original model for that profile. If for a horizontal point $\{x_i, y_j\}$, the velocity in its vertical profile drops below the minimum velocity v_{min}, we use the algorithm described in section 3.3.1 with threshold value v_{min} to rediscretize that profile.

3.4.2 Discussion of the algorithm for a 3-D isotropic model

The algorithm is suitable for a heterogeneous model with weak lateral inhomogeneity near the surface as for instance defined by *Levshin et al.* [1989]. The condition of the weak lateral inhomogeneity is locally satisfied by models with as much heterogeneity as the Southern California Velocity Model (SCVM) (*Magistrale et al.* [2000]). Figure 3.3 shows the Love wave group velocities computed for a period of 3 seconds for the SCVM (version 2.2). Several authors (*Graves* [1995], *Wald and Graves* [1998], *Olsen et al.* [1995], *Olsen and Archuleta* [1996]) have noted that the surface waves form the coda in their numerical simulations of the wave propagation inside the basins. This observation can be explained by the large zones of weakly heterogeneous group velocities in the basin regions as can be seen in Figure 3.3. The boundaries of the basins trap the surface waves inside the basins. Our algorithm finds a new model in which the group velocities for the periods of interest match the original model and it preserves the heterogeneity of the original model. In contrast to a simple velocity clamping, the method we propose preserves the average velocity. This means that we will increase the velocity in some regions of the original model as well as *decrease* it in other regions of the original model. This method requires a discretization of the original model. The volumetric averaging of slowness (*Muir et al.* [1992], **?**) is the most appropriate method to discretize an isotropic model to an isotropic model on a grid.

3.5 Numerical tests

To test the method we compare synthetic seismograms computed for the original and the EMP models. Tests with simple models will enable us to analyze the effects of the approximations we use. We shall start with the case of a layer over a half-space, then we shall test a complex vertically heterogeneous vertical profile selected from a realistic 3-D model and finally we shall show how the method works for laterally heterogeneous models.

For the layer over the half-space case we have chosen a layer with a velocity contrast of a factor of 2 to generate synthetic seismograms with observable dispersion. To test a large number of source locations in this model, we have used the reciprocity method (Chapter 2) with a single receiver at the free surface and 155 double-couple

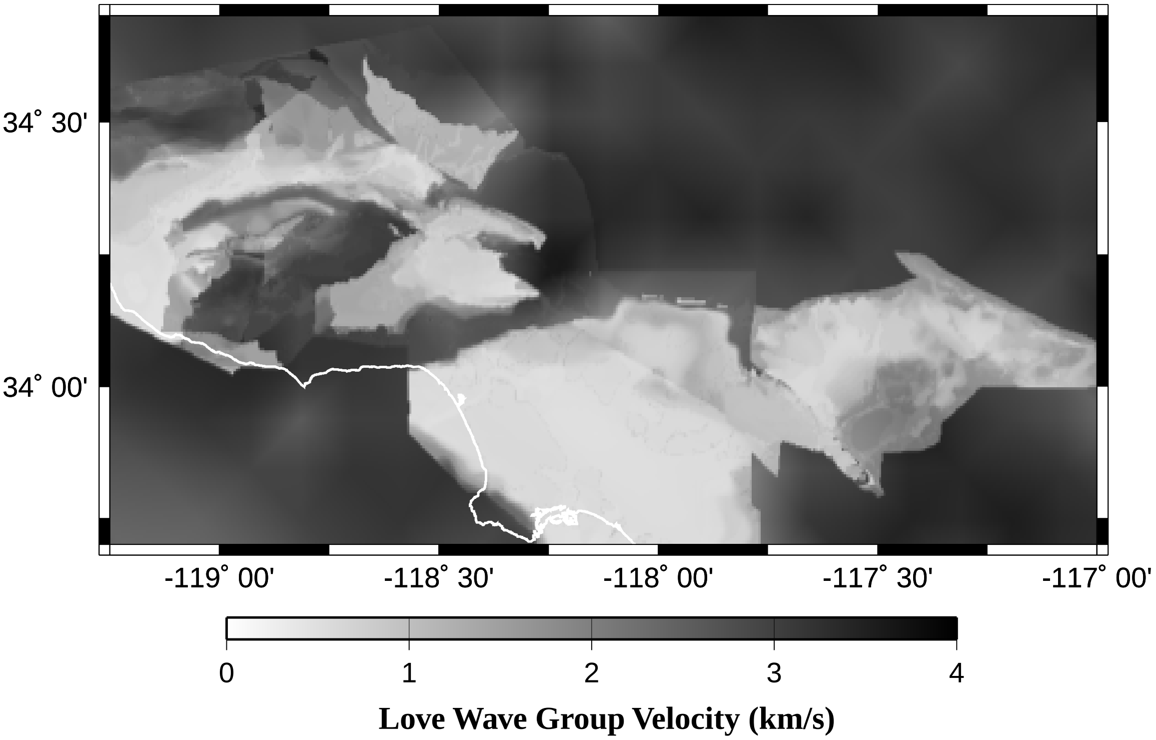

Figure 3.3: Large regions of the weakly heterogeneous media inside (and outside) the models of sedimentary basins. This figure shows the Mercator projection of the Love wave group velocity for a period of 3 seconds computed for the SC3DVM (version 2.2, *Magistrale et al.* [2000]). The group velocities were computed at discretized horizontal points (grid spacing length 300 m) by taking a vertical velocity profile with medium parameters discretized every 25 m for the top 1000 m and increased spacing below down to a depth of 45000 m.

point sources located throughout the model. The test for variable source depth is more sensitive to a change of the eigen-functions with depth as certain combinations of eigen-functions may be excited by the source mechanism. The source locations vary from 0 km to 24.0 km of epicentral distance and 0 km to 3.0 km depth (the deeper the source location, the smaller the effect of the near surface velocity variations). Sources beyond an epicentral distance of 24.0 km were not tested as we have limited our comparison to the first 60 seconds. The chosen time limit corresponds to the time set by the criteria for t_{prop} (see equation 3.3). The synthetic seismograms were compared for three source mechanisms from which a response due to an arbitrary double-couple mechanism can be evaluated by linear superposition (strike slip, vertical dip slip and 45^o dip slip). The original, the EMP and the velocity-clamped models are described

The Original model

Thickness of the layer (m)	β (m/s)	α (m/s)	ρ (kg/m^3)
300.0	500.0	1000.0	1900.0
∞	1000.0	1700.0	2200.0

The EMP model

Thickness of the layer (m)	β (m/s)	α (m/s)	ρ (kg/m^3)
500.0	640.0	1250.0	1430.0
∞	1000.0	1700.0	2200.0

The Velocity clamped model

Thickness of the layer (m)	β (m/s)	α (m/s)	ρ (kg/m^3)
300.0	640.0	1250.0	1430.0
∞	1000.0	1700.0	2200.0

Table 3.1: Medium parameters of the three layer over the half-space models.

in Table 3.1. The EMP model was evaluated for the signal with energy at periods of 3 seconds and longer. The velocity clamped and the EMP models have the same minimum velocity.

Figure 3.4 shows the worst matching seismograms computed with a finite-difference code for the original, the EMP, and the velocity clamped models. We have used a triangular source-time function with a length of 3 seconds. The worst matching seismograms as determined by cross-correlation were selected from 465 (155 source positions and 3 mechanisms) source-receiver combinations. The relative Love wave group velocity error corresponding to a period of 3.0 seconds is 7.5%, and criterion (3.3) sets $t_{prop} <40.0$ sec. The EMP and the original model's seismograms agree within a line thickness up to 30 seconds and the agreement deteriorates for arrivals after 45 seconds on the transverse component. The agreement of the radial and vertical components deteriorates for arrivals after approximately 37 seconds; however, the amplitude of these arrivals is an order of magnitude smaller than the amplitude on the transverse component. The velocity clamping does a poor job for all times after the onset. Also note that both the source and the receiver are situated at the free surface,

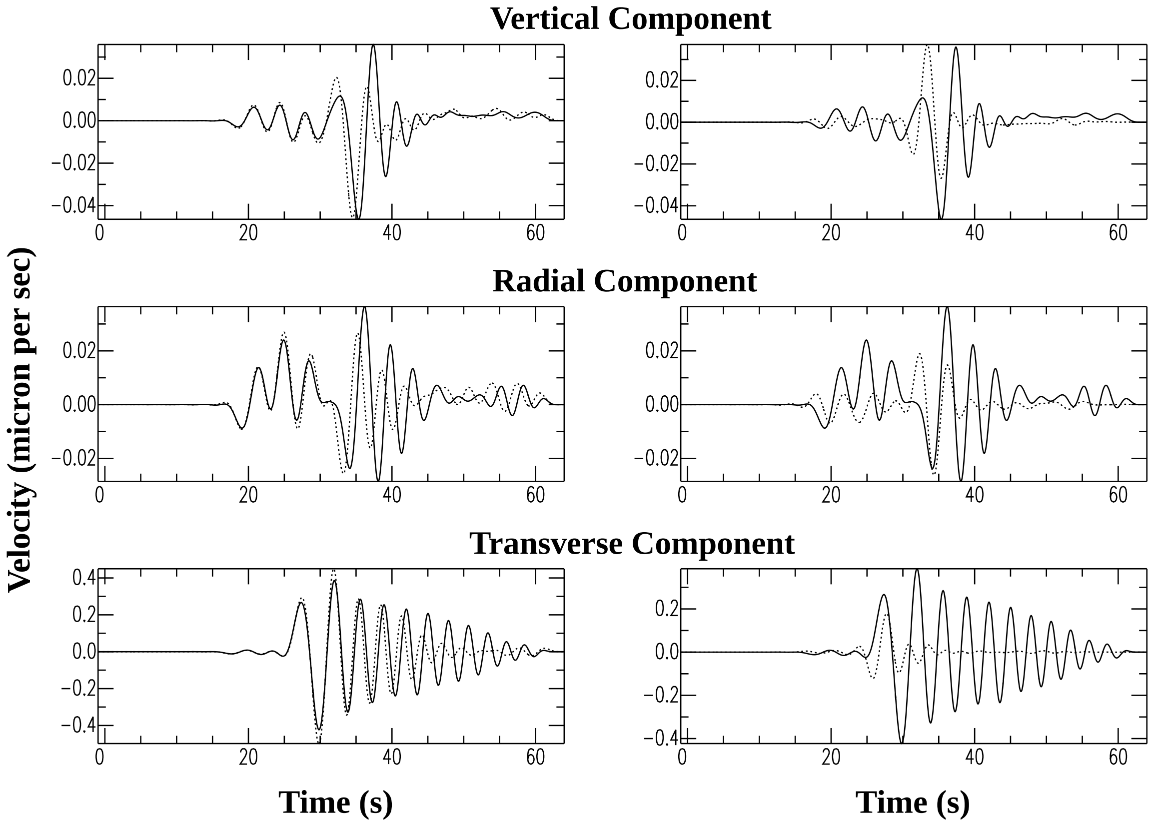

Figure 3.4: Comparison of the synthetic seismograms computed for the original, the EMP, and the velocity clamped models. Three components of velocity (in microns per second) due to a 45^o dip-slip double-couple point source situated at the free surface (azimuth 90^o, strike 90^o, dip 90^o, rake 45^o, magnitude $M_w = 1.0$). The source-receiver distance is 24.0 km. In both columns, the solid line is the synthetic seismogram computed for the original model. The dashed line in the left column is the synthetic seismogram computed for the EMP model while in the right column it shows synthetic seismograms computed for velocity clamped model. The models are described in Table 3.1.

on the top of the modified layer, which means that changes in the eigen-functions due to the modified medium parameters do not affect the synthetic seismograms.

Figure 3.5 shows the poorest matching seismograms computed for the original, the EMP, and the velocity clamped models with a double-couple point source mechanism of 90^o dip slip situated 0.25 km below the free surface at an epicentral distance of 22.0 km. Seismograms computed for the original and the EMP agree well up to 25 seconds and the agreement deteriorates for both the phase and the amplitude for times 25-40 seconds on all components. The source is situated at the center of the

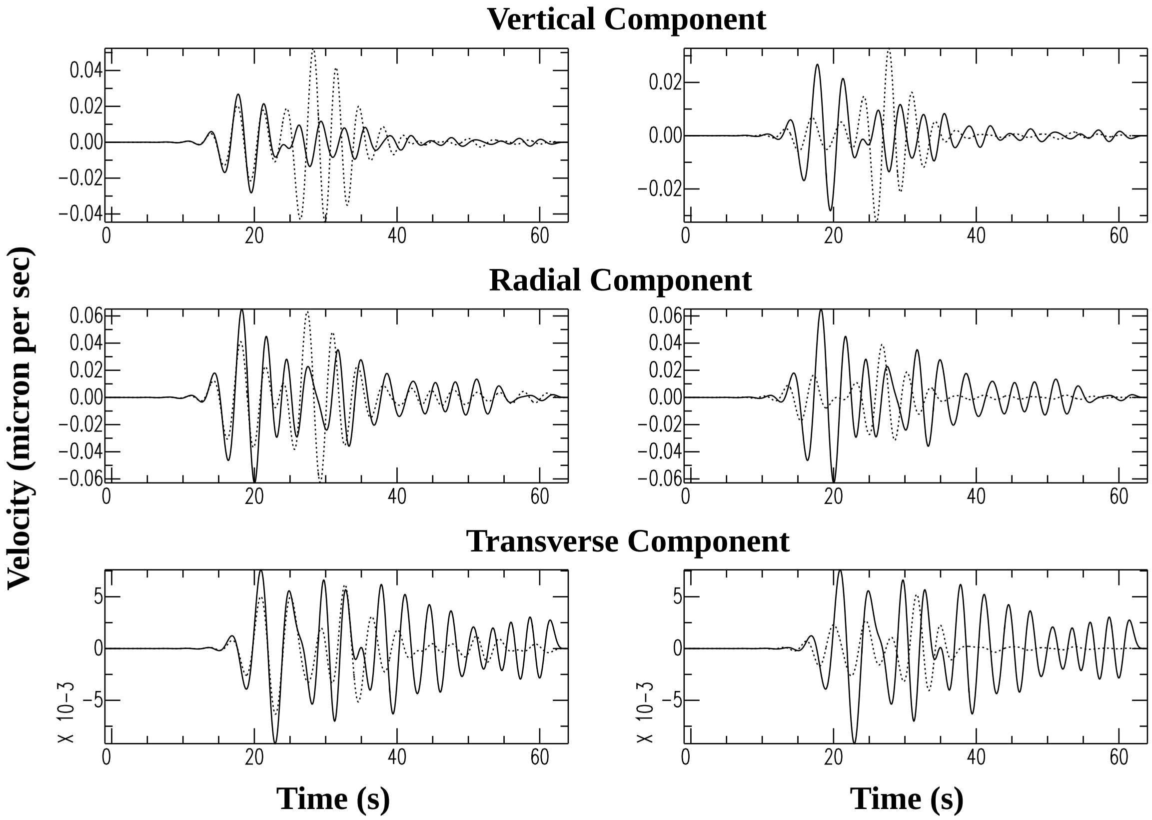

Figure 3.5: Comparison of the synthetic seismograms computed for the original, the EMP, and the velocity clamped models: the eigen-function problem. Three components of velocity (in microns per second) due to a dip-slip double-couple point source situated 0.25 km below the free surface (azimuth 90^o, strike 0^o, dip 90^o, rake 90^o, magnitude $M_w = 1.0$). The source-receiver distance is 22.0 km. In both columns, the solid line is the synthetic seismogram computed for the original model. The dashed line in the left column is the synthetic seismograms computed for the EMP model while in the right column it shows synthetic seismograms computed for velocity clamped model. The models are described in Table 3.1.

modified layer (thickness 0.5 km); at this depth the eigen-functions of the original and the EMP model (and the velocity clamped model) may significantly differ. Since we did not observe a similar discrepancy for different source mechanisms at the same hypocenter; we infer that the discrepancy is not caused by the epicentral distance but the source source mechanisms which may increase the difference between the eigen-functions of the original and EMP models. To further test this hypothesis, we have compared seismograms due to deeper sources where the eigen-functions do not differ as much between the original and the EMP models. Figure 3.6 shows seismograms due to the same double couple point source mechanism, the same epicentral distance, but at a depth of 2.0 km. The seismograms computed for the original and the EMP models match well up to 40 seconds except the transverse component which is 10 times smaller than the other two components, and therefore a small discrepancy on the other two components may project into a large discrepancy on the transverse component. Again, the simple clamping of the minimum velocities produces a much worse match.

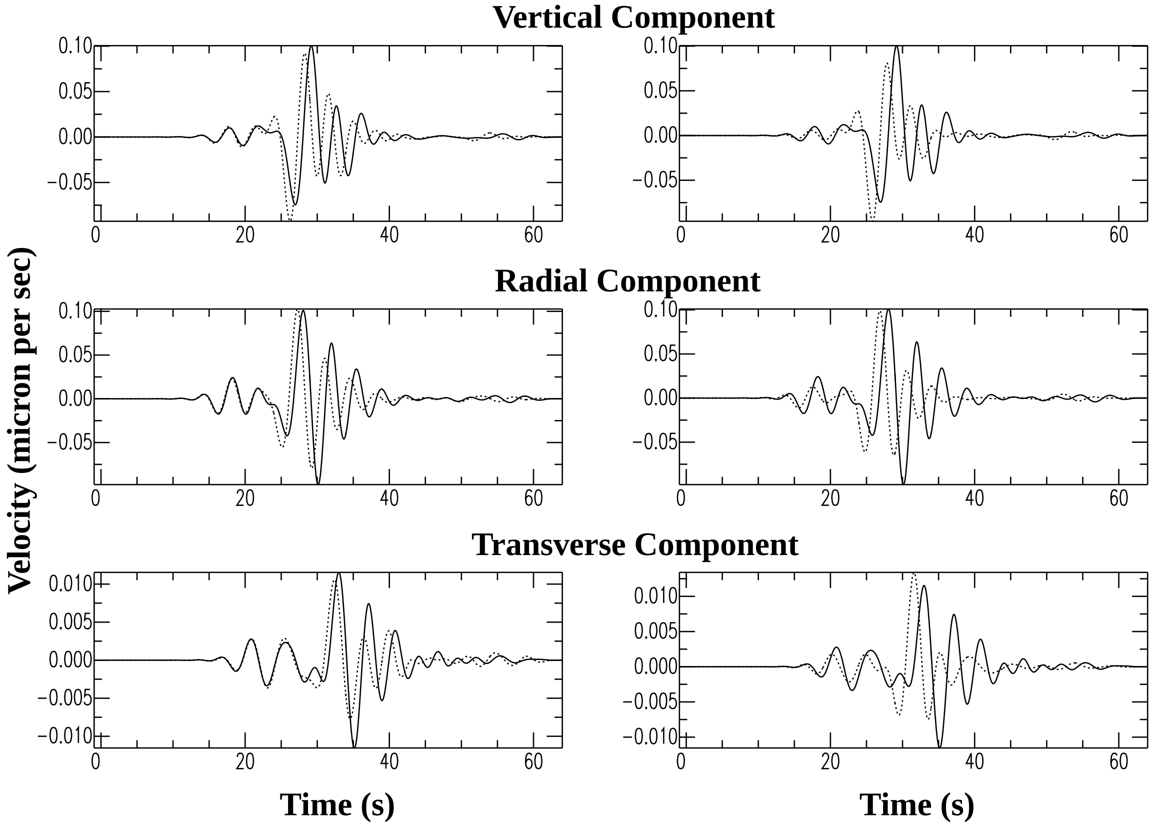

Figure 3.6: Comparison of the synthetic seismograms computed for the original, the EMP, and the velocity clamped models. Three components of velocity (in microns per second) due to a dip-slip double-couple point source situated 2.0 km below the free surface (azimuth 90^o, strike 0^o, dip 90^o, rake 90^o, magnitude $M_w = 1.0$). The source-receiver distance is 22.0 km. In both columns, the solid line is the synthetic seismogram computed for the original model. The dashed line in the left column is the synthetic seismograms computed for the EMP model while in the right column it shows synthetic seismograms computed for velocity clamped model. The models are described in Table 3.1.

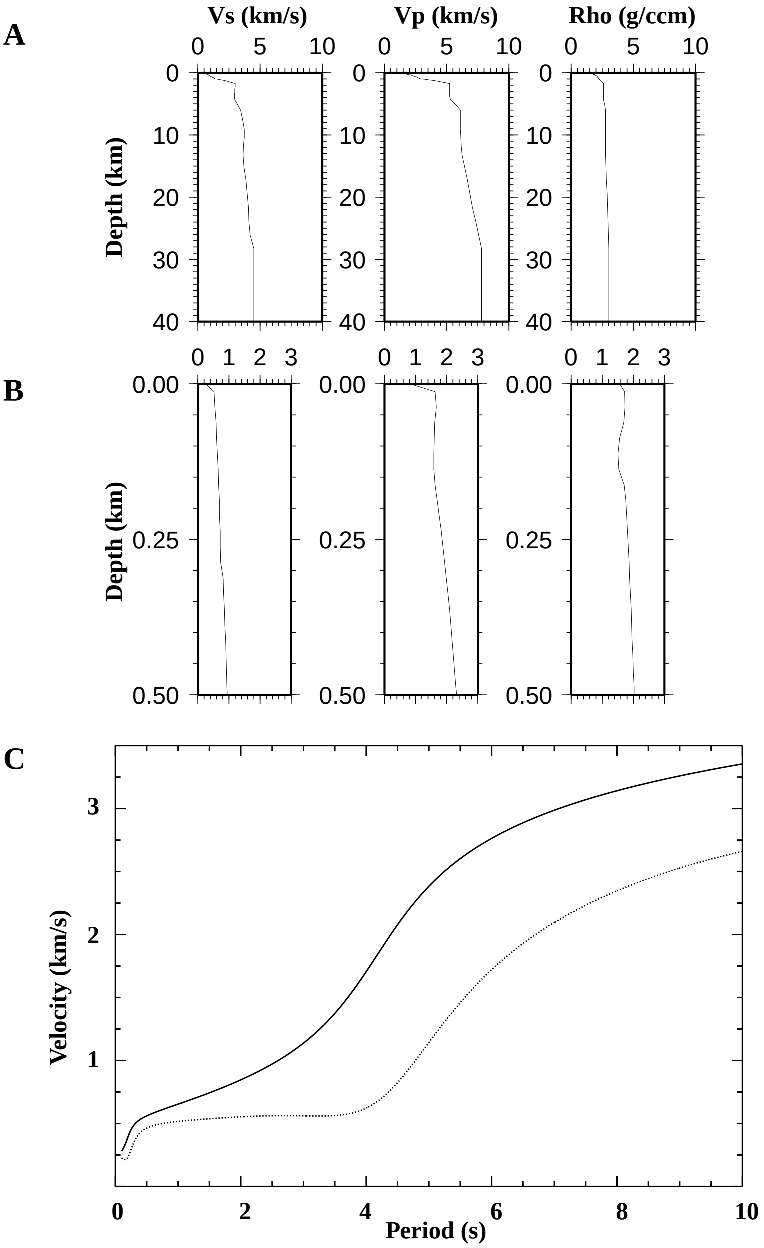

Figure 3.7: Medium parameters and dispersion curve of the vertical velocity profile selected from the SCEC velocity model version 2 (*Magistrale et al.* [2000]) at 33.94^o N and 118.15^o W. A/ Profiles show dependency of the S-wave velocity (Vs), P-wave velocity (Vp), and density (Rho) on depth. B/ The three graphs show a detailed medium parameter vertical profile for the top 0.5 km. C/ The graph shows the dispersion of the Love wave phase (solid line) and Love wave group (dashed line) velocities. Note the Airy phases at 0.15 sec, 2.6 sec and 3.1 sec.

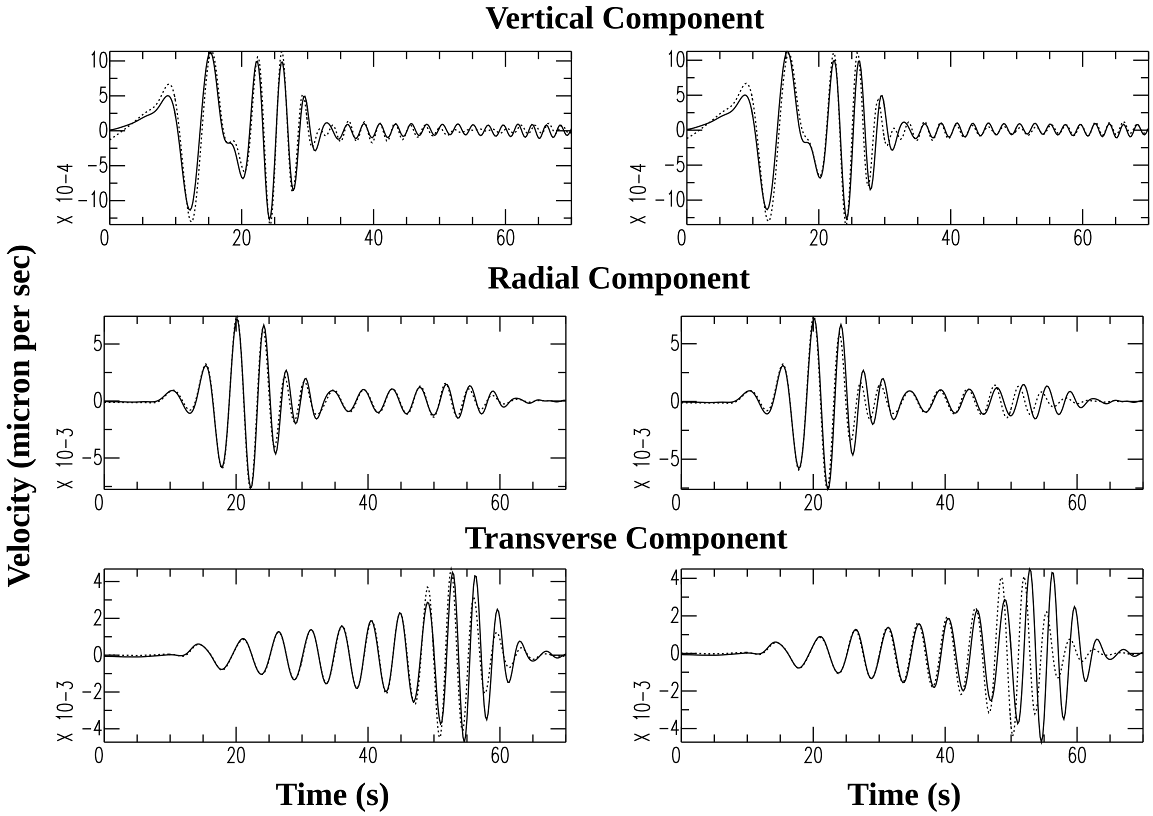

Figure 3.8: Comparison of the synthetic seismograms computed for the original, the EMP, and the velocity clamped models for complex vertical profile. Three components of velocity (in microns per second) due to a strike-slip double-couple point source situated 1.0 km below the free surface (azimuth 40^o, strike 0^o, dip 90^o, rake 0^o, magnitude $M_w = 1.0$). The source-receiver distance is 30.0 km. In both columns, the solid line is the synthetic seismogram computed for the original model of Figure 3.7. The dashed line in the left column is the synthetic seismograms computed for the EMP model of minimum velocity 0.7 km/sec, while in the right column it shows synthetic seismograms computed for velocity clamped model at 0.7 km/sec.

Figure 3.7 illustrates the medium parameters and the dispersion curves for a single vertical profile in the Los Angeles basin from the SCVM (version 2.2, *Magistrale et al.* [2000]). The near surface sedimentary layers cause a sharp drop in all medium parameters with a minimum velocity reaching 250 m/sec. The dispersion curve of Love wave group velocity shows three Airy phases (periods for which the group velocity has a local extreme) at 0.15 sec, 2.6 sec and 3.1 sec. As discussed earlier we can not increase the minimum velocity in the model if the period range of interest contains the overall minimum of the Love wave group velocity ($T = 0.15$ sec). We have modified this model for signals with energy at 3 seconds and longer to have a minimum velocity of 700 m/sec. The relative error of the Love wave group velocity caused by the increased minimum velocity is 5.7% for a period of 3 seconds; therefore, (using equation (3.3)) the seismograms should agree up to 52 seconds.

Synthetic seismograms for a shallow source (1.0 km deep) computed for the original, the EMP and the velocity clamped models are compared in Figure 3.8. We computed the synthetic seismograms with the Thompson-Haskell propagator matrix method (*Haskell* [1953], *Thompson* [1950]). We have tested and compared a large number of source mechanisms, epicentral distances and source depths (the receiver was fixed at the free surface), and this example represents an average fit between the seismograms computed for the original, the EMP and the velocity clamped models. The Airy phase arrival on the transverse component is at approximately 55 seconds (theoretical arrival time of 53.5 seconds). The synthetic seismograms computed for the original and the EMP models agree very well, even for times greater than the predicted 52 seconds. The Airy phase is poorly matched by synthetic seismograms computed for the velocity clamped model.

Finally we tested the method for a simple 3-D heterogeneous medium. We chose a model similar to the microbasin model of Figure 10 of *Saikia et al.* [1994], who pointed out the importance of near surface low velocity zones for full waveform seismograms. Our 3-D model is illustrated in Figure 3.9. The S-wave velocity drops to 0.2 km/sec in the original model. The equivalent medium parameter model has a minimum velocity of 0.5 km/sec and the relative group velocity error caused by this model modification is 0.4 % for a period of 3 seconds. Therefore, we may expect our seismograms to agree for 750 seconds. We use a rectangular shape of the basin model to avoid effects due to a different discretization for the finite-difference grid (the grid for the EMP model is twice as coarse as the grid of original model).

We have simulated the synthetic seismograms at a selected receiver situated at the free surface from 384 point sources for three different source mechanisms (strike slip, 90^o dip slip, and 45^o dip slip). Figure 3.10 shows the synthetic seismograms with the lowest cross correlation coefficient. The late arrivals (20-30 sec) are caused by

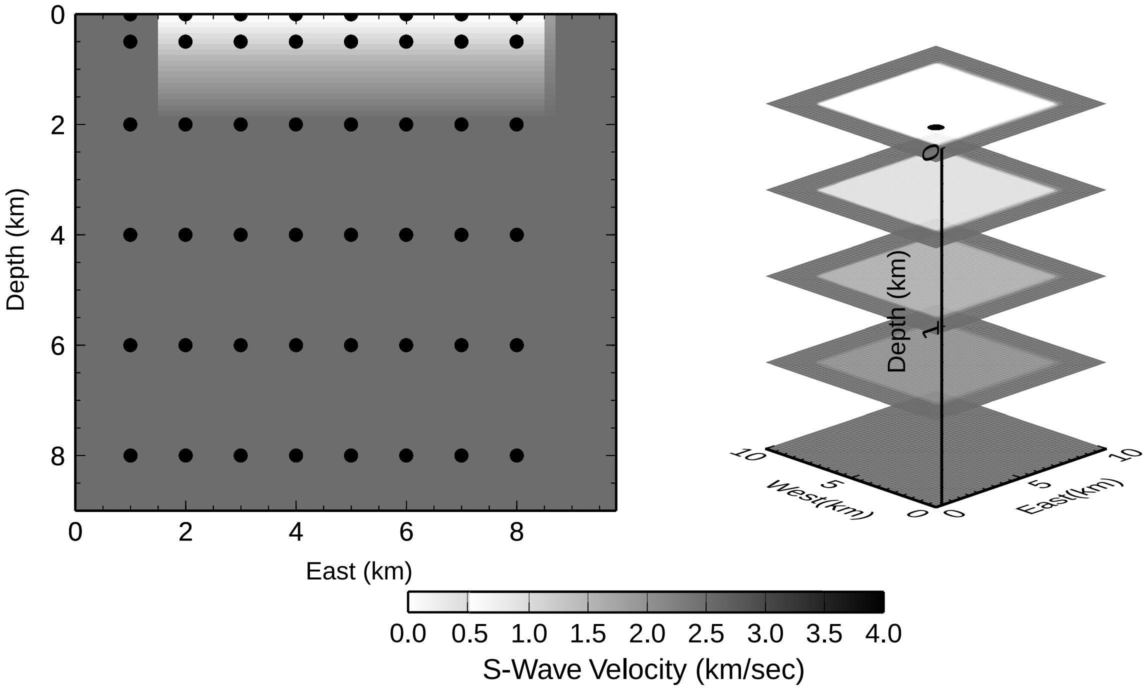

Figure 3.9: The 3-D heterogeneous model used for the 3-D test. The left plot shows S-wave velocity in the East-Depth plane in the center of the model. The black circles represent positions of sources projected on the plane. The right plot illustrates the 3-D structure of the rectangular basin. The black circle at the top represents the position of the receiver.

trapped energy in the basin. The original and the EMP models' seismograms match within a line thickness. The perfect match of the multiply reflected waves inside the low velocity region demonstrates the capability of the method to resample the model for sedimentary basins. The numerical simulation for the EMP model required eight time less computation time and four time less computer memory than the numerical simulation for the original model.

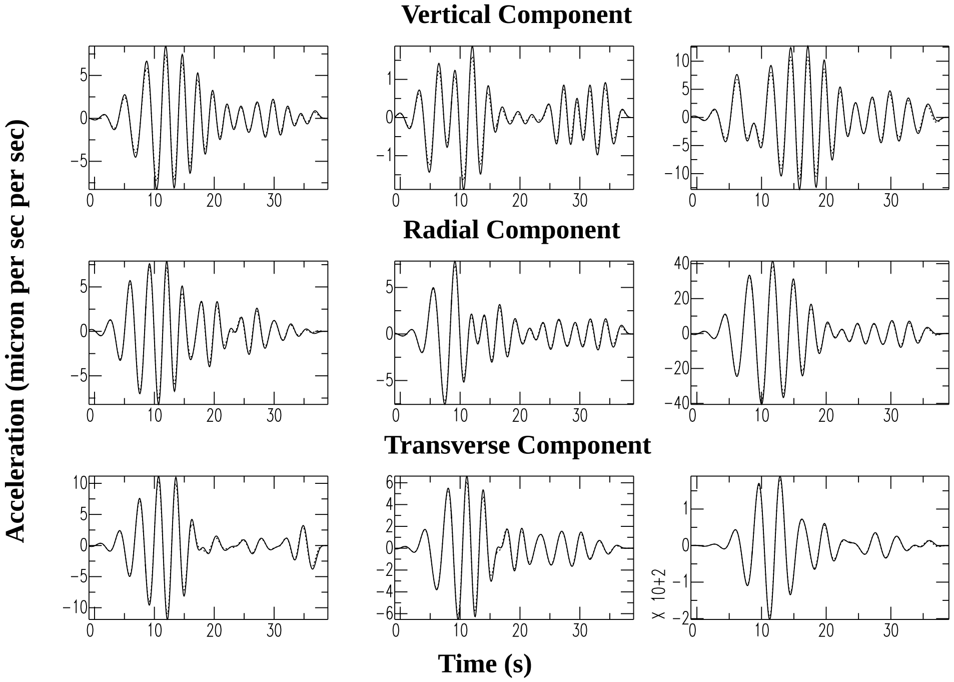

Figure 3.10: Comparison of the synthetic seismograms computed for the original and the EMP for a 3-D model. Three components of acceleration (in microns per second) due to three sources: 90^o dip-slip (left column), 45^o dip-slip (middle column), and strike-slip (right column) double-couple point source. The synthetic seismograms were computed for the model of Figure 3.9. The receiver was situated at the surface at 0.5 km East and 0.5 km North of the edge of the "basin." The source for 90^o dip slip and 45^o dip slip was situated at the depth of 0.5 km and it was 3.5 km North and 0.5 km West of the edge of the "basin." The source for strike slip point source is at the free surface 5.5 km North and 5.5 km East of the edge of the "basin." The solid line represents synthetic seismograms computed for the original model described in Figure 3.9. The dashed line represents synthetic seismograms computed with equivalent medium parameters and minimum velocity 0.5 km/sec.

3.6 Conclusions

The numerical tests show that the synthetics computed for the models with the equivalent medium parameters produce a significantly better match to the synthetics computed for the original models than the synthetics computed for the velocity-clamped models. This allows a significant reduction in model size and computational time required. For the shown example of the 3-D velocity model we have reduced the computational time by a factor of eight and memory requirements by a factor of four. The examples show that the misfit or artifacts introduced by clamping can be quite significant, particularly if one is using late arriving energy. The tests also show that the "t_{prop}" time of equation (3.3) does a good job of predicting the amount of time that will be relatively free of artifacts.

Chapter 4 A full waveform test of the Southern California Velocity Model by the reciprocity method

4.1 Abstract

We apply the reciprocity method (*Eisner and Clayton* [2001]) to compare the full waveform synthetic seismograms with a large number of observed seismograms. The reciprocity method used in the finite-difference modeling allow for the use of high quality data observed from the earthquakes distributed over the wide range of azimuths and depths. We have developed a methodology to facilitate the comparison between data and synthetics using a set of attributes to characterize the seismograms. These attributes are based on the magnitude of the displacement, a scalar quantity representing the three components of a displacement vector. For the Southern California Velocity Model, Version 1 (*Magistrale et al.* [1996]), we have found misfits between data and synthetics for paths traveling outside of the sedimentary basins and the western part of the Los Angeles and San Fernando basins.

4.2 Introduction

With better numerical techniques to evaluate the seismic wave propagation in complex three-dimensional (3-D) heterogeneous media, the need for realistic velocity models arises. *Graves and Wald* [2001] show the necessity of well tested velocity models for source inversions. *Olsen and Archuleta* [1996] and *Eisner and Clayton* [2002] apply finite-difference modeling in a 3-D velocity model to evaluate realistic long period site effects for southern California. However, the outstanding issue is how well the 3-D models describe the earth properties important for the seismic wave propagation. The ultimate test of these models is how well they predict the observed full waveforms. Several studies have used the Southern California velocity models for simulations of Landers (*Olsen et al.* [1997], *Wald and Graves* [1998]) and Northridge (*Olsen and Archuleta* [1996]) earthquakes and compared the full waveforms synthetics to the observed seismograms recorded during these earthquakes.

The current procedure is to evolve the wavefield outward from the source to a suite of observation points and compare the synthetics to the recorded data. This generally means one simulation for each source. We propose a method which will allow us to compare data and synthetics for a large number of source-receiver pairs with one run. By using reciprocal sources we can reduce the amount of calculations when determining synthetics for earthquakes at a few selected high quality stations. Furthermore, we can select stations which have available records for a large number of earthquakes. *Eisner and Clayton* [2001] show the reciprocity method for the above described application and discusses its numerical implementation and accuracy with the finite-difference technique.

We propose to use a large number of small earthquakes computed with a finite-difference technique (*Graves* [1996]) to test the Southern California Velocity Model, Version 1.0, (*Magistrale et al.* [1996]). The simulation of a large number of small earthquakes has several advantages; small earthquakes are generally distributed throughout the entire model, and the spatial distribution of sources enables us to illuminate the model from many azimuths. The depth variation of sources enables us to distinguish between the effects of the shallow and deep earthquakes. By including the weak motion data (small earthquakes) into this test of the velocity model we are able to test regions, where no large earthquake previously occurred, but which are potentially hazardous. Figure 4.1 illustrates the advantage of the proposed method. The velocity model is tested along a large number of the source-receiver paths which cross each other. The path crossing can be used to determine the sources of the discrepancies between the observed and synthetic seismograms.

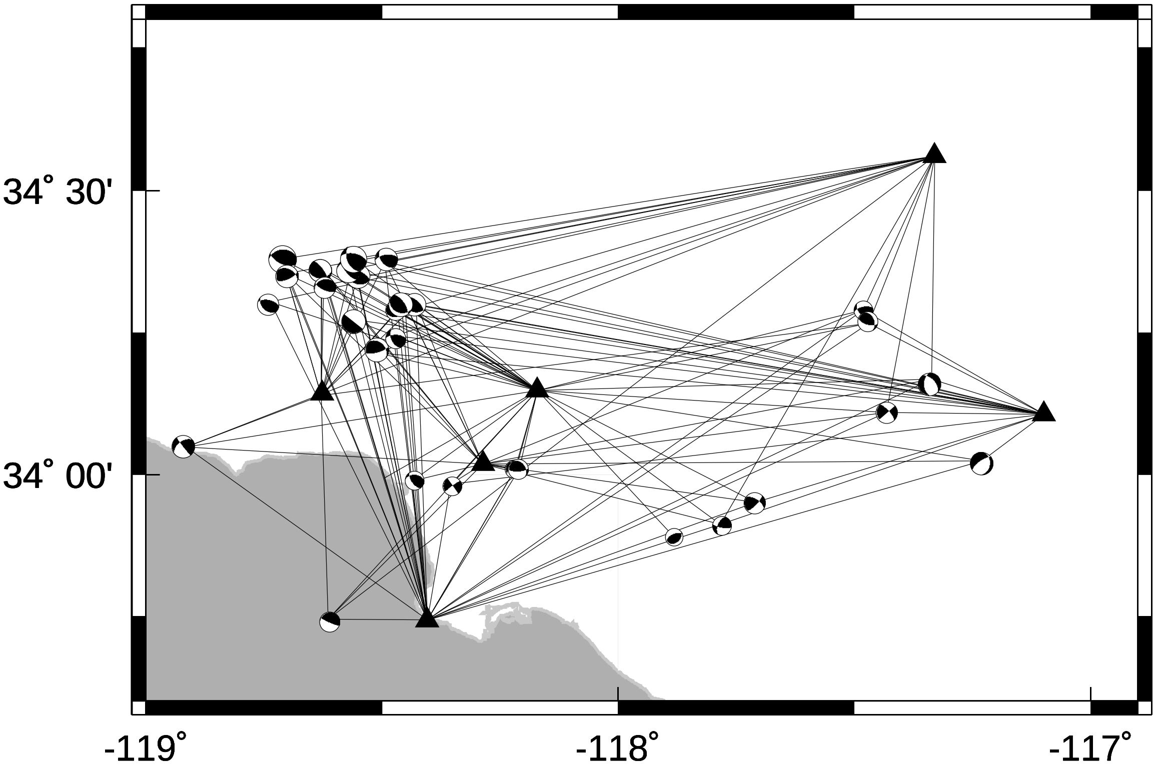

Figure 4.1: Map of southern California showing the selected earthquakes and broadband stations (triangles) with straight lines connecting the epicenters and the receivers of the epicenter-receiver pairs used in the back-projection of the time shifts and coda decay.

Wald and Graves [1998] show that even for the long period data, observations and synthetics do not match in phase and amplitude. The real earth has more complexity than we are likely to be able to include in our model, and hence we do not expect an exact match of synthetics and data. In this study, we are interested in matching the main energy of the synthetic and observed seismograms; therefore the discrepancy between data and synthetics is measured by comparing simple attributes of the seismograms. These discrepancies in attributes can be used to determine the regions of the model that appear to be in error. We propose to determine these attributes from the time history of the displacement magnitude. The magnitude of the displacement provides a simple scalar quantity with which one can monitor timing, amplitude and coda of the seismograms. We chose to characterize the fit between synthetic seismograms and data by measuring the following attributes: the time shift (the shift of the synthetic seismogram for which it best matches the observed seismogram), maximum amplitude and coda decay (the rate at which the amplitude decays to zero). Therefore, a "good fit" in our study is a match of timing, coda decay, and maximum amplitude between the displacement magnitude of the observed and synthetic seismograms.

The previous studies (*Olsen et al.* [1997], *Wald and Graves* [1998], and *Olsen and Archuleta* [1996]) included triggered or incomplete seismograms in order to test the entire model. Since our study is based on weak motion data, we use broadband complete observed seismograms with absolute timing. We also develop a method of interpreting the differences between data and synthetics which is robust and uses the entire three-component seismograms. In this study, we only indicate the regions of the model that are inadequate. We do not attempt to update the model. This study of the Southern California Velocity Model, Version 1, includes the top low-velocity layers which are important for propagation of waves within a period range of interest.

4.3 The testing procedure

We apply the reciprocity method to simulate multiple sources recorded at a few receivers to reduce the amount of calculations. By invoking reciprocity, the number of simulations can be reduced to three times the number of receivers (*Eisner and Clayton* [2001]). This method can also provide suites of source mechanisms and locations. For the example here, with 6 receivers and 32 sources (Figure 4.2), we need only 18 simulations versus 32 simulations using the forward technique. If we had also wanted to include a variable double-couple mechanism for the point-source, the reciprocity method would still have required only 18 simulations versus 160 (5 moment tensor elements times 32 source locations) simulations with the direct method. Source relocation would further increase the cost of the direct method but not of the reciprocal method.

We develop a new set of measurements to characterize the misfit. We use the magnitude of the displacement (MOD, vector length of all 3 components) as our basic measure

$$MOD(t) = \sqrt{u_{rad}^2(t) + u_{tra}^2(t) + u_{up}^2(t)}. \tag{4.1}$$

Here $MOD(t)$ is the time history of MOD and $u_{rad}(t), u_{tra}(t), u_{up}(t)$ are the time histories of the individual components. Use of the MOD is convenient, because it allows a scalar quantity to represent the complexity of a vector, and it is particularly useful in 3-D heterogeneous media where there is no simple decomposition of the seismogram into distinct phases, such as SV or SH, or surface waves such as Love or Rayleigh waves. It is a convenient measure of the first-order fit between data and synthetics that is sensitive to the traveltime, amplitude and strength of coda. Furthermore, the MOD is not zero in the nodal direction of the radiation pattern, making it more suitable for comparison of amplitude ratio of data over synthetics. An entire three-component seismogram can be described by three time dependent spherical coordinates (an MOD, a particle motion's azimuth and a particle motion's declination). The azimuth and the declination depend on the direction from which a wave arrives and the type of the wave. In this study we are primarily interested in whether the model sufficiently represents the real earth so that we can reproduce main scattered waves in our numerical simulations. Consequently, we have chosen to base our comparison on measuring characteristics of the MOD, as it is more sensitive to the propagation effects of the large energy arrivals in a seismogram than the smaller arrivals. Beside MOD there are other variables suitable for measuring a fit between the data and synthetic seismograms in a 3-D space (e.g. measuring absolute distance between particle motion in the synthetic and the observed seismograms); however, MOD conveniently describes the criteria of the fit we were interested in: the timing, the coda decay and the maximum amplitude.

The MOD time histories of the real and synthetic data are compared by correlation to obtain the maximum crosscorrelation and the time shift at which the maximum occurs. The value of the maximum crosscorrelation determines the quality of the fit between data and synthetics. Since the crosscorrelation of the MODs is a crosscorrelation of the two positive functions, the mean value of the crosscorrelation is 0.5. The time of the maximum correlation is a time shift of the synthetic seismogram for which it best matches the observed seismogram. Note that this definition of the time shift does not depend on an *a priori* selection of phases. Since the correlation is dominated by the maximum amplitude, we are likely determining the variations in surface-wave group velocities. However, this interpretation depends on the distance between the source and the receiver, source depth, source mechanism and several other parameters. The time shift between synthetics and the data is caused by the velocity deviation in the model between the source and the receiver. A source mislocation should not appear as a consistent time delay in our model as the earthquakes are located by a very dense network of the stations and time delays due to the mislocation are lower than time delays observed in this study. The noise in the observed seismograms or mismatch between the data and the synthetics may cause the crosscorrelation to peak at a time shifted by a dominant period (cycle-skip). Therefore, the crosscorrelation is tapered for time shifts longer than the dominant period of the signal to avoid this. We taper the crosscorrelation function for times longer than the shortest period used in our signal (no shorter period can be a dominant period). We can invert the time shifts for a slowness variation with a tomographic method to show which parts of the model are most likely in error. Assuming most of the energy in the data and the synthetic seismograms travels along a straight line between the source and the receiver, we chose a simple back projection method to map the time shifts into lines connecting corresponding epicenters and receivers. This is a simplification of the actual ray paths, but it gives us a good estimate regarding which regions of the model cause systematic time shifts.

To invert we divide the model into cells and the average slowness deviation of the i-th cell is determined by a simple inversion of the time shifts:

$$ds_i = \frac{\sum_j (L_{ij} dt_j)}{P_i + D}. \tag{4.2}$$

Here ds_i is a slowness deviation in $i-th$ cell, dt_j is the time shift of the $j-th$ epicenter-receiver pair, L_{ij} is the length of the straight line between the $j-th$ epicenter-receiver pair in the $i-th$ cell, D is damping, and $P_i = \sum_j L_{ij} L_{ji}$.

To measure the coda decay, we use a sliding window average (*Montalbetti and Kanasewich* [1970]) of MOD. An exponential decay of the form

$$M(t) = M_0 \cdot e^{-b \cdot |t - t_0|}, \quad \text{for} \quad t \geq t_0 \tag{4.3}$$

is fitted for the time $t \geq t_0$ by least squares. Here t_0 is the time of the maximum of the $MOD(t)$, $M(t)$ is the sliding window averaged $MOD(t)$, b characterizes the decay of the coda, and M_0 is the maximum of the $M(t)$: $M_0 = M(t_0)$. The exponential decay of the $M(t)$ can be derived from the exponential decay of the energy at a seismogram computed for a random isotropic scattering medium (*Zeng et al.* [1991]). Based on observation of the exponential decay of coda in data, we use this rate of decay as a first-order approximation for the coda decay of the long period signal.

We compare the coda of the synthetics and the data by comparing the decay of synthetics and the data if the maximum crosscorrelation is above 0.8. This level ensures we are looking at differences in coda decay and not simply misfit of entire seismograms. The coda is a measure of the complexity of the model, and we interpret it in the following way: if b is larger for the synthetics than for the data, then our model does not generate enough coda and is lacking in complexity; if b is larger for the data than the synthetics, our model is too complex and generates too much coda. Assuming small-angle scattering (*Wu and Aki* [1988]) we may estimate that the sources of the observed scattering occur along a straight path between the epicenter and the receiver. An exact inversion for the scattering sources is beyond the scope of this study, but the proposed method identifies the regions of the model which consistently cause a discrepancy in the scattered energy between synthetics and data. An analogous back projection can be used to identify these regions in the analogous manner as with the time shift anomalies:

$$dE_i = \frac{\sum_j (L_{ij} de_j)}{P_i + D} \quad \text{where} \quad de_j = \left(\frac{b_j^{data} - b_j^{synt}}{\sqrt{b_j^{synt} b_j^{data}}} \right). \tag{4.4}$$

Here b_j^{synt} and b_j^{data} are determined from the fit of the synthetics and data (respectively) of equation (4.3), and dE_i is a relative error of the b value per distance in the $i - th$ cell. The regions with positive dE_i are areas with too much scattering in the model and vice versa.

The last attribute we compare is M_0, the maximum of the $MOD(t)$, which characterizes the overall source strength and model amplification. *Olsen and Archuleta* [1996] and *Wald and Graves* [1998] have shown the model amplification is well predicted by the 3-D velocity model for well constrained sources of large earthquakes. That is, they fit the maximum amplitudes within a factor of 2 between the data and the synthetics. As we have observed larger discrepancies of the maximum amplitude, we assume that the ratio of the maximum amplitude of the synthetics to data is not on average biased due to the 3-D velocity model, and we interpret it as a bias due to the strength (magnitude) of the source. For each earthquake we compute the ratio of the maximum the $MOD(t)$ of the synthetics to data over all stations. We average these ratios over all stations used in a study. If the averaged ratio deviates significantly from 1.0, the estimated source magnitude is incorrect. Values larger than 1.0 can be interpreted as overestimated magnitude and values smaller than 1.0 can be interpreted as underestimated magnitude of an earthquake source.

4.4 Application to the Southern California velocity model

The reciprocity method and the measurement of the attributes discussed in the previous section are now applied to test the Southern California Velocity Model (SCVM), Version 1 (*Magistrale et al.* [1996]). The model consists of geology-based sedimentary basins placed in a 1-D (*Hadley and Kanamori* [1977]) background medium. Note that the sedimentary basins have a very irregular shape and therefore the synthetic seismograms computed in this model are very sensitive to the source location.

Figure 4.2 and Table 4.1 show the selected earthquakes and their parameters (respectively) used in this study. The earthquakes represent the best spatial distribution of small earthquakes with a good signal to noise ratio in periods of 3 seconds and longer. At shorter periods smaller velocity variations cause discrepancies between the data and synthetics, but this is compensated by having more earthquakes that have a good signal to noise ratio and thus improving the test of the velocity model. We use a triangular moment rate source time function of 3 seconds length in the modeling of the synthetic seismograms. The instrument response is removed from the observed data.

We have not inverted for source location or mechanism in our study because we use only a limited number of stations and therefore we would introduce an artificial bias due to station distribution. We use two catalogues of earthquake parameters: the primary catalogue of *Zhu and Helmberger* [1996] for 26 earthquakes with magnitude $5.5 > M_w > 3.4$ and a secondary catalog of earthquakes parameters of *Hauksson* [2000] for 6 earthquakes not listed by *Zhu and Helmberger* [1996]. *Zhu and Helmberger* [1996] use surface waves and body waves to determine earthquake mechanisms and locations in a 1-D velocity model of southern California. *Hauksson* [2000] uses direct first motion arrivals of P and S waves in laterally heterogeneous model based on tomographic inversion. The catalogue of *Hauksson* [2000] lists also source parameters of the catalogue of *Zhu and Helmberger* [1996]; therefore, we could compare the full waveform fit to the data for the source parameters listed in both catalogues. We

Selected Earthquakes

Earth. name	Lat $(^o)$	Lon $(^o)$	Depth (km)	Strike $(^o)$	Dip $(^o)$	Rake $(^o)$	M	Date yyyy/mm/dd	source
E00	34.29	-117.48	11.1	258	61	52	3.40	1993/05/18	ZH
E01	34.29	-118.47	12.4	71	34	47	3.54	1994/01/19	ZH
E02	34.22	-118.51	14.8	74	72	61	4.12	1994/01/19	ZH
E03	34.27	-118.56	13.3	34	0	-4	4.15	1994/01/27	ZH
E04	34.38	-118.49	5.0	264	59	51	3.93	1994/01/28	ZH
E05	34.38	-118.71	13.3	266	34	65	4.95	1994/01/19	ZH
E06	34.35	-118.55	10.3	291	58	90	4.25	1994/01/24	ZH
E07	34.27	-117.47	11.3	104	62	58	3.50	1995/04/04	ZH
E08	33.74	-118.61	21.0	244	10	41	3.65	1995/03/01	ZH
E09	34.16	-117.34	9.8	181	48	-56	4.03	1997/06/28	ZH
E10	33.95	-117.71	9.9	43	75	32	3.75	1998/01/05	ZH
E11	34.02	-117.23	16.6	235	70	-68	4.09	1998/03/11	ZH
E12	34.24	-118.47	14.6	272	60	47	3.61	1994/01/18	ZH
E13	34.36	-118.57	8.9	279	30	51	4.19	1994/01/19	ZH
E14	34.30	-118.74	10.6	283	56	72	3.79	1994/01/19	ZH
E15	34.36	-118.63	13.6	71	72	49	4.02	1994/01/24	ZH
E16	34.36	-118.63	16.4	84	32	35	4.10	1994/01/24	ZH
E17	34.30	-118.45	11.1	103	24	61	4.07	1994/01/21	ZH
E18	34.30	-118.43	9.9	107	32	69	4.00	1994/01/23	ZH
E19	34.30	-118.46	10.7	111	29	60	4.17	1994/01/21	ZH
E20	34.38	-118.56	10.6	281	57	51	4.72	1994/01/18	ZH
E21	34.33	-118.62	15.8	257	27	57	3.88	1994/01/18	ZH
E22	34.35	-118.70	16.9	65	66	59	3.96	1996/05/01	ZH
E23	34.11	-117.43	5.6	48	90	16	3.68	1997/10/14	ZH
E24	33.91	-117.78	9.0	203	54	21	3.41	1997/01/31	ZH
E25	34.01	-118.21	12.9	120.0	55.0	130.0	3.1	1999/05/03	H
E26	34.01	-118.22	13.1	330.0	85.0	-150	3.0	1999/06/01	H
E27	34.01	-118.21	12.5	85.0	70.0	60.0	3.5	1999/05/30	H
E28	33.89	-117.88	5.1	45.0	35	70	3.0	1998/01/07	H
E29	33.98	-118.35	4.0	235	85	0	3.3	1997/04/04	H
E30	33.99	-118.43	13.8	145	60	120	3.4	1994/12/11	H
E31	34.05	-118.92	18.8	236	50	5	4.01	1995/02/19	ZH

Table 4.1: List of the selected earthquakes: Latitude (Lat), Longitude (Lon), Depth of the event, Strike, Dip and Rake use convention of *Aki and Richards* [1980], M is a magnitude of an earthquake, and ZH denotes source parameters determined by *Zhu and Helmberger* [1996], H by *Hauksson* [2000].

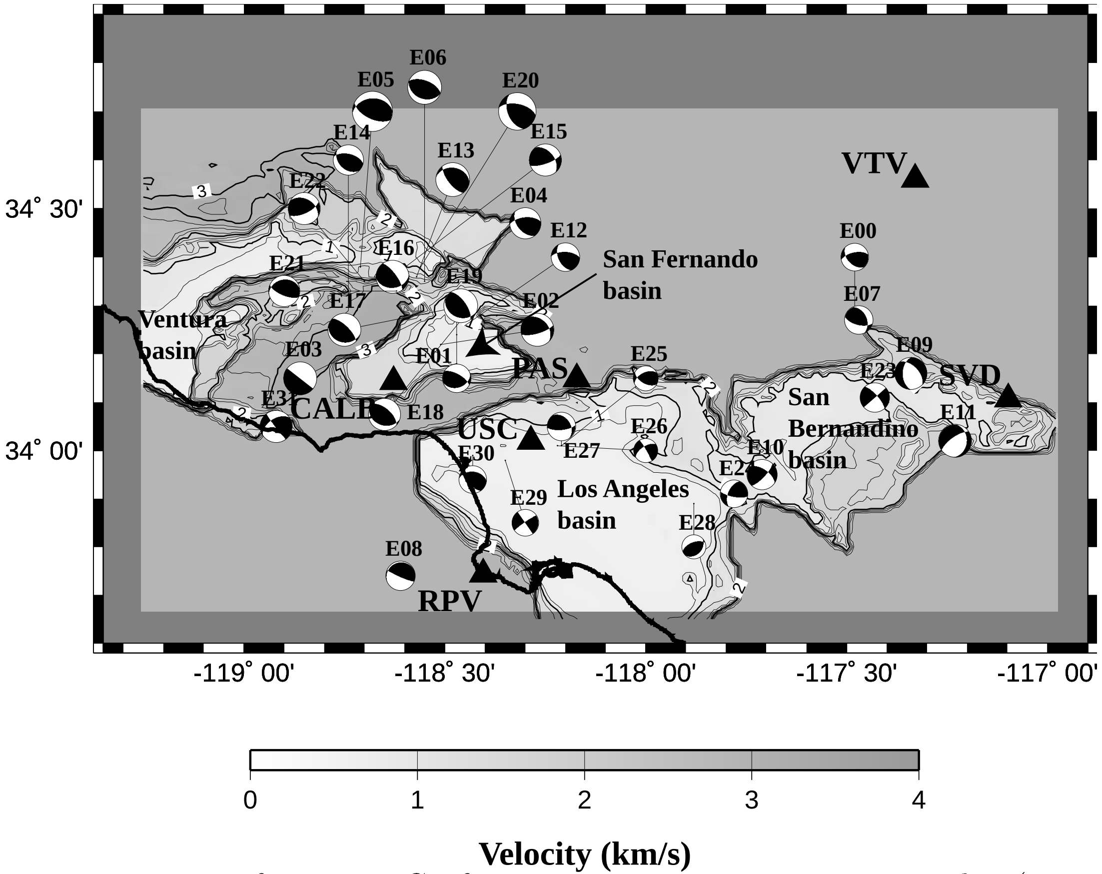

Figure 4.2: Map of southern California showing the selected earthquakes (see Table 4.1), and broadband stations (triangles) for the test of the Southern California Velocity Model, Version 1 (*Magistrale et al.* [1996]). The shading and contours correspond to the Love wave group velocity of 3 seconds period. The contours are labeled at 1.0 and 2.0 km/sec and the contour interval is 0.25 km/sec. Four stations: Pasadena (PAS), Rancho Palos Verdes (RPV), Calabasas (CALB) and University of Southern California (USC) are situated in or near the deep parts of the Los Angeles and San Fernando basins. Two stations, Victorville (VTV) and Seven Oaks Dam (SVD), are outside of the major basins.

found that the source parameters of *Zhu and Helmberger* [1996] fit the data better, especially the surface waves.

The lowest velocity in the model is clamped at 0.5 km/sec to allow the surface waves of 3 second and longer periods to maintain the same group velocities between the values in the velocity clamped and the original models. The velocity clamping at 0.5 km/sec replaces all velocities lower than 0.5 km/sec with 0.5 km/sec. For the SCVM, Version 1, only the S-wave velocities were clamped with the value of 0.5 km/sec in the top 600 meters. The simple velocity clamping is not the best method to preserve the surface-wave velocities for a velocity model (see *Eisner and Clayton* [2001b] for a detailed analysis); however, if the velocity clamping value (0.5 km/sec in this case) is sufficiently lower than the group velocities of the original model, it approximately maintains the same group velocities as in the original model. Figure 4.2 shows the Love wave group velocities in the SCVM, Version 1. The slowest regions of the Love wave group velocities are between 0.5 km/sec and 0.75 km/s for the period of 3 seconds (the minimum is exactly 0.51 km/sec at 34.197^oN latitude and 118.332^oW longitude). Therefore, the wavelength of the surface waves propagating in the sedimentary basins is 1.5–2.1 km. We do not use attenuation in our modeling, since it is not part of the SCVM, Version 1. The attenuation would decrease the amount of the coda in the synthetic seismograms, which already tends to be underestimated by the model.

4.4.1 The analyses of individual source-receiver pairs

In this section we show examples of the fit between the synthetics and the data. Figure 4.3 shows an example of a good fit of synthetics to data in the presence of strong lateral heterogeneity between the earthquake E10 and the station PAS. The synthetic seismograms reproduce the late scattered arrivals fairly well on all components. The maximum crosscorrelation is at 0.92 and the time shift is 1.4 seconds indicating that the model is slower on average than the data. The amplitude ratio of synthetics to data is 2.3 indicating the moment magnitude for this earthquake is overestimated (the average moment for the earthquake E10 is overestimated by the factor of 1.7). The coefficient of the decay is 30% larger for the synthetics.

Figure 4.4 shows another example of a good fit for the earthquake E24 at the station VTV. This example demonstrates the advantage of using the MOD to compare the synthetic seismograms and the data as the signal to noise ratio on the MOD component is better than on any of the vertical, radial or transverse components. This is also an example of the data with the worse signal to noise ratio used for the inversion of the coda decay, maximum amplitude, or time shifts. The value of the

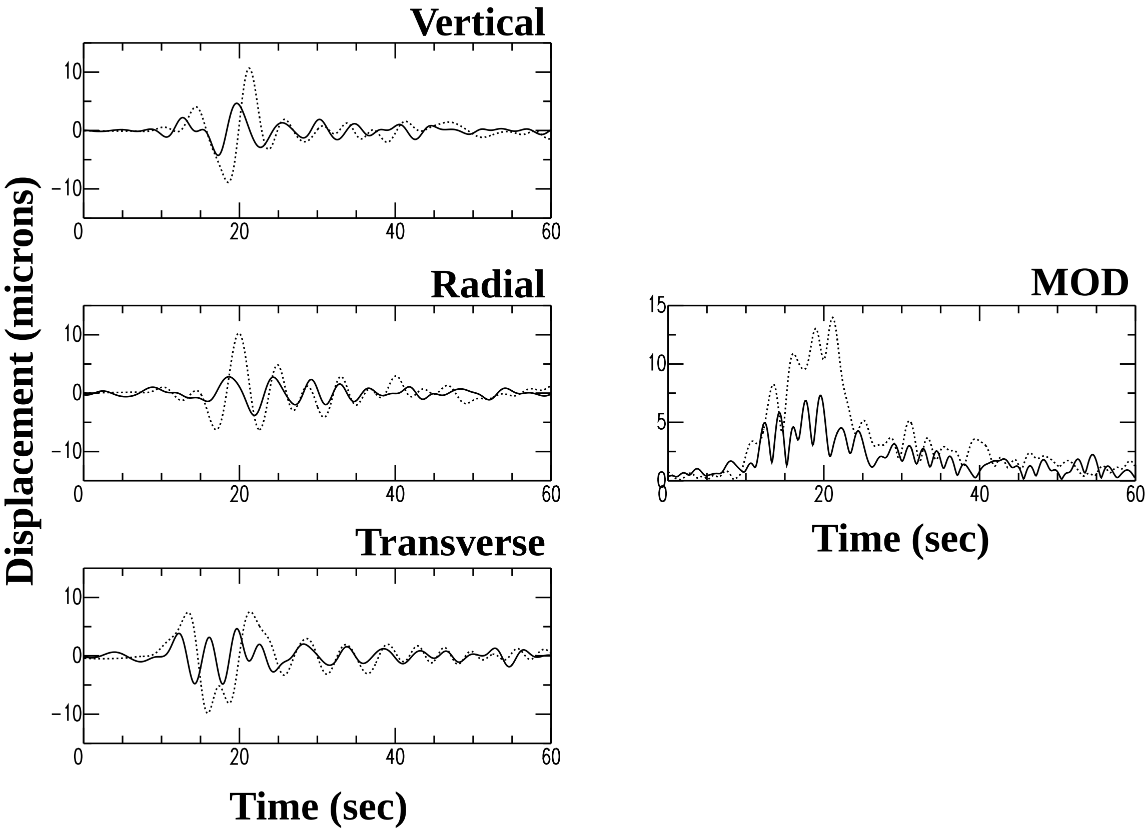

Figure 4.3: Example of a good fit between data and the synthetics for the earthquake E10 recorded at the station PAS (see Table 4.1). The seismograms show displacement in microns. Both synthetic seismograms and data are filtered between 3 and 20 seconds and the instrument response was removed. Data shown by solid line; synthetics by dashed line.

maximum crosscorrelation is 0.92 and the time shift is +0.25 sec. The amplitude ratio of synthetics to data is 1.25. The coefficient of decay is 10% larger for the synthetics. The synthetic seismograms match the timing and phase of the surface waves (time 30-40 seconds) well and no significant scattered energy arrives after the main pulse in either the observed and the synthetic seismograms.

Figure 4.5 shows the comparison of seismograms where there are significant discrepancies between the synthetics and data for the station RPV and the earthquake E13. The first arrivals (15-30 sec) match in phase, timing and amplitude on all components extremely well; however, the later phases of data and synthetics diverge. The synthetic seismograms do not show large arrivals after 35 seconds, but the data show

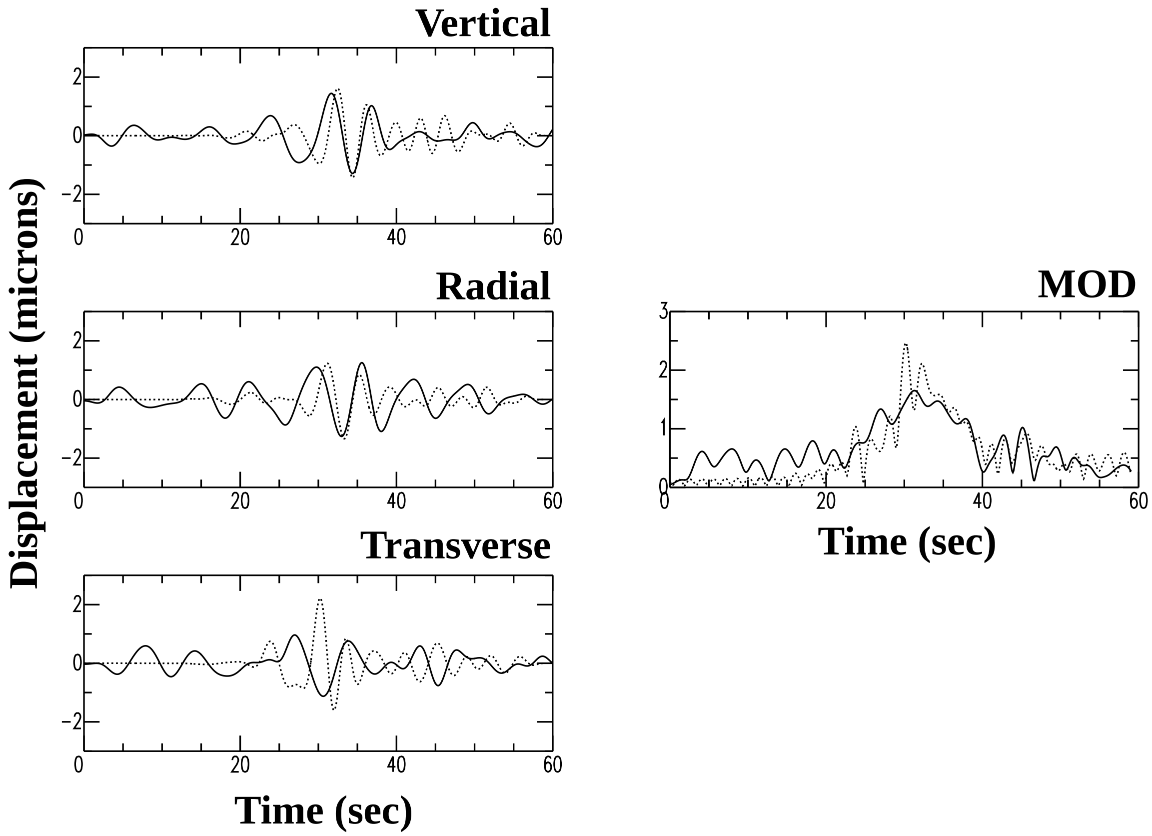

Figure 4.4: Example of a good fit between data and the synthetics for the earthquake E24 recorded at the station VTV (see Table 4.1). The seismograms show displacement in microns. Both synthetic seismograms and data are filtered between 3 and 20 seconds and the instrument response was removed. Data shown by solid line; synthetics by dashed line.

many large arrivals. The hypocenter of the earthquake E13 is at a shallow depth (8.9 km) and therefore the earthquake excite surface waves. These waves propagate through the strongly heterogeneous San Fernando and western part of the Los Angeles basins before they are observed at the station RPV. The lack of scattered energy in the synthetic seismograms indicates these basins may be too simple in the velocity model. The maximum value of the crosscorrelation is 0.87 and it is shifted by -1.5 seconds. The amplitude ratio is 0.84 and the coefficient of decay is 80% larger for the synthetics.

Figure 4.6 shows the comparison of data and synthetic seismograms at the station SVD for a shallow earthquake E04. The direct S-wave and the surface waves (40+

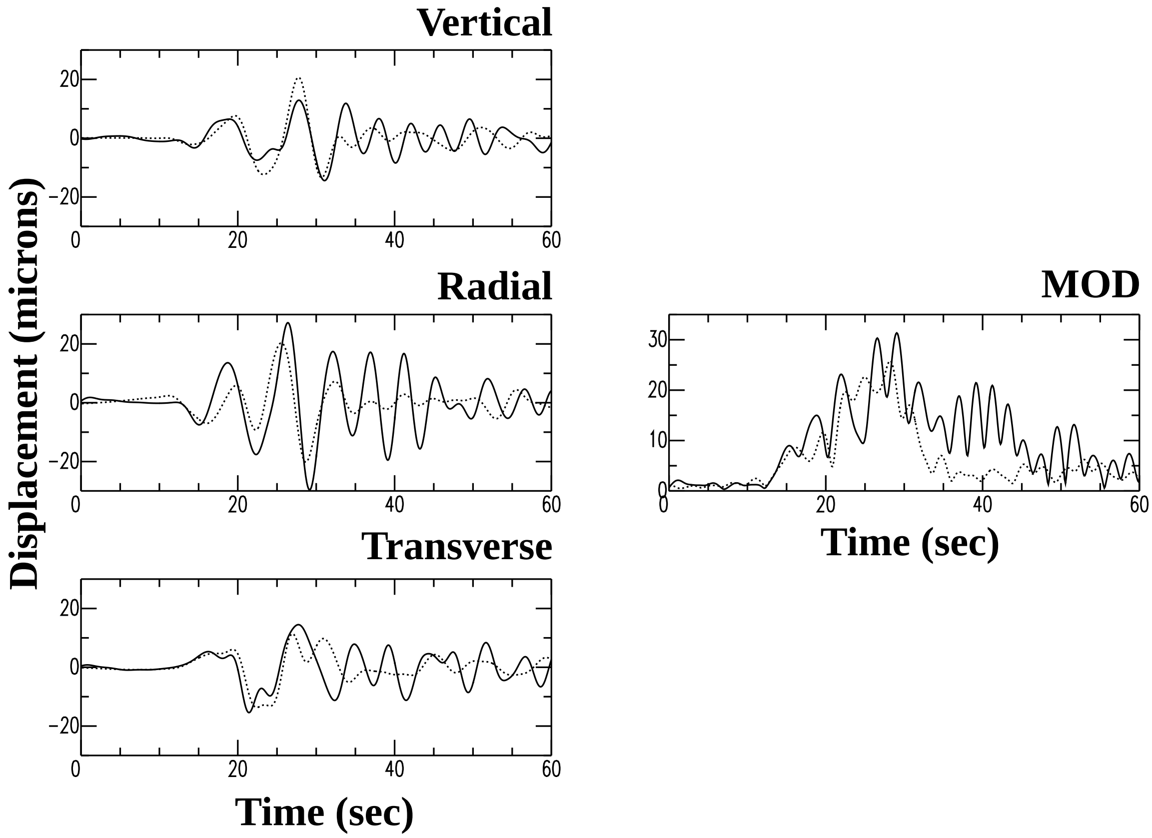

Figure 4.5: Example of a poor fit between the data and the synthetics for the earthquake E13 recorded at the station RPV (see Table 4.1). The seismograms show displacement in microns. Both synthetic seismograms and data are filtered between 3 and 20 seconds and the instrument response was removed. Data shown by solid line; synthetics by dashed line.

sec) arrive ahead of the data. The latter arrivals observed in the data show also more complexity not reproduced in the velocity model (50+ sec). A large portion of the path between the earthquake E04 and the station SVD is outside of the sedimentary basins and therefore the likely explanation of the timing shift is the fast background model (as was also observed by *Wald and Graves* [1998]). The lack of coda (50+ sec) in the synthetic seismograms indicates the background model should also have more complexity in order to explain the data. The maximum value of the crosscorrelation is 0.81 and it is shifted by -1.8 sec. The amplitude ratio is 1.7 and the coefficient of decay is 400% larger for the synthetics.

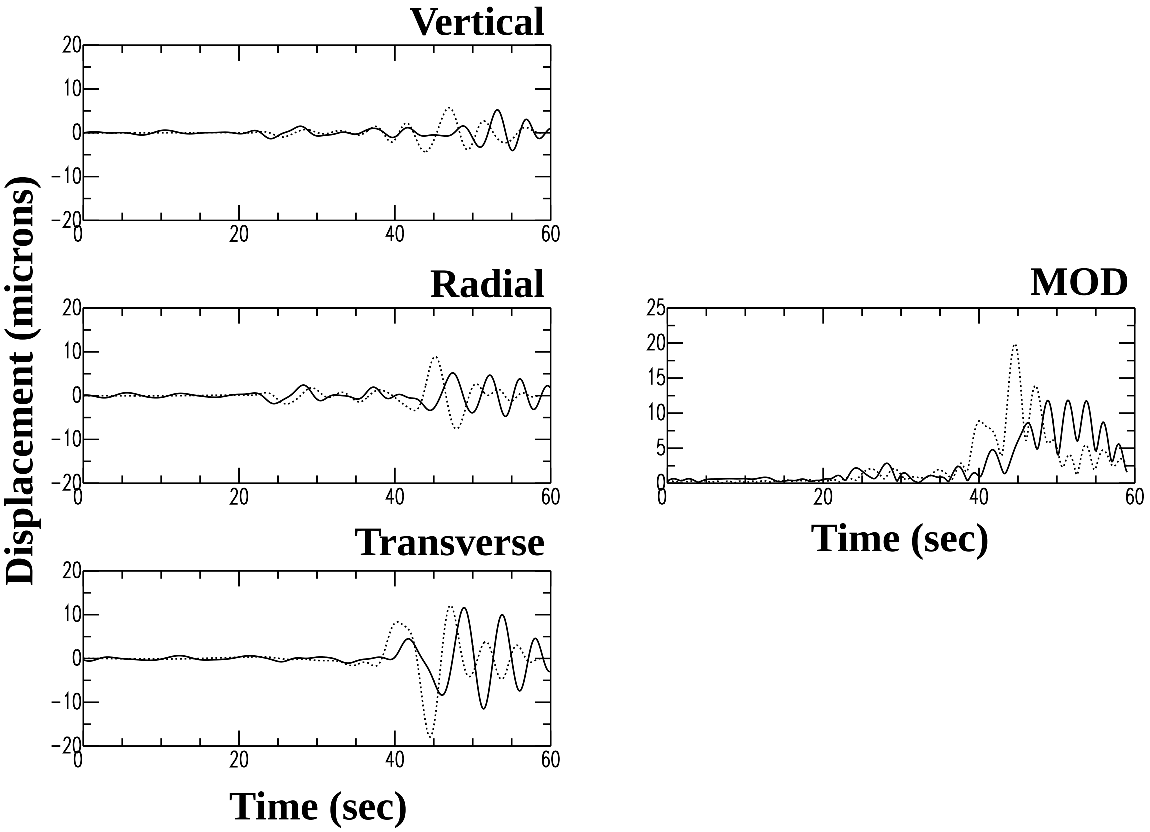

Figure 4.6: Example of a poor fit between the data and the synthetics for the earthquake E04 recorded at the station SVD (see Table 4.1). The seismograms show displacement in microns. Both synthetic seismograms and data are filtered between 3 and 20 seconds and the instrument response was removed. Data shown by solid line; synthetics by dashed line.

4.4.2 Errors of the velocity model

Finally we have used the back-projection techniques described in section 4.3 to summarize the comparison of all the synthetic and observed seismograms. We have used only seismograms with maximum crosscorrelation higher than 0.8 within a maximum time shift of 3 seconds. The coda decay was measured for the sliding 3 seconds long window average of $MOD(t)$. The back-projections of equations (**??**) and (**??**) are damped for both the time shift inversion ($D = 8.1\ 10^{-5} km^{-2}$) and the coda inversion ($D = 8.1\ 10^{-6} km^{-2}$).

Figures 4.7, 4.8, and 4.9 show a summary of the comparison of maximum amplitude, coda decay and time shift between the observed and synthetic seismograms.

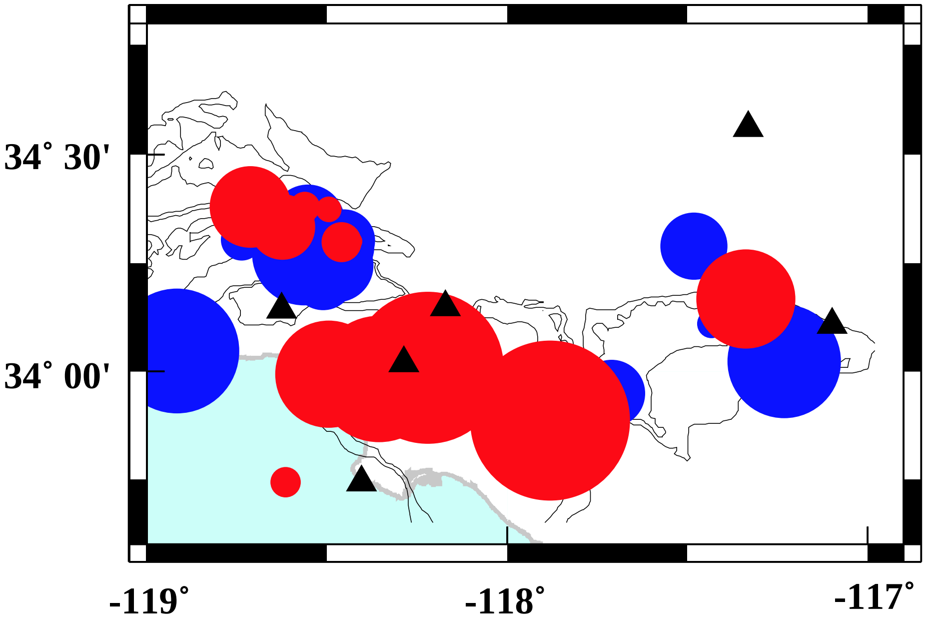

Figure 4.7: Summary results of comparison of the synthetic and observed seismograms. The map shows result of maximum amplitude comparison: The red circles correspond to the underestimated magnitude of an earthquake on average, the blue circles correspond to overestimated magnitude of an earthquake on average. The larger the circle, the larger the discrepancy. A circle of a radius zero – not printed – corresponds to perfect fit. The largest circle corresponds to 4.2 times on average underestimated maximum amplitude. The contours correspond to the Love wave group velocity for a period of 3 seconds.

The map of Figure 4.7 shows the maximum amplitude comparison is dominated by the three underestimated earthquakes in the Los Angeles basin, but several factors may have biased the comparison of these amplitudes. The overestimated magnitude of the most western earthquake may have been caused by complex 3-D coastal structure neglected in the 1-D velocity model used for the source magnitude inversion. There also seems to be a systematic bias to underestimate earthquakes to the north of the San Fernando basin and overestimate earthquakes with a hypocenter depth beneath the San Fernando basin (earthquakes north of 34^{o}N latitude and west of 118.5^{o}W longitude). We attribute this effect to a discrepancy of the inversion for source parameters in 1-D medium with a 3-D basin focusing (north of the San Fernando basin) and defocusing (below the San Fernando basin) of the energy.

The map of Figure 4.8 shows results of the coda analysis. The map is dominated by

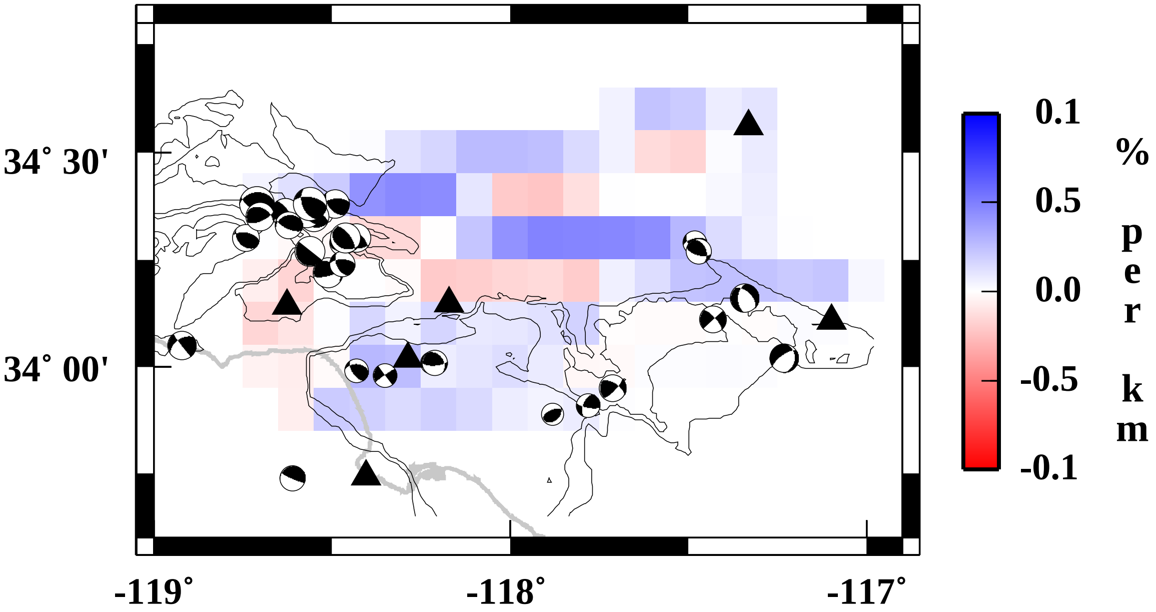

Figure 4.8: Summary results of comparison of the synthetic and observed seismograms. The map shows result of coda back-projection: the blue color corresponds to lack of the coda generated by the model, and the red color corresponds to too much coda generated by the synthetic model.

the areas for which the tested model lacks coda. Including attenuation would further increase this discrepancy and hence our measurement is a lower bound. Therefore, the model would need even more complexity in order to explain the observed data. The lack of coda in the western part of Los Angeles and San Fernando basins and to the north of the Los Angeles basin reflects a lack of complexity in the velocity model. The small discrepancies in the model of the central Los Angeles basin and San Bernardino Basin show that on average the model is properly modeling the complexity observed in data. The coda discrepancy is most likely caused by the surface-wave scattering. However, some artifacts may be caused by a poor coverage of crossing paths as can be seen in Figure 4.1. Also these results should not be considered to be an inversion but rather identification of regions which are sources of discrepancies between the observed and synthetic seismograms.

The map of Figure 4.9 shows that the velocity model is too fast in the western part of the Los Angeles basin and to the north of the Los Angeles basin. This result is consistent with the results of the coda tomography. We interpret that this consistent

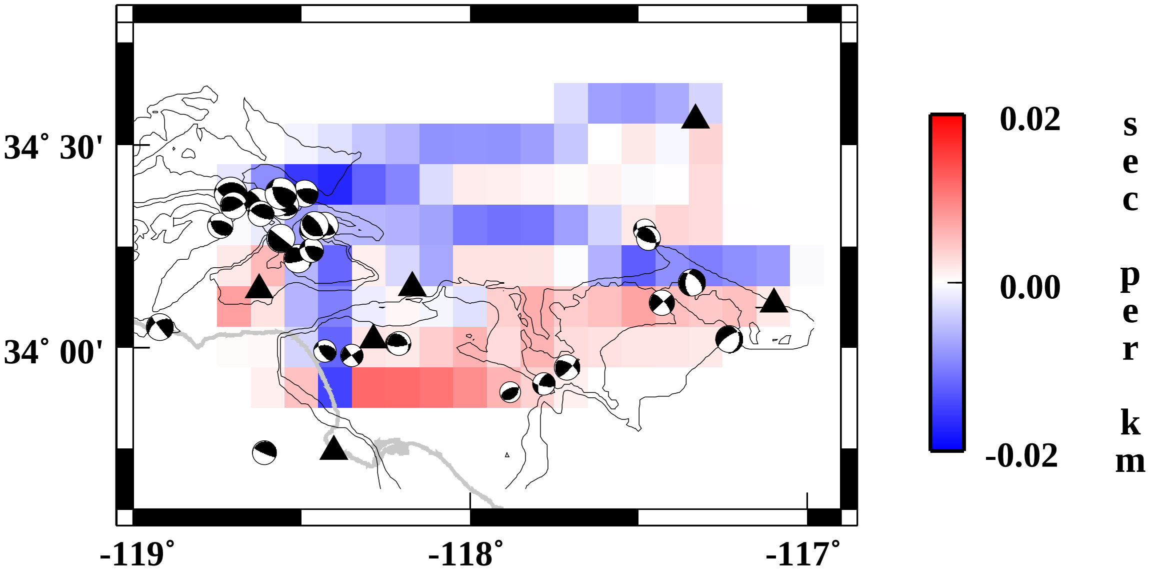

Figure 4.9: Summary results of comparison of the synthetic and observed seismograms. The map shows result of time shift tomography: the blue color corresponds to too fast parts of the model, and the red color corresponds to the slow parts of the model.

pattern is a consequence of a too fast and too simple background 1-D (laterally homogeneous) velocity model and that the western parts of the Los Angeles basin are also more complex than in the tested model. However, the central Los Angeles basin and San Bernardino basins seem to be too slow, which can be corrected with overall faster velocities in this part of the model.

4.5 Conclusions

We have shown that the reciprocal method provides a means for doing wave simulations that are otherwise expensive. In the example shown here, we are able to reduce the number of runs by a factor of two, and additional sources (when they become available) can be added with no extra computation.

We also developed a set of criteria for comparing data and synthetics computed in a complex 3-D media when exact matching of waveforms is not possible due to lack of model details or precision. The magnitude of displacement (MOD) measure has a number of advantages in this respect.

For the case study of the Southern California Velocity Model, Version 1, the characteristics of the fit between synthetic and recorded seismograms show consistent patterns, indicating regions which need to be improved to produce a better fit between data and synthetic seismograms. The bias would not be apparent unless large numbers of source receiver locations would be tested.

Chapter 5 Assessing site and path effects by full waveform modeling

5.1 Abstract

We have developed a methodology to calculate site and path effects for complex heterogeneous media using synthetic Green's functions. The Green's functions are calculated numerically by imposing body forces at the site of interest and then storing the reciprocal Green's functions along arbitrary finite fault surfaces. Using the reciprocal Green's functions, we can then simulate arbitrary source scenarios for those faults. Kinematic rupture effects and heterogeneous slip functions are accounted for by a Monte Carlo procedure, which is relatively inexpensive because the primary numerical calculations need be done only once. We have evaluated the site and path effects for three sites in the vicinity of the Los Angeles basin using the Southern California Velocity Model (version 2.2 [*Magistrale et al.*, 2000]). In this example we have simulated 75 realistic source scenarios for 5 major southern California faults and compared their responses at the selected sites. The largest amplitudes at the three sites are obtained from earthquakes on nearest faults rather than an earthquake on the San Andreas fault, which agrees with previous studies.

5.2 Introduction

A significant effort has been devoted to include synthetic simulations and observed data into the evaluation of the site and path effects in seismic hazard analyses (c.f. *Field and the SCEC Phase III Working Group* [2000]). Recently numerical simulations of long period strong ground motion in heterogeneous media were shown to be capable of reproducing the characteristic parameters of the observed data (*Olsen and Archuleta* [1996], *Wald and Graves* [1998], Chapter 4). Our goal is to include these long period strong ground motion simulations into the seismic hazard analyses as they have the potential to predict the strong ground motions more accurately than empirical relationships based on strong motion observations not directly related to a particular site.

The presently used method for the calculation of site and path effects by full waveform modeling has been developed by *Olsen and Archuleta* [1996]. They account for site and path effects by evolving the wavefield outward from the source location to a suite of sites, which means that one complete simulation is needed for each source location and scenario. However, it has been pointed out (*Field and the SCEC Phase III Working Group* [2000]) and we will show in this study, that site and path effects depend significantly on the particular choice of source location and scenario. Therefore, to estimate seismic hazard correctly we need to simulate a large number of source locations and realistic scenarios. The reciprocity method (Chapter 2) allows us to simulate a large number of source scenarios without recalculating the Green's functions evaluated for a given velocity model. This way the problem is divided into a component that is independent of the rupture scenario and one that depends on it. This method is restricted to assessing only one site effect per three numerical simulations of the wavefield. However, this apparent restriction is not significant considering the application of the method to long period structures which are located only at a few sites. We apply this method to three selected sites in the Los Angeles basin: a deep part of the basin, an edge of the basin, and a hard rock site near the basin. For each site we compare the effects of the 75 hypothetical rupture scenarios on the five major faults in the southern California, including the San Andreas fault.

5.3 Method, model and source parameterization

The full waveform modeling site and path effects are evaluated by imposing three orthogonal body forces at the site of interest and evaluating reciprocal Green's functions along fault surfaces. We may also store the evaluated reciprocal Green's functions on a very dense grid to simulate an arbitrary fault location. We need also the S-wave velocity and the rigidity modulus μ at the fault location to be able to properly evaluate the rupture velocity and to scale the displacement on a particular segment of the fault. We have numerically found, that we need to calculate the Green's functions at a minimum of three points per S-wave wavelength to model an arbitrary source rupture scenario (in agreement with *Spudich* [1981]). The wavelength in this case is that of the shortest S-wave traveling along the fault surface. To determine the rupture front history, we use the finite-difference travel-time method [*Vidale*, 1988] with velocities specified as a proportional fraction of the S-wave velocities along the fault surface as given in the model.

We used the values of rigidity modulus μ_n to scale the displacement on a fault segment to the seismic moment of that segment. A segment of area A_n and slip D_n has a seismic moment of

$$M_n = D_n A_n \mu_n.$$

This moment can be directly implemented for representation by a double-couple point-source in the finite-difference method (*Graves* [1996]). The total scalar sum of the long period moment M_w is then given by

$$M_w = \sum_{n=0}^{K} D_n A_n \mu_n, \tag{5.1}$$

where K is number of segments on the fault.

To relate the area S of the entire fault to the moment magnitude, we can use the empirical relationship derived from a global data set by *Wells and Coppersmith* [1994]:

$$M_w = 3.98 + 1.02\log(S). \tag{5.2}$$

Here S is the area of the entire fault in kilometers squared.

For a given M_w, we can evaluate the rupture area S from equation (5.2). We can then divide this area S into fault segments A_n each with slip D_n, with limit imposed by equation (5.1). For a uniform slip D_u and the fault area S divided into equal area segments A, we have

$$D_u = \frac{M_w}{AK\bar{\mu}} = \frac{M_w}{S\bar{\mu}},$$

where $\bar{\mu}$ is an arithmetic average of the rigidity modulus over the fault, and the *nth* segment of the fault has a moment of

$$M_n = \frac{M_w}{AK\bar{\mu}} A\mu_n = \frac{M_w}{K}\frac{\mu_n}{\bar{\mu}} = \frac{M_w \mu_n A}{S\bar{\mu}}. \tag{5.3}$$

The synthetic Green's functions were evaluated with the finite-difference method (*Graves* [1996]) for the Southern California Velocity Model Version 2.2 (*Magistrale et al.* [2000]). This model is the most recent model of the southern California velocity structure and includes the sedimentary basins, a laterally varying velocity structure outside of the basins, and a geotechnical layer of the slow velocities near surface. We assume for the purposes of this paper that the 3-D velocity model is correct. In general case, however, one may need to extend the simulations to include the uncertainty of the velocity model.

We have not included any attenuation effects in the calculations of the synthetic seismograms. An estimate of the attenuation effects for the chosen sites and sources is given in Appendix A. Appendix A shows the attenuation effects appear to be small for the sites and faults presented here and the period range of interest (T> 3 seconds), which agrees with our previous study from Chapter 4 where we compared the observed and synthetic seismograms.

This study directly includes the top of the velocity layers with the low velocities as given in the Southern California Velocity Model. We have used the equivalent medium parameters method of Chapter 3 to resample the top low velocity layers to avoid artifacts due to an arbitrary velocity clamping. This sampling ensures that the original Southern California Velocity Model is properly represented for the wave propagation of signal at long periods (greater than three seconds in this study). The sampling shown in Chapter 3 accounts for both the site effects and propagation effects. The minimum velocity in the resampled model used for the numerical simulations was 0.5 km/s for modeling of a signal with periods of 3 seconds and longer. Surface wave velocities are shown in Figure 5.1.

To illustrates the reciprocity method applied to site effect evaluation, we have selected 3 sites and 5 major faults in southern California. The sites were chosen to demonstrate the strong ground motion responses at different locations relative to the Los Angeles Basin. Table 5.1 has a list of the selected sites with their locations; they are also shown in Figure 5.1. Table 5.2 has a list of the basic parameters describing the faults. The fault parameters were taken from *Petersen et al.* [1996]. The position of the Newport-Inglewood fault is to the north-east relative to the commonly known surface fault trace; however, to be consistent with *Petersen et al.* [1996] we kept their location. Also note that *Petersen et al.* [1996] places the blind Elysian Park fault at a different location than *Olsen and Archuleta* [1996].

Selected sites

Site	Setting	Latitude (^{o}N)	Longitude (^{o}E)
SM	basin edge	34.011	-118.49
USC	deep basin	34.019	-118.286
PAS	hard rock	34.148	-118.171

Table 5.1: List of the selected sites and their locations.

The slip distributions (both the size and the rake) of the strike slip Hector Mine, California, earthquake (*Ji et al.* [2001]), the thrust fault Chichi, Taiwan, earthquake (*Mori and Ma* [2000]), the thrust fault Northridge, California, earthquake (*Wald et al.* [1996]) and the strike slip Landers, California, earthquake (*Wald and Heaton*

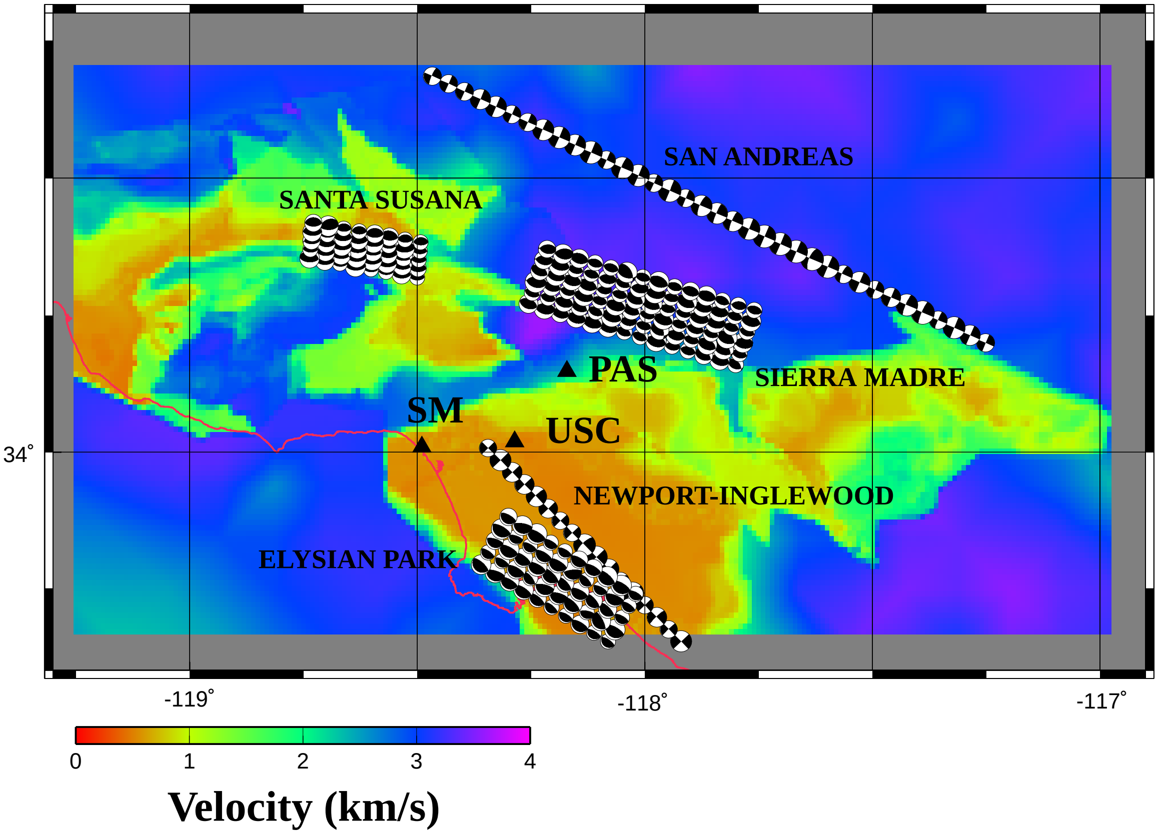

Figure 5.1: Southern California Velocity Model and locations of the selected sites and faults. The velocity is the Love wave group velocity at 3 second period. The fault locations are shown with beach balls as projected on the surface. The variations of the rake and magnitude of the beach ball represent the randomness of the fault slip vector. Selected sites are shown with black triangles and capital letters: PAS - Pasadena, USC - University of Southern California, and SM - Santa Monica. The large low velocity area between -118.5^o and -117.75^o longitude and below 34.1^o latitude is the Los Angles Basin.

[1994]) show that the slip size distribution and slip rake orientation on the fault plane is not uniform. Therefore, to simulate realistic rupture scenarios, we have used a randomized slip distribution in a Monte Carlo fashion. The slip's rake was also randomized within a maximum of 20 degrees from the average rake on the fault. The slip's size was randomized to a value at most 5 times larger than the uniform slip for a given fault (equation (5.3)). The randomized slip size was renormalized to keep the total scalar moment M_w the same. In the application shown here, we have used only one random slip distribution per fault as we have found there is little

Selected faults

Fault name	SE	NW	Dip	Rake	Strike
San Andreas	34.20,-117.25	34.70,-118.50	90	180	113.0
Newport-Inglewood	33.65,-117.92	34.03,-118.37	90	180	136
Santa Susana	34.32,-118.50	34.44,-118.76	55	90	91
Sierra Madre	34.16,-117.80	34.40,-118.24	45	90	107
Elysian Park	33.65,-118.08	33.92,-118.31	20	90	120

Fault name	Length	Depth 1	Depth 2	M_w	D
San Andreas	120.0	0.0	18.0	7.4	2.0
Newport-Inglewood	60.0	0.0	13.0	6.9	1.3
Santa Susana	25.0	0.0	13.0	6.6	1.1
Sierra Madre	47.0	0.0	15.0	7.0	1.2
Elysian Park	33.0	10.0	15.0	6.7	1.2

Table 5.2: List of the selected faults and their parameters. SE is a south-east horizontal location of the top part of the fault; NW is north-west location of the the top part of the fault; the two numbers represent northern latitude and eastern longitude. Length is length of the fault along the strike in kilometers. Depth 1 is the depth of the top of the fault in kilometers, and Depth 2 is the depth of the bottom of the fault in kilometers. D represent average slip on the fault surface in meters.

dependence of the measured characteristics (maximum velocity and duration) of the synthetic seismograms on particular instances of randomization, although we have found a significant difference between random and uniform slip.

The rupture velocity is an important parameter of the rupture scenario which can not be entirely predicted. Most of the previous studies used simplified rupture velocity scenarios leading to slow rupturing deeper parts of the fault (*Graves* [1998]) or super-shear velocities of the rupture in the shallow regions of the fault (*Olsen and Archuleta* [1996]). To avoid these extreme rupture velocities in a strongly heterogeneous medium, we have set the rupture speed relative to a constant fraction of the local shear wave speed (*Aagaard et al.* [2001]). To compute the rupture front time history, we use a simplified 2-D finite-difference travel-time algorithm ([*Vidale*, 1988]). To account for an unknown ratio of the rupture velocity to the S-wave velocity on the fault, we test several values of the rupture velocity: 60%, 75%, and 90% of the S-wave velocity on the fault. The effect of the strongly heterogeneous rupture velocity can be seen on the Newport-Inglewood fault's time history of the rupture front. Figure 5.2

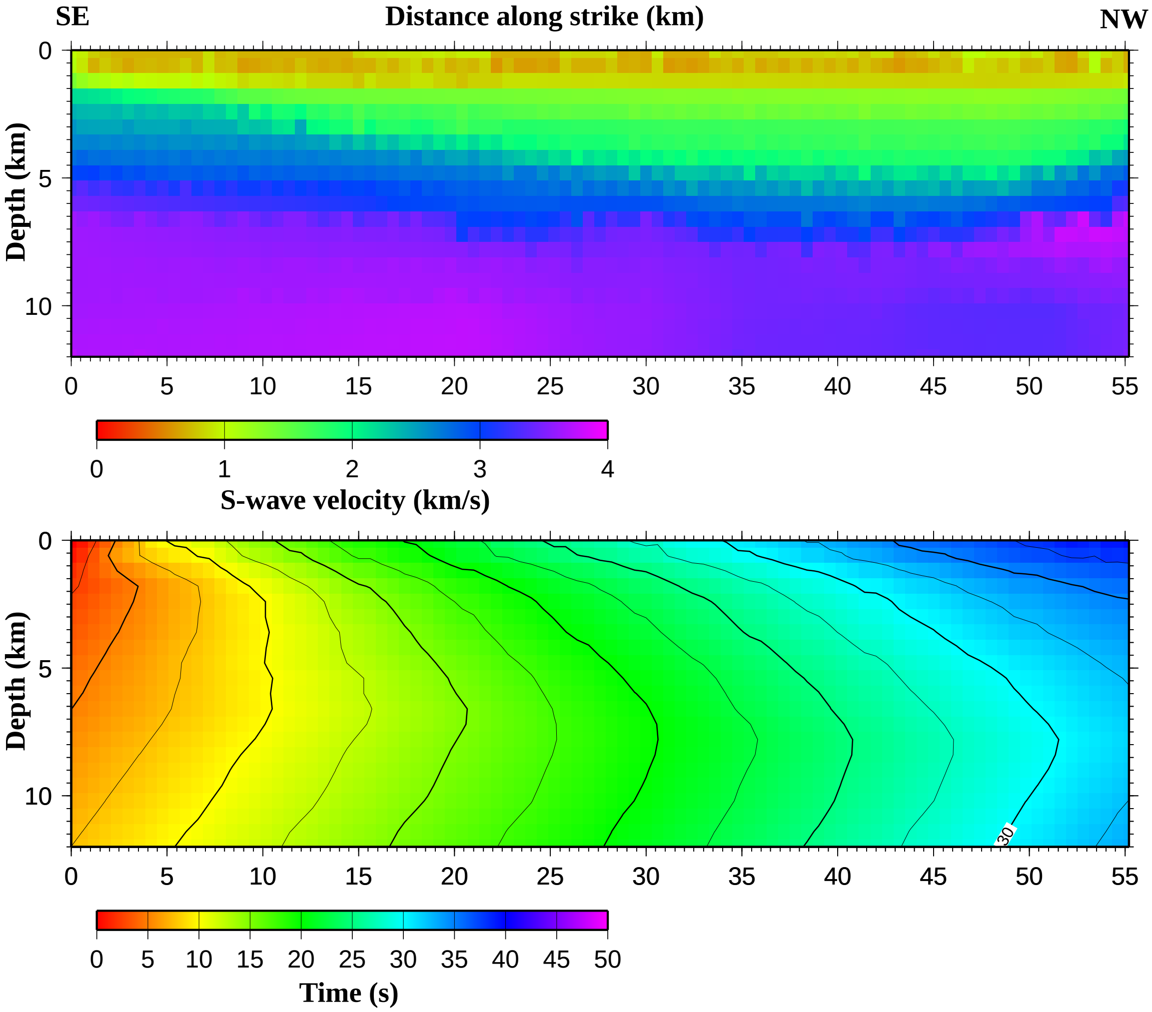

Figure 5.2: S-wave velocity on the Newport-Inglewood fault (top) and the time history of the rupture front for a hypocenter at the SE upper corner of the fault (bottom). The hypocenter is at 0.0 depth and 0.0 distance from the SE corner. The rupture speed is equal to 90% of the S-wave velocity on the fault.

shows the time history of the rupture front of the Newport-Inglewood fault's scenario with its hypocenter at the south-east top corner of the fault. Despite the fact that the rupture starts at the top, most of the fault ruptures upward from the center of the fault. Figure 5.3 shows time history of the rupture front of the San Andreas fault with a hypocenter at the south-east top corner of the fault. In this case, the fault time history of the rupture front shows a nearly horizontally propagating rupture through a weakly heterogeneous medium.

We have not varied the rise time (set to 3 seconds length) of the slip history on

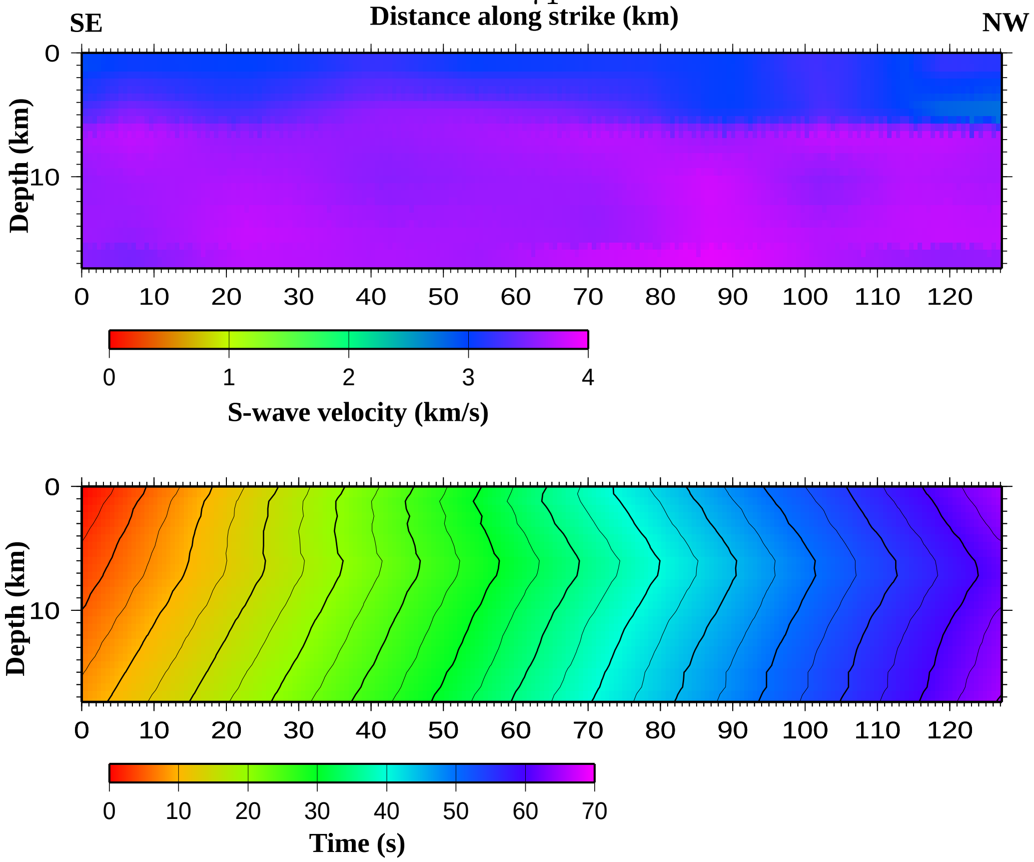

Figure 5.3: S-wave velocity on the San Andreas fault (top) and the time history of the rupture front for a hypocenter at the SE upper corner of the fault (bottom). The hypocenter is at 0.0 depth and 0.0 distance from the SE corner. The rupture speed is equal to 90% of the S-wave velocity on the fault.

the fault. An alternative rise time function can be accounted for by deconvolving the used rise time function from the seismograms and convolving with an alternative rise time function. Therefore, the rise time function does not influence the effects due to dynamic of the rupture or wave-propagation in a heterogeneous medium. Further, the variation of the rise time should not a significant factor for the studied period range of interest. For example, *Aagaard et al.* [2001] did not observe a significant effects on the strong motion seismograms due to realistic variation of the rise time. However, the rise time plays an important role for shorter period seismic wave propagation and its variability should be considered into site and path effect evaluation (it may vary by a factor of 2 for the magnitudes of earthquakes in this study).

5.4 Site and path effects at the selected sites

We have calculated strong motion seismograms due to 75 fault rupture scenarios at the three sites. For each site we note two characteristics of the synthetic seismograms: peak velocity and duration. The peak velocity is measured as the maximum amplitude of a vectorial sum of all 3 components over the entire seismogram. The duration is the time interval between the points at which 20% and 90% of the total energy has been recorded. This definition is analogous to the definition of *Trifunac and Brady* [1975], but we have shortened the interval to avoid biasing due to numerical dispersion.

Figure 5.4 shows the strong motion velocity seismograms with the largest recorded amplitude of all of the modeled seismograms. The largest amplitude was recorded at the closest site to a rupturing fault (USC site from the Newport-Inglewood fault). This scenario also has the fastest rupture velocity towards the site. The strong heterogeneity of the S-wave velocity on the fault makes the directivity effect less efficient as different parts of the fault propagate at different velocities and directions as can be seen in Figure 5.2. Figure 5.4 shows the earthquakes with rupture velocities closer to the S-wave velocity on the fault surface produce larger ground motion levels. The synthetic seismograms at the USC site are further complicated by the long duration of the coda following the initial peak as the energy released by the earthquake remains trapped in the Los Angeles basin. The energy arriving after the initial pulse is very similar in size among the different rupture velocities as the directivity does not affect the scattered energy.

Figure 5.5 shows the synthetic seismograms for the hypothetical earthquake on the San Andreas fault with three hypocenter locations, as would be recorded at the PAS site. The peak amplitude does not significantly vary between different hypocenters. The PAS site is approximately at 90^o azimuth to the strike of the fault and therefore the PAS site should not be very sensitive to the directivity of the rupture. The duration and the maximum amplitudes are comparable to the amplitudes simulated by *Graves* [1998] for the "PASA" station, and realistic magnitude $M_w = 7.5$ of the hypothetical San Andreas earthquake (our simulations were limited to $M_w = 7.4$ by

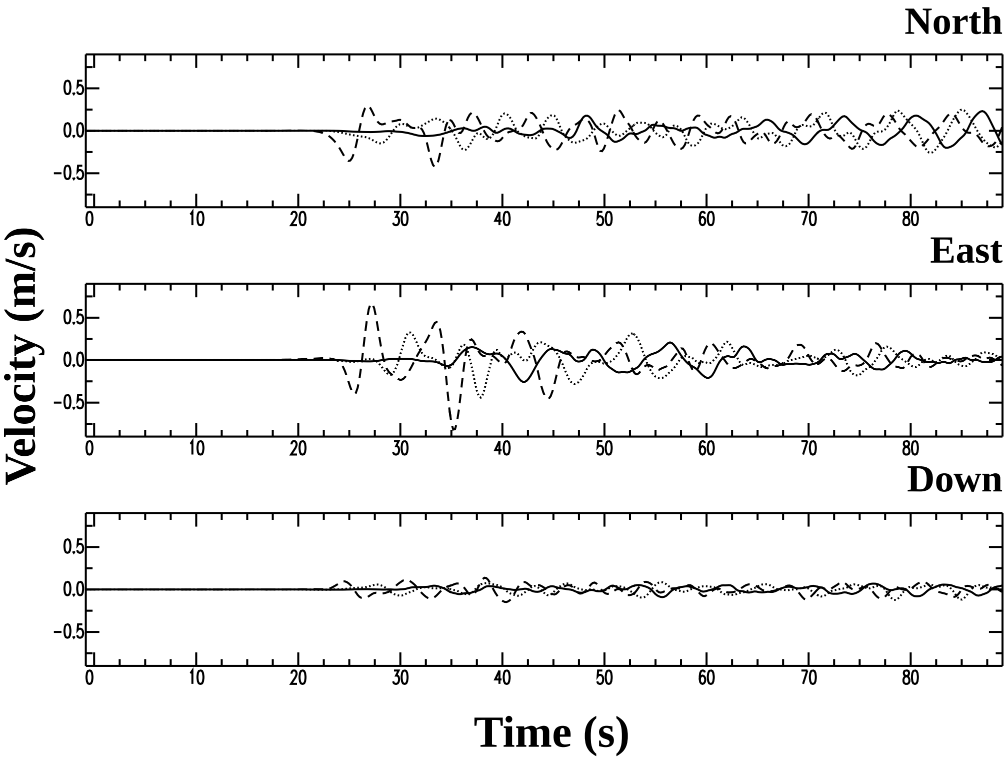

Figure 5.4: Synthetic seismograms at the USC site with the scenario causing the largest recorded amplitude in our simulations due to a rupture on the Newport-Inglewood fault with its hypocenter at the south-east corner at depth 0. The solid line represents seismograms due to an earthquake with rupture velocity equal to 60% of the S-wave velocity, the finest dashed line represents seismograms due to an earthquake with rupture velocity equal to 75% of S-wave velocity, and the coarsely dashed line represents seismograms due to an earthquake with rupture velocity equal to 90% of the S-wave velocity.

the size of the model). We have not observed a significant difference between the different rupture scenarios of the San Andreas earthquakes, even for the two sites inside the Los Angeles basin.

Figures 5.6, 5.7 and 5.8 summarize the maximum velocity amplitude comparison for the USC, SM and PAS sites. The Newport-Inglewood fault produces the largest ground motions of the ones modeled. Note that the maximum amplitude due an earthquake on the Newport-Inglewood fault varies by a factor of 4 the the USC and SM sites. Hypothetical earthquakes on the San Andreas and the Sierra Madre faults show similar maximum velocity amplitudes at the USC site, despite the difference

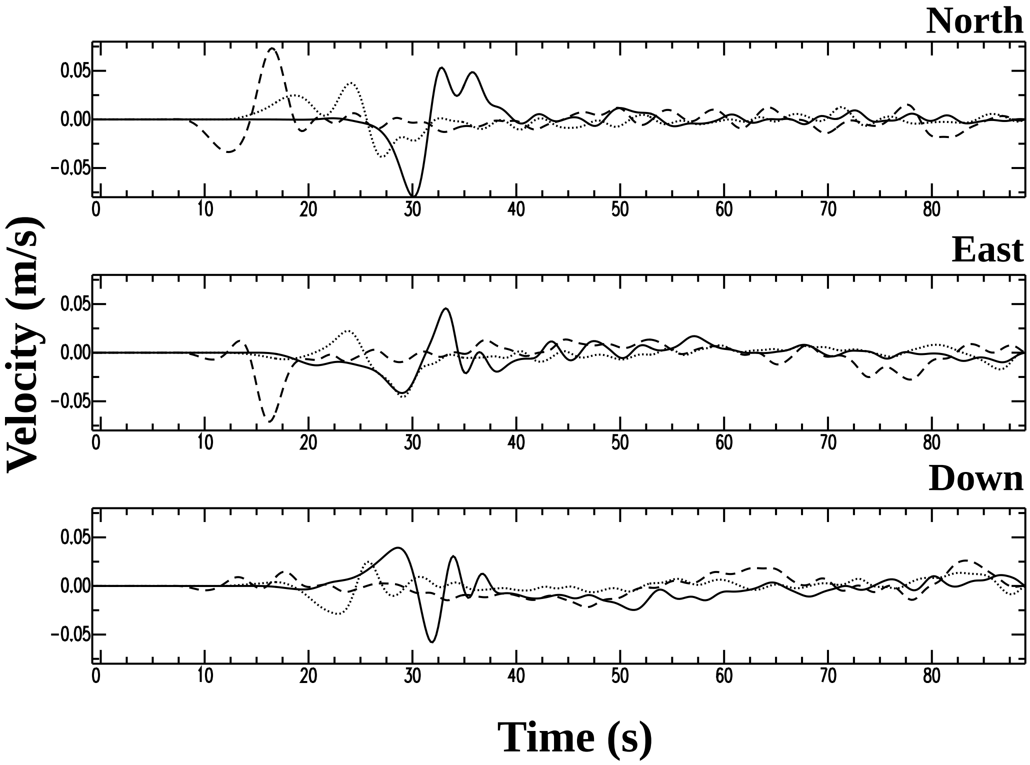

Figure 5.5: Synthetic seismograms at the PAS site for various fault rupturing scenarios of the San Andreas fault. All nine seismograms correspond to the earthquakes with rupture velocity equal to 90% of the S-wave velocity. The solid line represents rupture scenario with a hypocenter at the south-east corner of the fault at depth of 0.0 km. The finest dashed line rupture scenario with a hypocenter at the north-west corner of the fault at depth of 0.0 km. The coarsely dashed line is for the case with a hypocenter at the center of the fault.

in distance of the faults from the site. At the USC site, the Elysian Park fault causes a large maximum amplitude for a scenario in which the fault ruptures from the south-east top corner of the fault. This observation emphasizes the importance of testing different rupture scenarios to evaluate realistic seismic hazard from a particular fault, because with the hypocenter in the other parts of the fault the maximum amplitudes are 2-4 times smaller. Our maximum amplitude values are significantly smaller than those simulated by *Olsen and Archuleta* [1996] for the same reasons (uniform vs. random slip distribution, super-shear rupture velocity vs. sub-shear rupture velocity, seismic moment to rupture area scaling) that maximum amplitude values differ between *Olsen et al.* [1995] and *Graves* [1998]. The maximum amplitudes simulated for the Santa Susana fault at the USC and SM sites are similar to those observed for the Northridge Earthquake (*Olsen and Archuleta* [1996]). For the SM site the Newport-Inglewood fault is again the most hazardous fault. The large spread in the simulated maximum velocity amplitudes at the SM site due to earthquakes on the Newport-Inglewood fault again emphasizes the importance of testing different rupture scenarios. There are three Sierra Madre fault earthquake scenarios with hypocenters at the center and both east corners of the fault, which generate large velocity amplitudes at the SM site. This is probably caused by the efficient coupling of the earthquakes' directivity and the Los Angeles basin. A similar effect at the SM site can be observed for hypothetical earthquakes from the San Andreas fault for scenarios with its hypocenter at the south-east end of the fault. The PAS site is located almost outside of the Los Angeles basin; therefore, the maximum velocity amplitudes at the site are generally much smaller than the maximum velocity amplitudes simulated for the SM and USC sites. The only large maximum velocity amplitudes are observed for the hypothetical earthquakes on the Sierra Madre and the San Andreas faults. The large amplitudes at the PAS site Note that the maximum amplitude due an earthquake on the Sierra Madre fault varies by a factor of 3 for the PAS site. The large maximum velocity amplitudes due to the earthquakes on the Sierra Madre fault are caused by the proximity of the fault to the site. The large amplitudes due to the earthquakes on the San Andreas fault are caused by the large seismic moment of the fault.

Figure 5.9 summarizes the source and site durations of the different rupture scenarios on the selected faults. The source durations increase with increasing size of the fault as the rupture velocity is limited by the shear wave velocity. The definition of the source durations was slightly modified from the site durations. It is the time between 0% and 100% of the released energy, because we wanted to represent the entire source duration. The San Andreas fault ruptures for the longest time, however the USC and SM sites' durations due to earthquakes on the San Andreas fault are probably limited by the length of the computed seismograms (the first arrivals at

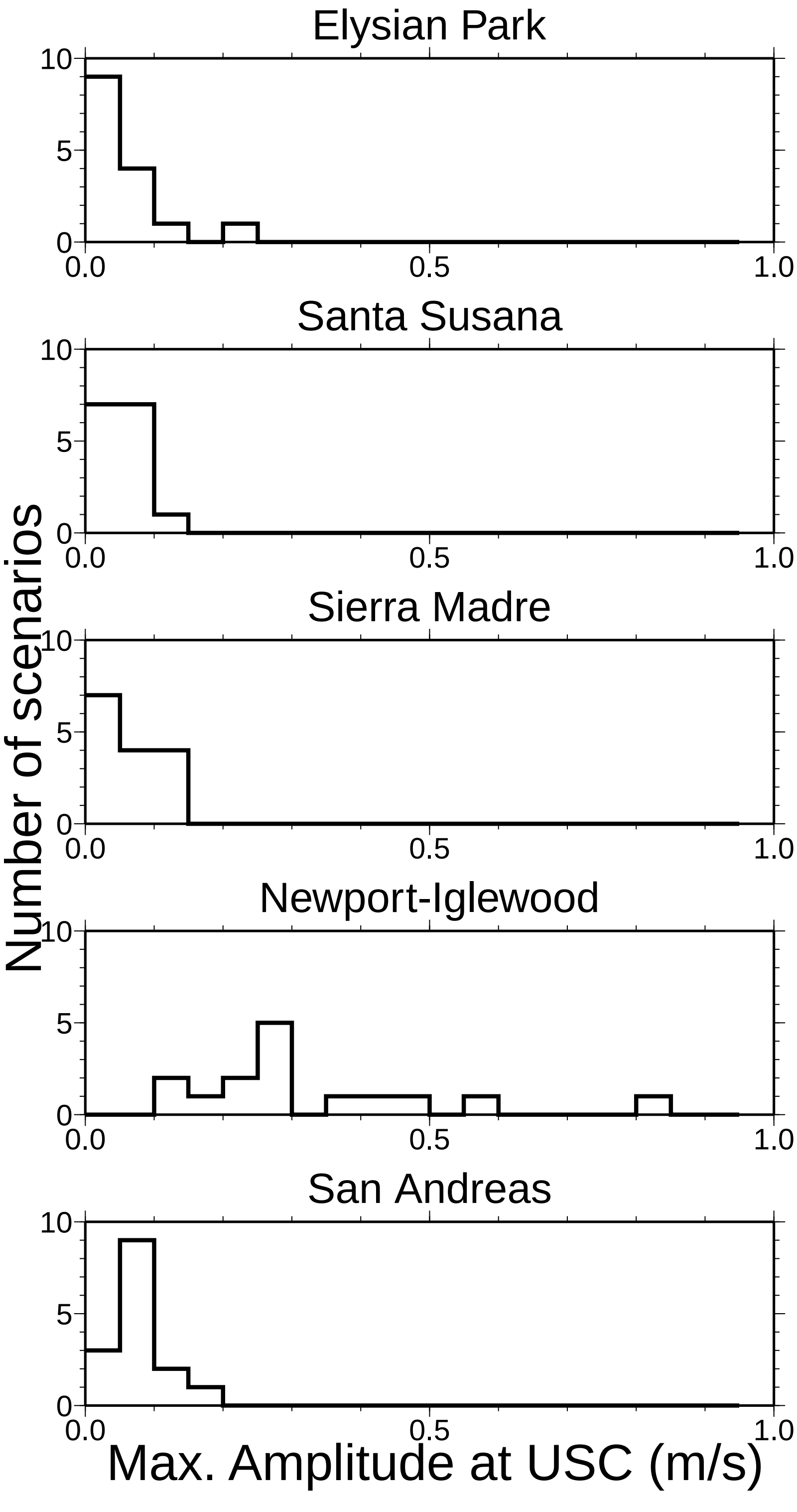

Figure 5.6: Maximum amplitude of the velocity vector as recorded at the USC site from 15 different rupture scenarios: 3 different rupture velocities and 5 different hypocenters, for each fault.

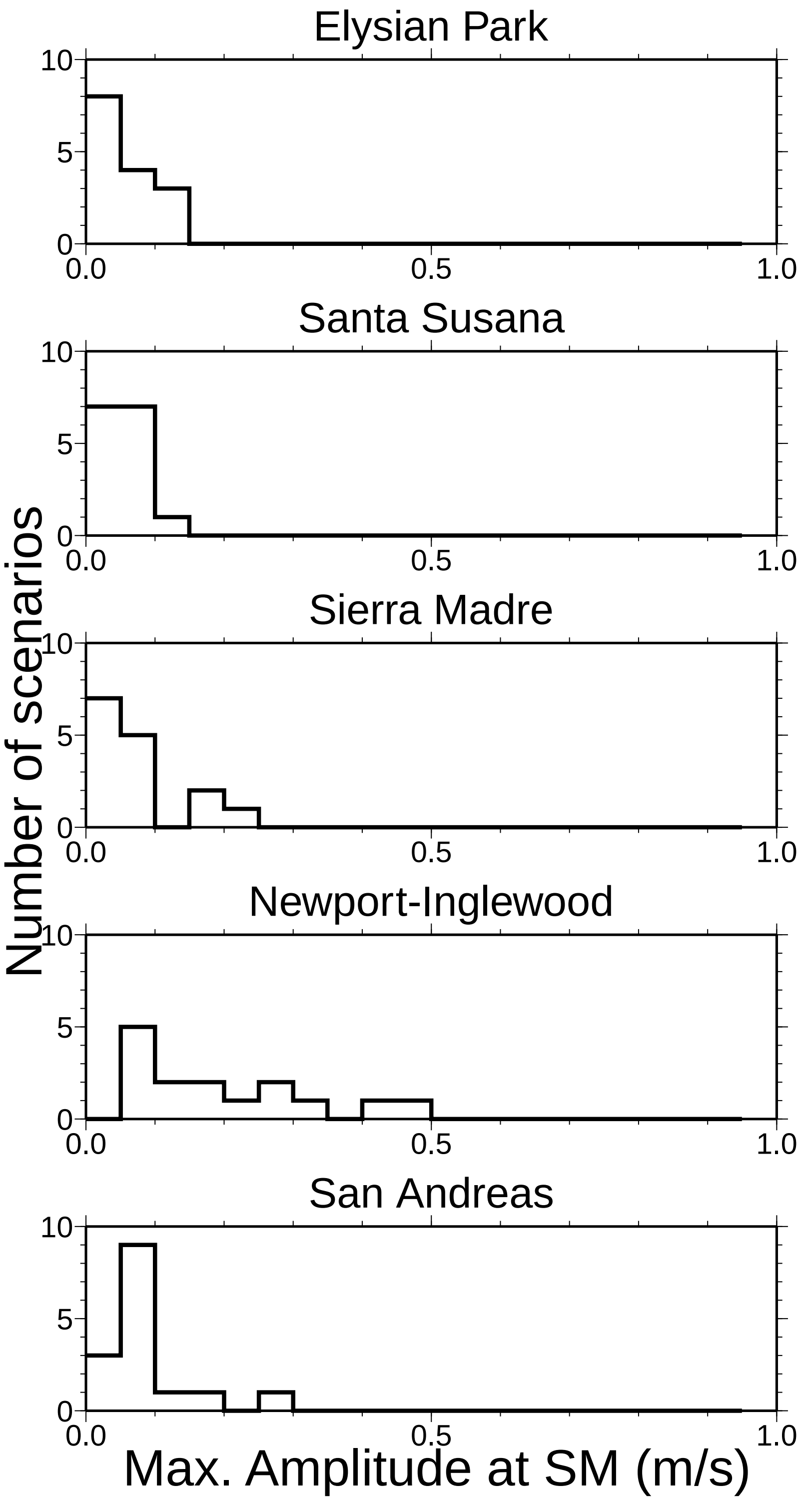

Figure 5.7: Maximum amplitude of the velocity vector as recorded at the SM site from 15 different rupture scenarios: 3 different rupture velocities and 5 different hypocenters, for each fault.

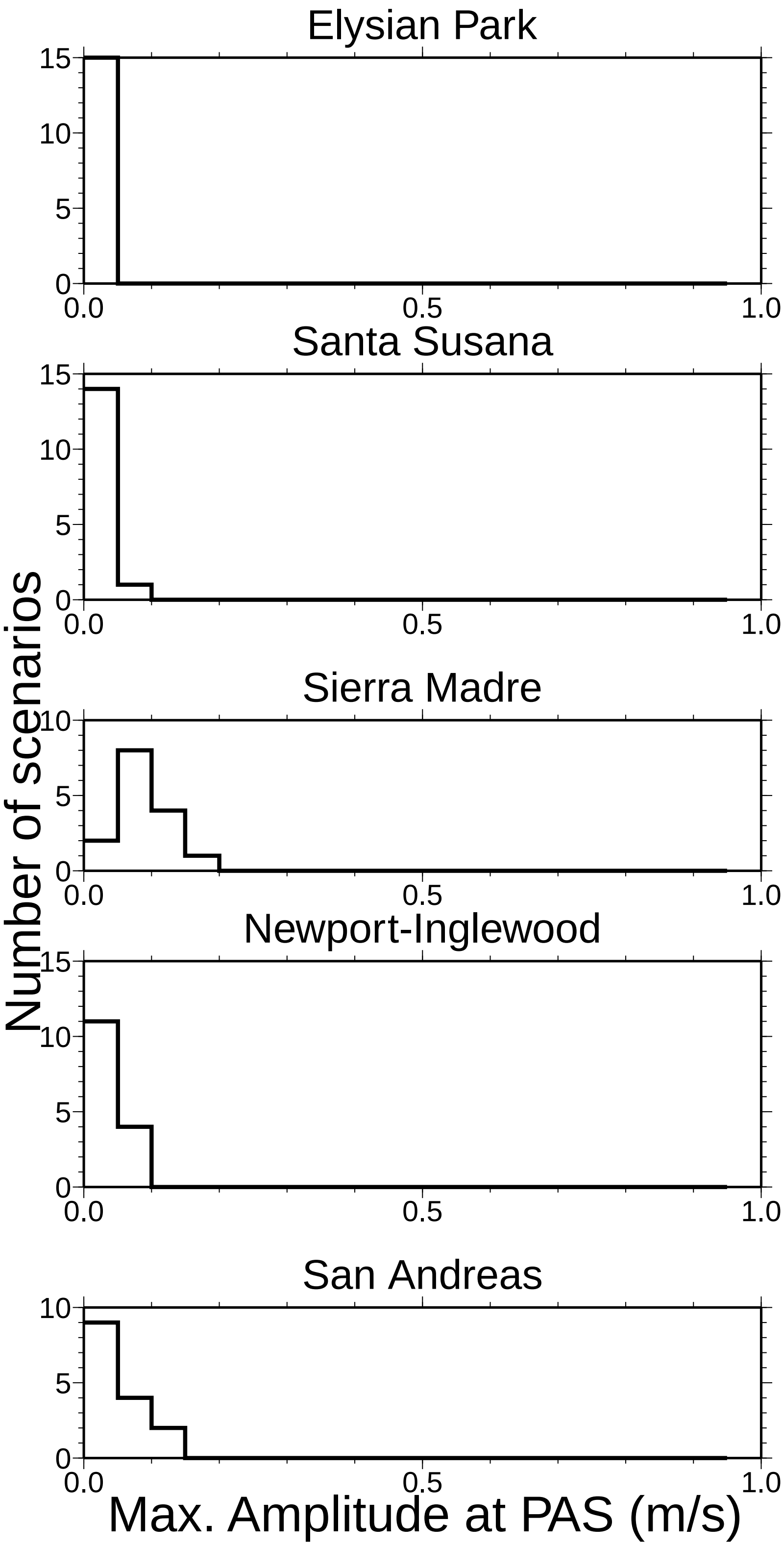

Figure 5.8: Maximum amplitude of the velocity vector as recorded at the PAS site from 15 different rupture scenarios: 3 different rupture velocities and 5 different hypocenters, for each fault.

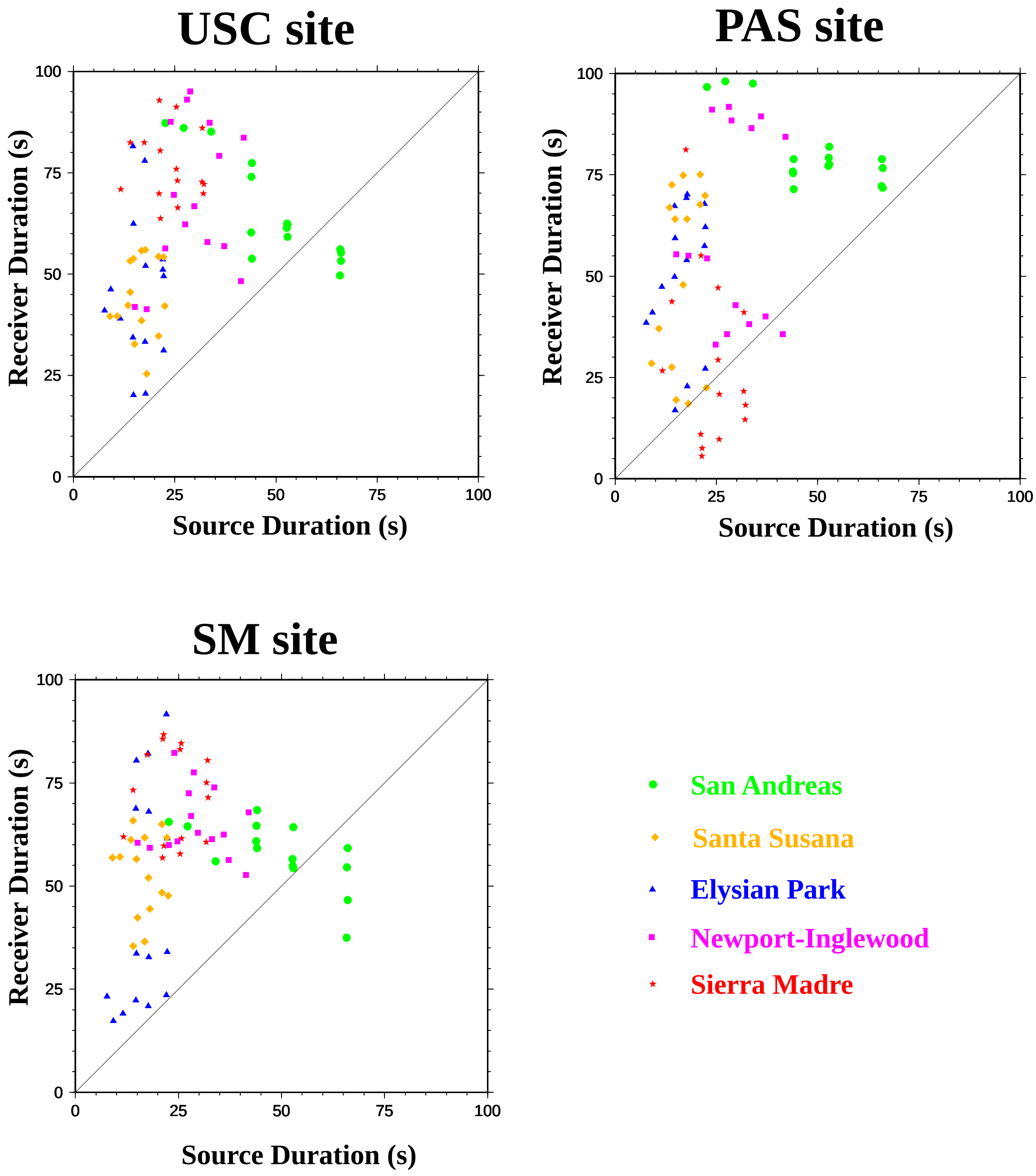

Figure 5.9: The source and site durations for the selected site and 75 rupture scenarios. The source durations are measured from the initiation to the end of the rupture process, the site durations are measure as a time interval between 20 to 70% of energy in the seismogram.

USC and SM sites appear between 30-40 seconds after the rupture initiation).

The site durations are longer than the source durations for most of the rupture scenarios as the scattered energy in the heterogeneous velocity model tend to arrive later. Except for the earthquakes on the San Andreas fault, the USC and SM sites have generally longer site durations than the PAS site as the surface waves trapped inside the sedimentary basin extend durations at the USC and SM sites. Most of the site durations at the USC site are two to three times as long as the source durations for the Newport-Inglewood, Sierra Madre, and Santa Susana faults. The USC site's durations due to the earthquakes on the Newport-Inglewood fault show a significant dependence on the rupture scenarios; the scenarios in which the fault ruptures southward with a high velocity (90% of the S-wave velocity) have short durations. Most of the durations at the SM site are two to three times as long as the source durations for the Newport-Inglewood, Sierra Madre, and Santa Susana faults. The SM site's durations due to the Elysian Park fault earthquakes show a strong dependency on the rupture scenarios; the ruptures with hypocenters at the south end of the fault show longer durations. The PAS site's durations due to earthquakes on the Newport-Inglewood, Elysian Park, and Santa Susana faults are strongly dependent on the rupture scenario, as only certain configurations tend to trap energy in the Los Angeles basin. The PAS site's durations due to the Sierra Madre fault earthquakes are relatively short as the PAS site is close to the fault in a weakly heterogeneous medium. However, strong heterogeneity significantly extends the duration of the signal as is shown by the PAS site's durations due to earthquakes on the Newport-Inglewood fault.

5.5 Conclusions

The developed method for evaluation of the site and path effects with full waveform synthetic seismograms allows to simulate earthquakes in a complex heterogeneous media and with the variable rupture scenario. Using the Southern California Velocity Model we have evaluated the theoretical site effects for three locations in the Los Angeles area, and have shown the variations due to rupture scenario on a fault causes factor of 3 variation in the maximum amplitude for sites outside of the sedimentary basin, and possible factor of 4 in the maximum amplitude for sites inside the sedimentary basins. We have found that the largest amplitudes are observed from earthquakes on nearest faults rather than an earthquake on the San Andreas fault.

Appendix A Attenuation estimate

Attenuation is not part of the Southern California Velocity Model; therefore, we shall only estimate the attenuation effect on the maximum amplitude by a simple order of magnitude calculation. *Aki and Richards* [1980] (page 168-9) derive the attenuation effect in a homogeneous medium with an attenuation factor $Q(T) \gg 1.0$ for a wave with amplitude A_0 at point $x = 0$ and propagating with velocity c; the amplitude of this wave at distance x is

$$A(x) = A_0 e^{\frac{\pi x}{cTQ(T)}}, \tag{A.1}$$

Using the engineering practice (c.f. *Kramer* [1996], Chapter 4) we use the shortest distance from the finite fault from our site to estimate the distance x in equation (A.1). Obviously, equation (A.1) implies the longer the period of the propagating wave, the smaller the attenuation effects. Therefore, we shall make our estimate only for the shortest period of 3 seconds. Equation (A.1) also implies that the faster propagating waves have smaller attenuation effects (at the same period and distance); therefore, to estimate an upper bound on the attenuation effects we shall investigate surface waves, the slowest propagating waves at a given period.

It is difficult to estimate a representative crustal value of the attenuation at 3 seconds period $Q(3.0)$. The seismic waves are mainly attenuated at the very top of the crust (90% of the signal is attenuated at the top 3 km of the crust, *Abercrombie* [1997]). However, there are very few measurements of attenuation at long periods for the strong motion data. *Su et al.* [1988] use regional 1-D model of Southern California with values of $Q_S \sim 20 - 150$ (frequency independent attenuation of the S-waves), which is consistent with value of $Q = 70$ found by *Hough* [1997] for frequencies 1-10 Hz at Ridgecrest, California, and $Q = 80 - 130$ from *Ma and Kanamori* [1994] for frequency approximately 1 Hz and Pasadena-Sierra Madre earthquake, California.

The representative values for sedimentary basins are in the lower range of the above values as can be seen in the *Ibanez et al.* [1991] study of attenuation in sedimentary basins. Therefore, we estimate the representative values for $Q(3.0) \sim 100$ for paths outside of sedimentary basins and $Q(3.0) \sim 50$ for paths inside sedimentary basins.

Assuming we can approximate the medium between the San Andreas fault and the PAS site by a homogeneous halfspace with $c = 3.0$ km/s (see Figure 5.1) and a distance of $x \sim 50.0$ km, equation (A.1) gives

$$\frac{A(50.0)}{A_0} < e^{\frac{-17}{Q(3.0)}}.$$

This path is outside of the sedimentary basin and therefore the maximum amplitude is at most (we estimate the upper bound) reduced by 15% making the attenuation effect negligible. However, for a wave propagation inside the sedimentary basin we must be more careful. We can approximate the medium between the Newport-Inglewood fault and the PAS site as a homogeneous halfspace with $c = 0.7$ km/s (see Figure 5.1) and a distance of $x \sim 30.0$ km. Equation (A.1) gives

$$\frac{A(30.0)}{A_0} < e^{\frac{-45}{Q(3.0)}}.$$

This path is inside the Los Angeles sedimentary basin and therefore the maximum amplitude is at most reduced by 60% making the attenuation possibly more significant. However, this is an upper bound and therefore we know the maximum amplitudes without attenuation are a factor of 2 from the maximum amplitudes computed for models with a realistic attenuation. The effects of attenuation at the USC or SM sites are even smaller as the distances between faults and the sites are smaller. However, multiply scattered waves inside the basins may be more severely attenuated even at periods of 3 seconds. Therefore, our durations may be slightly overestimated and should be considered as an upper bound.

Bibliography

Aagaard, B., J. Hall, T. Heaton, and M. Eeri, Characterization of near-source ground motions with earthquake simulations, *submitted to Journal of Geophysical Research*, 2001.

Abercrombie, R., Near-surface attenuation and site effects from comparison of surface and deep borehole recordings, *Bulletin of the Seismological Society of America*, *87*, 731–744, 1997.

Aki, K., and P. Richards, *Quantitative Seismology*, W.H. Freeman and Co, 1980.

Backus, G. E., Long-wave elastic anisotropy produced by horizontal layering, *Journal of Geophysical Research*, *67*, 4427–4440, 1962.

Betti, E., Theria dell'elasticita, *Il Nuovo Cimento (Ser. II)*, *7-10*, 5–21; 69–97; 158–180; 357–367; 34–43 (Vol. 9); 58–108 (Vol. 10), 1871-73.

Bouchon, M., Teleseismic body wave radiation from a seismic source in a layered medium, *Geophysical Journal Research*, *47*, 515–530, 1976.

Burridge, R., and L. Knopoff, Body force equivalents for seismic dislocations, *Bulletin of the Seismological Society of America*, *54*, 1875–1888, 1964.

Červený, V., *Seismic ray theory*, in press, Cambridge University Press, 2001.

Chapman, C., Reflection/transmission coefficient reciprocities in anisotropic media, *Geophysical Journal International*, *116*, 498–501, 1994.

Chapman, C., and R. Coates, *Seismic Waveform Modelling of High-Frequency Body Waves*, Plenum Publishing Co., 1991.

Claerbout, J., *Fundamentals of Geophysical Data Processing*, McGraw-Hill, Inc., 1976.

Clayton, R. W., and B. Engquist, Absorbing boundary conditions for acoustic and elastic wave equations, *Bulletin of the Seismological Society of America*, *67*, 1529–1540, 1977.

Dahlen, F., and J. Tromp, *Theoretical Global Seismology*, Princeton University Press, 1998.

de Hoop, M., and A. de Hoop, Wave-field reciprocity and optimalization in remote sensing, *Proc. R. Soc. Lond. A*, *456*, 641–682, 2000.

Dellinger, J., A crossed-dipole reciprocity "paradox", *Leading Edge*, *16*, 1465–1471, 1997.

Eisner, L., and R. W. Clayton, A reciprocity method for multiple source simulations, *Bulletin of the Seismological Society of America*, *91*, 553–560, 2001.

Eisner, L., and R. W. Clayton, Equivalent medium parameters for numerical modelling in media with near-surface low-velocities, *accepted to Bulletin of the Seismological Society of America*, 2001b.

Eisner, L., and R. W. Clayton, Assessing site and path effects by full waveform modeling, *reviewed in Journal of Geophysical Research*, 2002.

Field, E., and the SCEC Phase III Working Group, Accounting for site effects in probabilistic seismic hazard analyses of Southern California: Overview of the SCEC Phase III report, *Bulletin of the Seismological Society of America*, *90*, S1–S31, 2000.

Graves, R., Simulating seismic wave propagation in 3D elastic media using staggered-grid finite differences, *Bulletin of the Seismological Society of America*, *86*, 1091–1106, 1996.

Graves, R., Effects of small scale near surface geologic heterogeneity on strong ground motions at long periods (T>1 sec), *Seismological Research Letters*, *68*, 302, 1997.

Graves, R., Three-Dimensional finite-difference modeling of the San Andreas fault: Source parameterization and ground-motion levels, *Bulletin of the Seismological Society of America*, *88*, 881–897, 1998.

Graves, R., and D. Wald, Resolution analysis of finite fault source inversion using 1D and 3D Green's functions, part I: Strong motions, *accepted to Journal of Geophysical Research*, 2001.

Graves, R. W., Preliminary analysis of long-period basin response in the Los Angleles region from the 1994 Northridge earthquake, *Geophysical Research letters*, *22*, 101–104, 1995.

Graves, R. W., and R. Clayton, Modeling path effects in 3-dimensional basin structures, *Bulletin of the Seismological Society of America*, *82*, 81–103, 1992.

Hadley, D., and H. Kanamori, Seismic structure of the Transverse Ranges, California, *Bulletin of the Geological Society of America*, *88*, 1469–1478, 1977.

Haskell, N., The dispersion of surface waves on multilayered media, *Bulletin of the Seismological Society of America*, *43*, 17–34, 1953.

Hauksson, E., Crustal structure and seismicity distribution adjacent to the Pacific and North America plate boundary in southern California, *Journal of Geophysical Research*, *105*, 13,875–13,903, 2000.

Hooke, R. S., *Lectures de potentia restitutiva (Of spring,explaining the power of springing bodies)*, 1678.

Hough, S., Empirical green's function analysis: Taking the next step, *Journal of Geophysical Research-Solid Earth*, *102*, 5369–5384, 1997.

Ibanez, J., J. Morales, F. DeMiguel, F. Vidal, G. Alguacil, and A. Posadas, Effect of a sedimentary basin on estimations of q_c and q_{Lg}, *Physics of the Earth and Planetary Interiors*, *66*, 244–252, 1991.

Ji, C., D. Wald, and D. Helmberger, Source description of the 1999 Hector Mine, California, earthquake; Part II: Complexity of slip history, *submitted to Bulletin of the Seismological Society of America*, 2001.

Komatitsch, D., and J. Tromp, Introduction to the spectral-element method for three-dimensional seismic wave propagation, *Geophysical Journal International*, *139*, 806–822, 1999.

Kramer, S., *Geotechnical Earthquake Engineering*, Prentice-Hall, Inc., 1996.

Lamb, H. F., On the propagation of tremors over the surface of an elastic solid, *Philosophical Transactions of the Royal Society of London*, *203*, 1–42, 1904.

Levshin, A., T. Yanovskaya, A. Lander, B. Bukchin, M. Barmin, L. Ratnikova, and E. Its, *Seismic surface waves in a laterally inhomogeneous earth*, vol. 1, Kluwer Academic Publishers., 1989.

Love, A., *A Treatise on the Mathematical Theory of Elasticity*, New York, Dover Publications., 1892.

Ma, K.-F., and H. Kanamori, Broadband waveform observation of the 28 June 1991 Sierra-Madre earthquake sequence (M(l)=5.8), *Bulletin of the Seismological Society of America*, *84*, 1725–1738, 1994.

Magistrale, H., K. McLaughlin, and S. Day, A geology-based 3D velocity model of the Los Angeles basin sediments, *Bulletin of the Seismological Society of America*, *86*, 1161–1166, http://www.scecdc.scec.org/3Dvelocity/3Dvelocity.html, 1996.

Magistrale, H., S. Day, R. Clayton, and R. Graves, The SCEC Southern California Reference 3D Seismic Velocity Model Version 2, *Bulletin of the Seismological Society of America*, *90*, S65–76, 2000.

Montalbetti, J. F., and E. K. Kanasewich, Enhancement of teleseismic body waves with a polarization filter, *Geophysical J. R. ast. Soc.*, *21*, 119–129, 1970.

Mori, J., and K. Ma, Review of seismological results from the 1999 Chichi, Taiwan, earthquake, *EOS*, *81*, F873, 2000.

Muir, F., J. Dellinger, J. Etgen, and D. Nichols, Modeling elastic fields across irregular boundaries, *Geophysics*, *57*, 1189–1193, 1992.

Navier, C., *Momoire sur les lois de lÉquilibre et due mouvement des corps solides elastiques*, vol. 7, Academie royale des sciences, 1827.

Olsen, K., and R. Archuleta, Three-dimensional simulation of earthquakes on the Los Angeles fault system, *Bulletin of the Seismological Society of America*, *86*, 575–596, 1996.

Olsen, K., R. Archuleta, and J. Matarese, Magnitude 7.75 earthquake on the San Andreas fault: Three-dimensional ground motion in Los Angeles, *Science*, *270*, 1628–1632, 1995.

Olsen, K., R. Madariaga, and R. Archuleta, Three-dimensional dynamic simulation of the 1992 Landers earthquake, *Science*, *278*, 834–838, 1997.

Opršal, I., and J. Zahradník, Elastic finite-difference method for irregular grids, *Geophysics*, *64*, 240–250, 1999.

Petersen, M., W. Bryant, C. Cramer, T. Cao, M. Riechle, A. Frankel, J. Lienkaemper, P. McCrory, and D. Schwartz, Probabilistic seismic hazard assessment for the state of California, *Tech. rep.*, Division of Mines and Geology, open-file report 96-08; United States Geological Survey; open-file report 96-706, 1996.

Rayleigh, L. H. J. S., Some general theorems relating to vibrations, *Proceedings of the London Mathematical Society*, *4*, 357–368, 1873.

Rayleigh, L. H. J. S., On waves propagated along the plane surface of an elastic solid, *Proceedings of the London Mathematical Society*, *17*, 4–11, 1885.

Saikia, C., D. Dreger, and D. Helmberger, Modeling of energy amplification recorded within greater Los-Angeles using irregular structure, *Bulletin of the Seismological Society of America*, *84*, 47–61, 1994.

Schoenberg, M., and F. Muir, A calculus for finely layered anisotropic media, *Geophysics*, *54*, 581–589, 1989.

Spudich, P., Frequency domain calculation of extended source seismograms, *EOS*, *62*, 960, 1981.

Su, F., J. Anderson, and Y. Zeng, Study of weak and strong ground motion including nonlinearity from the Northridge, California, earthquake sequence, *Bulletin of the Seismological Society of America*, *88*, 1411–1425, 1988.

Thompson, W., Transmission of elastic waves through a stratified solid medium, *Journal of Applied Physics*, *21*, 89–93, 1950.

Trifunac, M., and A. G. Brady, A study of the duration of strong ground earthquake ground motion, *Bulletin of the Seismological Society of America*, *65*, 581–626, 1975.

Vidale, J., Finite-difference calculation of travel-times, *Bulletin of the Seismological Society of America*, *78*, 2062–2076, 1988.

Virieux, J., SH wave propagation in heterogeneous media: velocity-stress finite-difference method, *Geophysics*, *49*, 1933–1957, 1984.

Wald, D., and R. Graves, The seismic response of the Los Angeles basin, California, *Bulletin of the Seismological Society of America*, *88*, 337–356, 1998.

Wald, D., and T. Heaton, Spatial and temporal distribution of slip for the 1992 Landers, California, earthquake, *Bulletin of the Seismological Society of America*, *84*, 668–691, 1994.

Wald, D., T. Heaton, and K. Hudnut, The slip history of the 1994 Northridge, California, earthquake determined from strong-motion, teleseismic, gps, and leveling data, *Bulletin of the Seismological Society of America*, *86*, S49–S70, 1996.

Wells, D., and K. Coppersmith, New empirical relationships among magnitude, rupture length, rupture width, rupture area, and surface displacement, *Bulletin of the Seismological Society of America*, *84*, 974–1002, 1994.

Wu, R., and K. Aki, Introduction: Seismic wave scattering in three-dimensionally heterogeneous Earth, *Pure and Applied Geophysics*, *128*, 1–6, 1988.

Zahradník, J., P. Moczo, and F. Hron, Testing four elastic finite-difference schemes for behavior at discontinuities, *Bulletin of the Seismological Society of America*, *83*, 107–129, 1993.

Zeng, Y., F. Su, and K. Aki, Scattering wave energy propagation in a random isotropic scattering medium 1. Theory, *Journal of Geophysical Research*, *96*, 607–619, 1991.

Zhu, L., and D. Helmberger, Advancement in source estimation techniques using broadband regional seismograms, *Bulletin of the Seismological Society of America*, *86*, 1634–1641, 1996.